

Capacitive Sensing with a Fluorescent Lamp

by

John Jacob Cooley

Submitted to the Department of Electrical Engineering and Computer
Science

in partial fulfillment of the requirements for the degree of

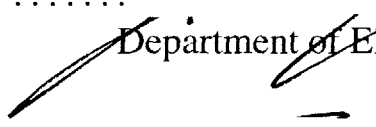
Master of Engineering in Electrical Science and Engineering

at the

MASSACHUSETTS INSTITUTE OF TECHNOLOGY

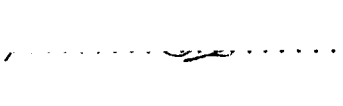
February 2007

© Massachusetts Institute of Technology 2007. All rights reserved.

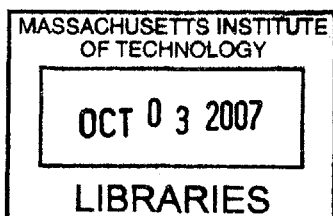
Author
 Department of Electrical Engineering and Computer Science

February 2007

Certified by
 Steven B. Leeb
Professor
Thesis Supervisor

Certified by
 Al-Thaddeus Avestruz
Student
Thesis Co-signer

Accepted by
 Arthur C. Smith
Chairman, Department Committee on Graduate Students



Capacitive Sensing with a Fluorescent Lamp

by

John Jacob Cooley

Submitted to the Department of Electrical Engineering and Computer Science
on February 2007, in partial fulfillment of the
requirements for the degree of
Master of Engineering in Electrical Science and Engineering

Abstract

This work presents a modified fluorescent lamp that can be used as a capacitive sensing system. The lamp sensor measures changes in the electric fields emitted from the fluorescent bulbs in order to deduce the presence and motion of conductive and dielectric objects below the lamp. The prototype lamp sensor demonstrated a detection range of 10 feet for the presence and motion of a human below the lamp. Potential applications of the lamp sensor include proximity detection, motion sensing, security monitoring, activity level monitoring for power management and control and metal or dangerous substance detection.

Thesis Supervisor: Steven B. Leeb

Title: Professor

Thesis Co-supervisor: Al-Thaddeus Avestruz

Title: Graduate Research Assistant

Acknowledgments

We would like to acknowledge the generous support for this research by the United States Department of Justice, the Grainger Foundation, and the Center for Materials Science and Engineering at MIT.

Contents

1	Introduction	19
1.1	Motivation	19
1.2	Relevant Research	21
1.2.1	Capacitive Sensing	21
1.2.2	Biometric and Security Surveillance	23
1.2.3	Feedback for Building Power Level Management	24
2	The Lamp as an ac Source and Capacitive Models	27
2.1	Measuring Electric Flux	27
2.1.1	The Bulb as an Alternating Voltage Source	29
2.1.2	The Alternating Current Measurement	31
2.1.3	The Capacitive Sensing Abstraction	34
2.2	The Practical Alternating Voltage Source	35
2.3	Capacitive Sensing Models	38
2.3.1	Capacitance Model	38
2.3.2	Dielectric Reluctance Model	40
3	Signal Conditioning	45
3.1	Differential Transimpedance Front-End Amplifier for Current-Mode Detection	46
3.1.1	Differential Front-End Operating Principles	48
3.1.2	Differential Transimpedance Amplifier Input Characteristics	51
3.1.3	Feedback Compensation	57

3.1.4	Common-Mode Rejection	63
3.2	Synchronous Detection Operating Principle and Implementation	69
3.2.1	Synchronous Detection Operating Principle	69
3.2.2	Synchronous Detection Implementation	74
3.3	Analog to Digital Interface	80
3.4	Noise Sources	83
4	Expected Output Behavior	93
4.1	Reduced Reluctance and Capacitance Models	93
4.1.1	Stray Capacitances and Negligible Capacitances	94
4.2	Expected Output Response	96
4.2.1	Calculated Output Response	97
4.2.2	Simulated Output Response	102
5	Results, Data Analysis and Demonstration	107
5.1	Measured Output Response and Range Test Data	108
5.2	Signal Source Magnitude Calibration	111
5.3	Real-Time MATLAB Demonstration	113
6	Multiple Electrode Pair System and Further Work	115
6.1	Controlling the Sensing Range	115
6.2	A Prototype Mixed-Signal System for Multiple Electrode Pair Measurements	117
6.2.1	Initial Data and Conclusions	121
6.3	Limitations and Further Work	123
6.3.1	Possible Immediate Improvements	125
A	Lamp Sensor Application Notes	127
A.1	Nulling the Output	127
A.2	Practical Considerations for a Predictable Output	127
B	Software	131
B.1	MATLAB Code	131

B.1.1	takedata.m	131
B.1.2	postprocess.m	132
B.1.3	clearv.m	132
B.1.4	PlotADCroll.m	132
B.1.5	Demo.m	134
B.1.6	Compensation2.m	136
B.1.7	Syncdet.m	137
B.1.8	anacap5.m	138
B.1.9	datatest.m	140
B.1.10	openloopcomp.m	141
B.1.11	idiffthesis.m	142
B.1.12	datatest.m	143
B.1.13	scandata.m	143
B.1.14	clearens.m	144
B.1.15	storecontrol.m	144
B.1.16	storedata.m	145
B.2	C Code for the PIC	145
B.2.1	adc.c	145
B.2.2	Demomaster.c	150
B.2.3	Demoslave.c	156
C	Schematics and PCBs	161
C.1	PCB: Front-End Only	161
C.2	PCB: Full Channel	162

List of Figures

1-1	FSK modulation circuit for transmitting data using a standard fluorescent bulb[15].	19
1-2	Electric field strength simulations of a human walking below a fluorescent lamp.	21
1-3	Lumped element model of a MEMS accelerometer[24].	22
1-4	Generalized block diagram depicting the common detection scheme in the research presented on capacitive sensing.	22
1-5	An electric field depiction of a capacitive sensing scheme for fingerprint reading[29].	24
2-1	Lumped capacitances couple the bulb surface to the electrode and to the ground reference. A voltage relative to the ground reference can be measured at the electrode as ($i_{meas} \times Z_{meas}$).	28
2-2	A conducting target introduces a change in the capacitive coupling and the change in the electrode voltage relative to the ground reference can be measured. A voltage relative to the ground reference can be measured at the electrode as ($i_{meas} \times Z_{meas}$).	29
2-3	The measured fluorescent bulb voltage (a) and current (b) to determine the nominal lengthwise resistance.	30
2-4	The high-impedance ballast current source drives the low-impedance bulb. .	31
2-5	The Thevenin equivalent circuit shows a low-impedance voltage source. . .	31
2-6	A two-electrode set up for differential measurements	36
2-7	A typical lengthwise voltage profile of a fluorescent bulb[10].	36

2-8	Two effective lumped and symmetric alternating voltage sources from the segments of the bulbs nearest the electrodes with the ballast connections to one of the bulbs reversed.	37
2-9	A lumped element capacitive model of the lamp sensor and target system. .	39
2-10	A lumped element dielectric reluctance model of the lamp sensor and target system.	43
3-1	Schematic of the Low-Noise Analog Front-End Amplifier.	48
3-2	The concept of separating differential-mode signals from common-mode signals.	49
3-3	A typical op-amp negative feedback connection	50
3-4	Differential input current in a differential amplifier	51
3-5	A fully differential amplifier taking into account shunt impedances from the measurement nodes to incremental ground.	52
3-6	The half-circuit with incremental grounds for calculating the effect of the shunt impedance on the output voltage.	53
3-7	A current divider between the currents in the op-amp circuit with the op-amp removed.	54
3-8	A differential transimpedance amplifier measuring current through capacitive impedances.	57
3-9	Closed-loop bode plots of the voltage transfer function of the Front-End amplifier with a fixed differential input capacitance. Plots are shown with various feedback capacitances $0 \leq C_f \leq 62 \text{ pF}$ and $R_f = 1 \text{ M}\Omega$	59
3-10	The half-circuit for calculating the stability of the differential front-end amplifier.	60
3-11	The block diagram for the differential closed-loop front-end amplifier system.	60
3-12	Bode plot of the loop transfer function for the uncompensated system ($C_f = 0$) showing poor phase margin.	62

3-13 Bode plot of the compensated loop transfer function showing good phase margin. The addition of C_f in the feedback network is a form of lead compensation.	63
3-14 Bode plot of the compensated system with extra input capacitance showing degraded but acceptable phase margin.	64
3-15 Simplified schematic of THS4140[38].	65
3-16 The differential amplifier with component mismatches.	66
3-17 Basic plot of 1/f noise and thermal noise densities.	70
3-18 Plots of the voltage noise spectral densities for the THS4140 (a) and AD8620 (b)[38][36].	70
3-19 Block diagram of the synchronous detection system	71
3-20 Frequency-domain plot of the modulating signal, carrier signal, and amplifier noise.	72
3-21 Demodulation of the amplified up-modulated signal by multiplication with the carrier.	73
3-22 Output of the synchronous detection system.	73
3-23 Normalized output response of the synchronous detector plotted against phase error between the measured signal and the clock signal.	74
3-24 Clock generation circuit[39].	75
3-25 Fully differential square wave multiplier[41].	76
3-26 Fully differential LPF	77
3-27 The full schematic of the analog receiving network.	79
3-28 Connection diagram of the analog-to-digital interface.	82
3-29 Voltage spectral density of the differential output of the front-end amplifier from dc to 20 kHz showing the 1/f corner.	85
3-30 Voltage spectral density surrounding the carrier frequency of 42 kHz at the differential output of the front-end amplifier with no input signal and the inputs open-circuited. Interference from other lamps appear as stray signals in the plot.	86

3-31 Differential circuit for calculating differential output voltage noise from input-referred current and voltage noise sources.	87
4-1 The full capacitive model of the lamp sensor and target system.	94
4-2 Reduced capacitance model.	95
4-3 Reduced dielectric reluctance model.	96
4-4 Incremental capacitive circuit extracted from the physical model and interfaced with the transimpedance amplifier.	98
4-5 A capacitive half circuit for calculating differential current in the capacitive system.	99
4-6 A dielectric reluctance half circuit for calculating differential electric flux in the capacitive system.	99
4-7 A screenshot of the Fastcap model for the horizontal lamp setup.	103
4-8 A screenshot of the Fastcap model for the hanging lamp setup.	103
4-9 An example of the Fastcap output matrix.	104
4-10 A plot of the simulated output voltage as a human target passes in front of the lamp.	105
4-11 A plot of the simulated output voltage as a human target passes below of the lamp.	105
5-1 A photograph of the cart-mounted prototype lamp sensor.	107
5-2 Examples of plots of sample detections from the range test. [Configuration 44x5]	109
5-3 Overlayed plots of the real output response for calibration of V_s	112
5-4 Tabulated data of the peak deviation of the real output response for calibration of V_s	112
5-5 A screenshot of the real-time Matlab demo.	114
6-1 A plot of the simulated output voltage for varying electrode spacings.	116
6-2 A photograph of the multiple electrode system setup.	118
6-3 A photograph of the multiple electrode pair system electronics.	118

6-4	The connection diagram for the prototype multiple channel system.	120
C-1	A PCB for the front-end amplifier	161
C-2	The single channel prototype lamp sensor mixed-signal PCB.	162

List of Tables

2.1	Capacitance descriptions and nominal values for the full capacitance model.	40
3.1	Significant Noise Sources	92
4.1	Conductors in the Fastcap model.	104
5.1	Detection Data <i>p</i> – <i>values</i> for Various Electrode Configurations at the Limit of the Detection Range.	111
6.1	Detection Data <i>p</i> – <i>values</i> for vertical scans of a human walking below the lamp holding various metallic objects.	122

Chapter 1

Introduction

1.1 Motivation

The ubiquity of fluorescent lighting in public, commercial and work spaces motivates investigation into the potential to exploit the already in place infrastructure of fluorescent lamps for multi-use applications. For example, [15] describes a system which transmits data by modulating the frequency of the light radiated by a fluorescent lamp. With this system, each fluorescent light becomes a versatile data access point that can be used, for example, to transmit location specific audio data to blind customers in a shopping area. The frequency modulating ballast for “Talking Lights” is shown in Figure 1-1.

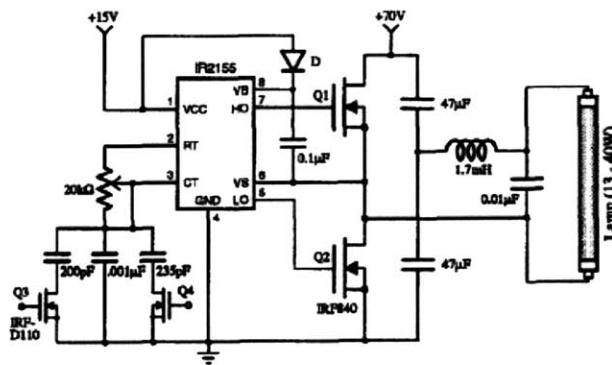


Figure 1-1: FSK modulation circuit for transmitting data using a standard fluorescent bulb[15].

There are many potential advantages of exploiting the fluorescent lamp infrastructure.

The infrastructure provides an omnipresent, controllable light source and alternating electric field source. If the electronics for the system that exploits the fluorescent lamp infrastructure are engineered to not modify the outward appearance and operation of the lamp, a certain level of discreteness is achieved despite the omnipresence of the electronic system. Electronics that are incorporated into the lamp ballast can be installed cost-effectively and without the knowledge of the person who installs them. The electronics do not have to be particularly low-power because they will have access to the same utility power that the lamp ballast uses. Finally, electronics that are installed in all of the fluorescent lamps in a public space result in a macroscopic system that can be networked and controlled remotely. For instance, a power-line modem or a wireless connection could be used to interface a remote PC with each of the lamp sensors.

In particular, the characteristic of the fluorescent lamp infrastructure that this work exploits is that, under normal operation, fluorescent lamps provide an alternating electric field that can be used for sensing applications. This work demonstrates electronics and techniques to measure changes in the electric fields under the lamp and to deduce the presence and motion of conducting or dielectric bodies.

Figure 1-2 shows simulations of how the electric field strength under a fluorescent light bulb changes in the space below the lamp as a human walks by. In the simulation, the fluorescent bulb is a resistive oblong conductor with a piece-wise linear voltage distribution that approximates the low-frequency lengthwise voltage profile of a real fluorescent bulb. The backplane of the lamp is grounded as is the ground below the human. The human is modeled as a six foot tall rectangle composed of salt water. The electric field distribution below the lamp is asymmetric because the voltage profile of the fluorescent bulb is asymmetric. The color gradient from blue to red represents increasing electric field strength.

Potential applications of the sensor system presented in this work include security motion detection, activity level monitoring for power level management, biometric surveillance, and metal or dangerous substance detection. Examples of spaces in which these applications would be appropriate include airports, commercial buildings, prisons, and government or secure buildings.

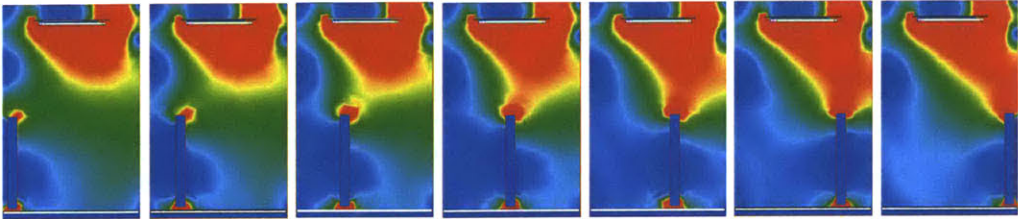


Figure 1-2: Electric field strength simulations of a human walking below a fluorescent lamp.

1.2 Relevant Research

1.2.1 Capacitive Sensing

This work approaches the lamp sensor system as a capacitive sensor in order to simplify the process of measuring electric field changes below the lamp. Therefore, relevant research includes the entire discipline of capacitive sensing and applications. Many references can be cited on this topic; a few are reviewed here.

One of the most contemporary and common applications of capacitive sensors is in micro-electromechanical systems (MEMS) accelerometers. In this case, the MEMS device acts as a capacitive structure and is interfaced with sensing electronics to measure acceleration from the displacement of a mass in a mass-spring system. For example, Hao Luo has presented his research in micro-machined lateral accelerometers [19]. Also, Bliley [2] has presented research in the application of capacitive accelerometers for personal motion data logging. Anwar Sadat has presented research on the design of a MEMS capacitive sensor interfaced with CMOS sensing electronics. Figure 1-3, taken from Sadat[24], shows an example of the capacitive measurement of a displaced proof-mass to deduce acceleration.

In addition to MEMS accelerometers, capacitive sensing is a useful sensing technique in situations requiring non-contact and even high-accuracy measurements. These measurements can be used to measure the physical orientation of conducting and dielectric bodies in 2D and 3D spaces. D. Marioli of the University of Brescia, Italy, has published the paper “High-accuracy Measurement Techniques for Capacitance Transducers[20].” In Marioli’s paper, techniques for signal conditioning and accurately measuring capacitances of interest are discussed as well as topologies for capacitive sensing transducer amplifiers.

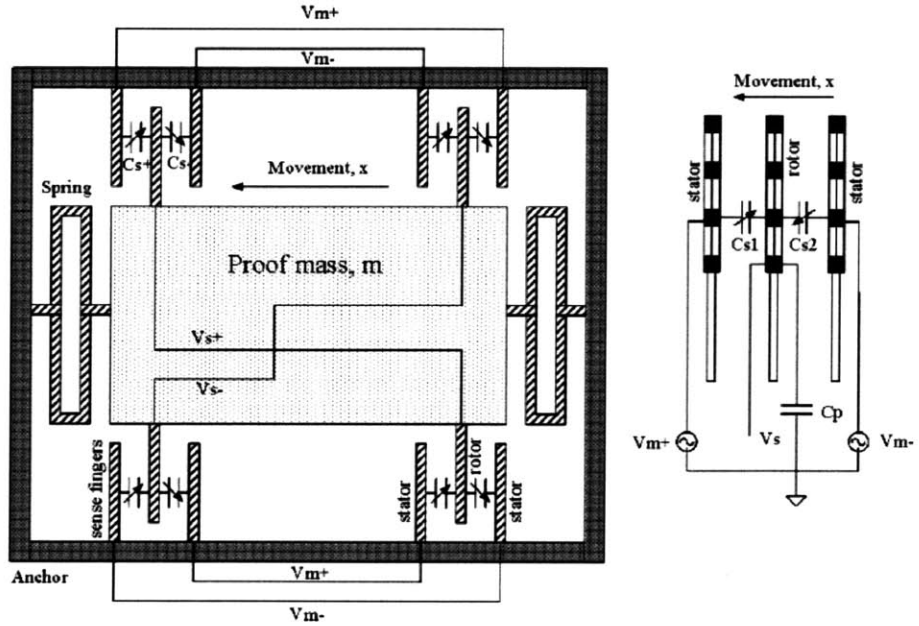


Figure 1-3: Lumped element model of a MEMS accelerometer[24].

J. R. Smith of the Media Laboratory at MIT has published “Field mice: Extracting geometry from electric field measurements[25].” In Smith’s research the goal is actually to detect the human hand as a conducting object amongst electric field sources and sensors. This research in particular has some similarities to the research in this work. The capacitive sensing circuit topology and methodology in the work described above consistently demonstrates similarities to the topology in this work. A generalized block diagram of the common topology is shown in Figure 1-4.

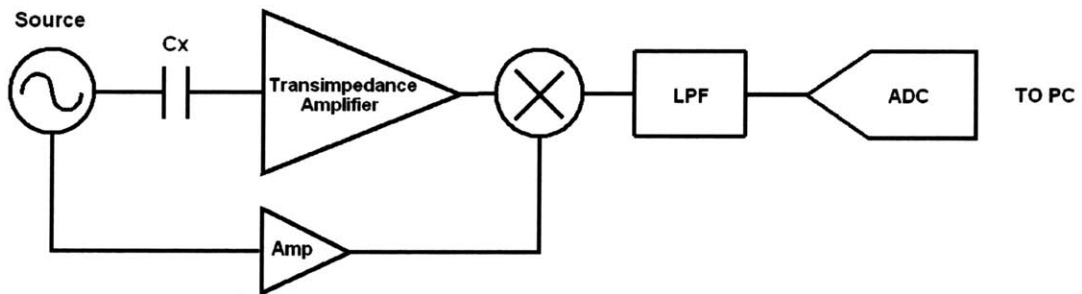


Figure 1-4: Generalized block diagram depicting the common detection scheme in the research presented on capacitive sensing.

The generalized topology uses an ac signal source to drive current through the capacitance to be measured, shown in the diagram as Cx. It often measures the current through

the capacitance, C_x with a transimpedance amplifier (although Sadat's system is an example in which the sensing electronics take a voltage measurement using an operational transconductance amplifier (OTA)[24]). The common topology then uses some form of synchronous detection to condition the output of the front-end amplifier by multiplying the measured signal with the signal source. Finally, the signal is digitized for processing with a computer. The topology presented in this work, although similar on a high level to many of the topologies presented for capacitive sensing, is designed particularly for the lamp sensor application and presents some particular advantages over the common detection topologies that allow for useable detection ranges in the unfriendly and not well-controlled environment below a fluorescent lamp.

1.2.2 Biometric and Security Surveillance

One of the principle motivating factors of this research has been the potential to use the lamp sensor as a security detection device. This work presents circuitry and detection methods which prove the lamp sensor to be useful at the very least as a motion detection system. Further, we are exploring the possibility of more sophisticated biometric surveillance in which we will attempt to extract vertical profiles of the dielectric and conductive make-up of a person below the lamp by controlling the sensing range. The ability to perform Electrical Capacitance Tomography may be possible by controlling the sensing range with the system that will be presented in Chapter 6. Some relevant research in discrete, widespread security surveillance systems as well as electrical capacitance tomography (ECT) is summarized here.

Fong [11] has presented research in security systems in which he discusses a widespread networked security surveillance systems using web-based communication to interface multiple security devices. The lamp sensor could be used in this context as a security device which can be interfaced on a large scale with other lamp sensors.

Professor Wuqiang Yang at the University of Manchester Institute of Science and Technology, U.K. has presented research in ECT[34]. Professor Yang's research uses capacitive sensing techniques to map the electric fields in spaces occupied by conductive and dielec-

tric liquids and gases.

Thomas Heseltine has presented research in ECT in which he uses capacitive sensors to generate a 3D map of a human face[14]. Applications of Heseltine's work include security, surveillance, and archive searching. In this case, Heseltine treats the face as an "eigensurface." This refers to the "inverse problem" that Yang [34] discusses in his research in which the shape of the conductive or dielectric body measured by the capacitive sensor system is deduced from multiple electrode measurements. Marco Tartagni presents a capacitive sensing scheme for non-contact measurements of human fingerprints for identification purposes. Figure 1-5 shows the electric field depiction of the capacitive sensing scheme that Tartagni employs in his fingerprint reader.

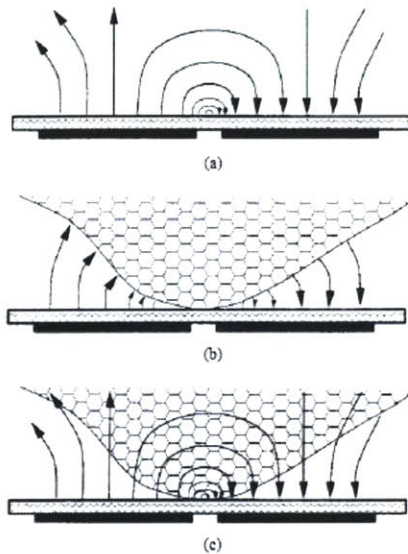


Fig. 4. (a) Parasitic feedback capacitance and (b), (c) sensing principle.

Figure 1-5: An electric field depiction of a capacitive sensing scheme for fingerprint reading[29].

1.2.3 Feedback for Building Power Level Management

Commercial buildings and residences and industrial shops and factories are often designed primarily to fulfill their role of providing occupants with space. The cost of operating these buildings is frequently a secondary consideration, at least until operating expenses force a reconsideration of operating behavior and the installed physical plant. There is

an exploding interest in making buildings more economical to operate while maintaining occupant comfort. Operating costs matter, and will become even more important in the future. A unique opportunity for energy conservation is becoming technically feasible.

We are developing mathematical tools to develop accurate models of a building's environment (temperature, for example) in response to important variables like occupancy, electrical loading, outdoor weather, and heating, ventilation, and air-conditioning (HVAC) operating parameters. These models require fine-grain occupancy measurements taken at known positions in a building. Easy proximity detection of people makes it easy to collect this data. These models make it possible, for example, to examine the effect of a reduction in HVAC plant operating costs on occupant comfort[6].

Professor Steven Leeb has presented research in the area of non-intrusive load monitoring for building power level management[16] [9] [17]. Leeb's research examines non-intrusive power building-level power network analysis for improved efficiency in power usage.

Chapter 2

The Lamp as an ac Source and Capacitive Models

The first task in understanding how a fluorescent lamp can be used as a sensing device is in characterizing the lamp as an electric signal source. With sufficient understanding of the signal source, the lamp sensor system can be simplified and an electrical model can be extracted that will predict the output response of the system. If the output response of the real system matches the response that was predicted by the model, then we can be confident that we understand the basic operating principles behind the lamp sensor and thus make intelligent decisions in engineering the system performance.

2.1 Measuring Electric Flux

Generally speaking, we initially expect the lamp sensor to work as follows. Under normal operation, the bulb surface potential varies with respect to an incremental ground reference as the ballast drives current through it. The incremental ground reference for the lamp sensor is discussed in Section 2.2.¹ Electric field couples the surface of the bulb to conducting surfaces below the lamp and to the ground reference. The electric field below the lamp can be sensed by measuring the voltage of an electrode placed in front of the bulb relative to

¹The effect of earth-grounded surfaces including the backplane behind the bulbs and the floor below the lamp will be examined in Chapter 4.

the ground reference. The behavior of the electric fields can be modeled with lumped capacitances between the conducting surfaces. The specifics of the capacitive model used in this work will be developed in the coming Chapters. A qualitative picture of the capacitive coupling between the conducting surfaces and the ground reference is shown in Figure 2-1, in which the voltage of the electrode is the result of the capacitive voltage divider formed by C_1 and C_2 and it is measured as the product of the current i_{meas} and the impedance Z_{meas} .

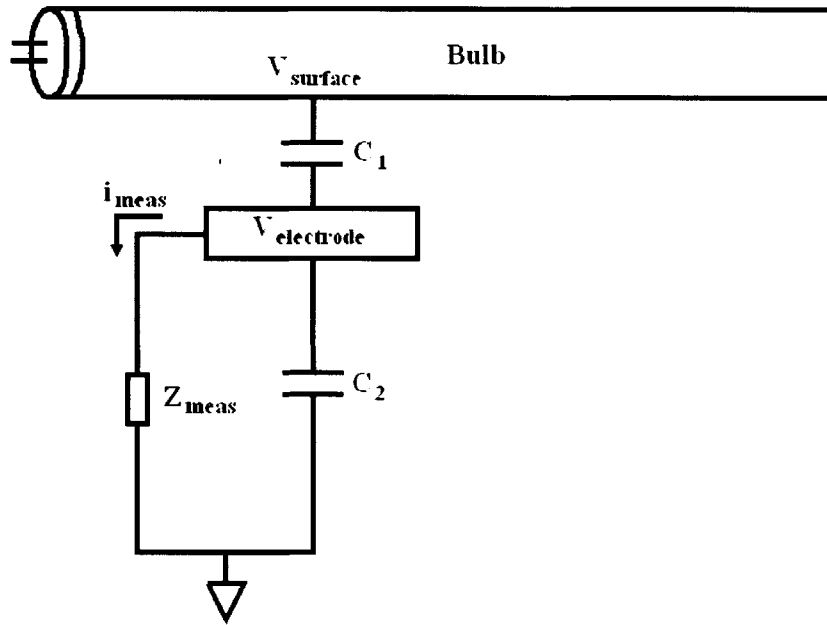


Figure 2-1: Lumped capacitances couple the bulb surface to the electrode and to the ground reference. A voltage relative to the ground reference can be measured at the electrode as ($i_{meas} \times Z_{meas}$).

When a conductive or dielectric target such as a human is present below the lamp, it distorts the electric field below the lamp and therefore changes the capacitive coupling between the conducting surfaces. The change in the capacitive coupling can also be measured at the electrode as a change in the electrode voltage relative to the ground reference. A qualitative picture showing the capacitive coupling below the lamp with a conducting target is shown in Figure 2-2.

The particular manner in which the electric field distribution changes and therefore how changes in the capacitive coupling are measured, depends on how the source is characterized. If the source were characterized as an alternating current source or a high impedance

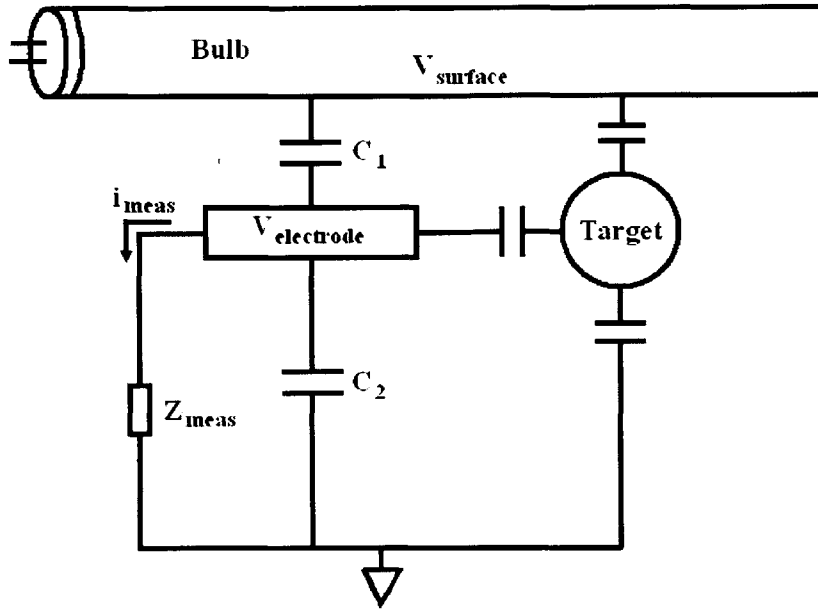


Figure 2-2: A conducting target introduces a change in the capacitive coupling and the change in the electrode voltage relative to the ground reference can be measured. A voltage relative to the ground reference can be measured at the electrode as ($i_{\text{meas}} \times Z_{\text{meas}}$).

source, then the total electric flux from the surface of the bulb would be fixed. In that case, a target would divert some of the electric flux away from the measurement electrode and we would measure a reduction in the electric flux incident on the electrode. If the source were characterized as an alternating voltage source, or a low impedance source, then the surface potential of the bulb would be fixed relative to the ground reference and the total electric flux from the surface of the bulb would vary in response to a target. Therefore, the first task is to understand whether the bulb should be characterized as an alternating current source or an alternating voltage source.

2.1.1 The Bulb as an Alternating Voltage Source

To determine the appropriate source characterization, consider the source and loading impedances. The lengthwise impedance along the length of the bulb was measured as the ratio of the root-mean-square (rms) voltage across the bulb to the rms current through the bulb. This measurement gives a nominal resistance of 900Ω . Scope traces of the bulb current and voltage are shown in Figure 2-3.

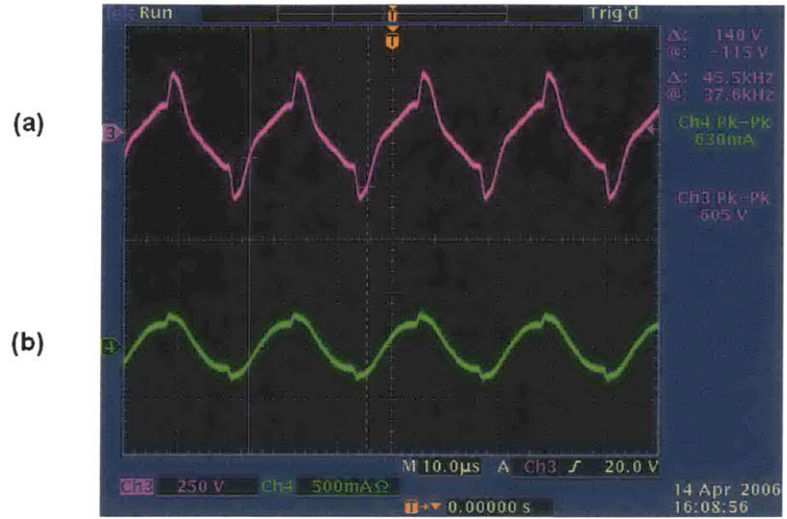


Figure 2-3: The measured fluorescent bulb voltage (a) and current (b) to determine the nominal lengthwise resistance.

The loading impedances on the source will be capacitive impedances from the surface of the bulb to the conducting bodies in the system. These capacitances will be shown to have maximum nominal values of about 1 pF. The fundamental signal frequency of the source, ω , is taken from the ballast operating frequency of 42 kHz. Therefore the smallest nominal capacitive impedance in the system will be approximately

$$|Z_{c,min}| = \frac{1}{\omega C_{max}} \quad (2.1)$$

$$= \frac{1}{2\pi \times 42 \text{ kHz} \times 1 \text{ pF}} \quad (2.2)$$

$$|Z_{c,min}| = 3.8 \text{ M}\Omega. \quad (2.3)$$

Conducting bodies below the lamp will divert some alternating current via these capacitive impedances providing a high-impedance path from one point on the surface of the bulb to other conducting surfaces or to the ground reference. Although the ballast itself is a high-impedance current source, the capacitive impedances from the bulb surface to the conducting and dielectric bodies below the lamp will see the bulbs as a low-impedance voltage source. Figure 2-4 shows the situation in which the ballast current drives the low-impedance bulb. Alternating current is diverted from the surface of the bulb at points

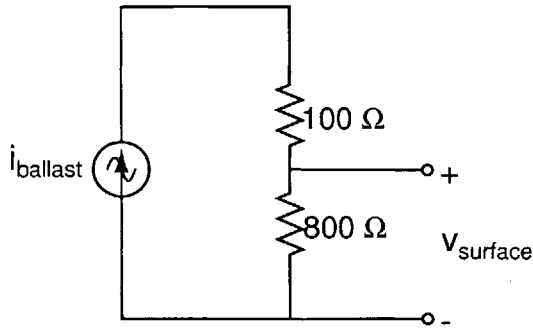


Figure 2-4: The high-impedance ballast current source drives the low-impedance bulb.

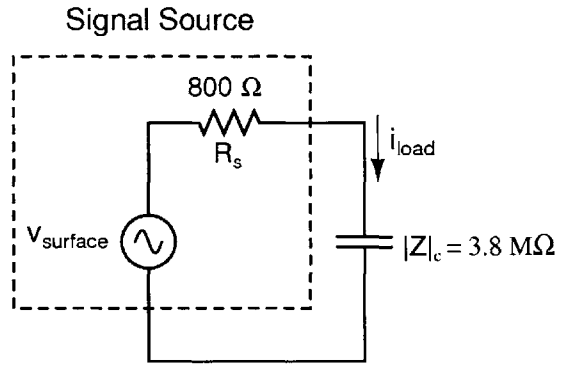


Figure 2-5: The Thevenin equivalent circuit shows a low-impedance voltage source.

between the two ends of the bulb. Considering only one point at a time, labeled in Figure 2-4 as V_{surface} , the bulb and ballast source can be drawn as a Thevenin equivalent circuit shown in Figure 2-5. In the Thevenin equivalent circuit, the source appears to the capacitive load as a low-impedance voltage source. The bulbs as an electrical signal source are therefore treated as an alternating voltage source.

2.1.2 The Alternating Current Measurement

Considering the bulb surface as an alternating voltage source implies the manner in which the target will distort the electric fields below the lamp and therefore the manner in which the target will be detected. In order to develop intuition about the way that the electric field must change in response to a target, first note that the electric field (E-field) must terminate perpendicularly to any conducting surface (inasmuch as that surface is perfectly conducting). Second, note that the potential difference between any two points is equal to the line integral of the electric field vector between those two points.

$$\phi(t) = \int_a^b \vec{E}(r, t) \cdot d\vec{r} \quad (2.4)$$

The fact that the bulb acts approximately as a voltage source or a low-impedance source means that the potential difference between a fixed potential surface and the bulb must remain constant despite electric field distortions. Therefore, a conducting target in the detec-

tion field distorts the electric field in such a way that the field lines terminate perpendicular to the target surface and that the line integral of the vector electric field between any two fixed potentials remains constant.

The E-field perpendicular to a conducting surface is proportional to the surface charge density on that surface. In other words, the total electric flux on a conducting surface is equal to the ratio of the total surface charge Q_s to the dielectric constant ϵ of the medium in which the E-field exists:

$$\Phi_e = \int_A \vec{E} \cdot d\vec{A} = \frac{Q_s}{\epsilon}, \quad (2.5)$$

where Φ_e is the electric flux calculated as the surface integral of the electric field. If Q_s on the surface of the conductor is reduced, the total E-field incident on the conducting surface or Φ_e is reduced and vice versa. The presence of the conducting target in the detection field means that some charge on the surface of the target can balance some of the charge on the surface of the bulb or any other conductor in the system by the electric flux linking the two surfaces. Therefore, we intend to measure electric flux Φ_e at the electrode by measuring varying surface charge on the electrode in order to measure electric field distortions below the lamp.

The ballast drives the fluorescent bulb with an alternating current. Assuming that the bulb has some finite impedance, there is some alternating voltage drop across it. Taking only the segment of the bulb behind the electrode, the potential there varies as an ac voltage about some average potential with the ballast operating frequency. The time-varying bulb surface potential $\phi(t)$ is

$$\phi(t) = - \int_{\infty}^R \vec{E}(r, t) \cdot d\vec{r}, \quad (2.6)$$

where R is the radius of the bulb. The time-varying E-field, $\Delta E(t)$, from each incremental bulb surface area segment, ΔA , varies with the distance from the bulb surface as

$$\Delta \vec{E}(t) = \frac{\Delta Q(t)}{4\pi\epsilon r^2} \hat{r}, \quad (2.7)$$

where $\Delta Q(t)$ is the surface charge on the infinitesimal bulb surface area ΔA and \hat{r} is the

direction radially outward from the center of the bulb. Then, from (2.6),

$$\Delta\phi(t) = \frac{\Delta Q(t)}{4\pi\epsilon R}. \quad (2.8)$$

Therefore, the surface charge on the bulb varies as the surface potential varies with the ballast operating frequency. Finally, the electric flux from the surface of the bulb alternates with the operating frequency of the ballast from (2.5) and (2.8) and that alternating electric flux couples the bulb surface to other conducting surfaces including the electrodes. In order to measure the electric flux at the electrode, a measurement is taken of the alternating current that couples from the surface of the bulb to the electrode. The time-varying incremental surface charge on the electrode is

$$\Delta Q(t) = \epsilon \Delta \Phi_e(t), \quad (2.9)$$

where $\Delta \Phi_e(t)$ is the incremental electric flux at the electrode and the incremental surface potential in terms of the incremental electric flux from the surface of the bulb is

$$\Delta\phi(t) = \frac{\Delta\Phi_e(t)}{4\pi R}. \quad (2.10)$$

The current measured at the electrode is

$$i(t) = \frac{d}{dt} Q(t), \quad (2.11)$$

where $Q(t)$ is the integral of the incremental surface charge on the electrode over the surface area of the electrode. From (2.11) and (2.9), each frequency component of the alternating electric flux at the electrode gives rise to a frequency component of the alternating current at the electrode. For each frequency component of the alternating electric flux,

$$\Phi_e(t) = \Phi_{eo} \sin(\omega t). \quad (2.12)$$

Then, the alternating current is found from the time derivative of the surface charge in terms

of electric flux as

$$i(t) = \epsilon \frac{d}{dt} \Phi_e(t). \quad (2.13)$$

Finally, the alternating current in terms of the magnitude of the electric flux at the electrode is

$$i(t) = \epsilon \omega \Phi_o \cos(\omega t). \quad (2.14)$$

There is a phase shift of 90° between the alternating electric flux and the alternating current measured at the electrode. The alternating current measured at the electrode then is a 90° phase shifted version of the alternating electric flux scaled by the factor $\epsilon\omega$. Then, the conducting electrode can be thought of as an alternating electric flux-to-alternating current transducer that adds an inherent 90° phase shift and scales by the factor $\epsilon\omega$ for correct units. In order to measure electric flux with a current measurement, the frequency of the alternating surface potential on the bulb must be nonzero due to the factor of ω in $i(t)$, so our source must be an ac electric signal source.

2.1.3 The Capacitive Sensing Abstraction

Capacitance between two conductors is the ratio of the total charge on each conductor to the voltage between the two conductors for all time:

$$Cv_c(t) = Q_c(t). \quad (2.15)$$

In (2.15), C is constant in time, $v_c(t)$ is the alternating voltage between the two conductors and $Q_c(t)$ is the alternating total surface charge on either conductor. Then, capacitance can be rewritten in terms of alternating electric flux, $\Phi_e(t)$, as

$$C = \frac{\epsilon \int_A \vec{E}(t) \cdot d\vec{A}}{\int_s \vec{E}(t) \cdot d\vec{s}} = \epsilon \frac{\Phi_e(t)}{v_c(t)}. \quad (2.16)$$

Solving for the alternating current at the electrode,

$$i(t) = \frac{d}{dt} Q(t), \quad (2.17)$$

with the definition of capacitance,

$$i(t) = \frac{d}{dt}(Cv_c(t)) = \frac{d}{dt} \left(\frac{\epsilon\Phi_e(t)v_c(t)}{v_c(t)} \right) \quad (2.18)$$

$$= \frac{d}{dt}\epsilon\Phi_e(t) = \epsilon \frac{d}{dt}[\Phi_{eo} \sin(\omega t)]. \quad (2.19)$$

Therefore, the current in a capacitor in terms of the magnitude of the flux linking its two conductors is

$$i(t) = \epsilon\omega\Phi_{eo} \cos(\omega t) \quad (2.20)$$

which is consistent with the form of $i(t)$ in (2.14). So we have a capacitive sensor for which

$$v_c(\omega t) = \frac{\epsilon\Phi_e(t)}{C} = \frac{\epsilon\Phi_{eo} \sin(\omega t)}{C} \quad (2.21)$$

from (2.16). Then, from (2.14) and (2.21) the capacitive reactances are as expected:

$$X_c(\omega) \equiv \frac{|v_c(\omega t)|}{|i_c(\omega t)|} = \frac{\epsilon\Phi_{eo}}{C\epsilon\omega\Phi_{eo}} = \frac{1}{\omega C}, \quad (2.22)$$

so that for a fixed magnitude of alternating voltage $|v_c(t)|$, the alternating current magnitude $|i_c(t)|$ increases with capacitance C and frequency ω . It is more convenient to measure the rms current at the electrodes,

$$i_{rms} = \frac{|i(t)|}{\sqrt{2}} = \frac{\epsilon\omega\Phi_e}{\sqrt{2}} \quad (2.23)$$

in terms of, Φ_e , the magnitude of each sinusoidal frequency component of the electric flux. For an arbitrary periodic drive the currents will add in quadrature according to the electric flux magnitude Φ_n of each frequency component n with frequency ω_n as

$$i_{rms} = \frac{\epsilon}{\sqrt{2}} \sqrt{[\Phi_0^2\omega_0^2 + \Phi_1^2\omega_1^2 + \Phi_2^2\omega_2^2 + \dots]} \quad (2.24)$$

2.2 The Practical Alternating Voltage Source

In the lamp sensor system, detection is approached with a differential and nulled measurement between two electrodes. The differentially nulled measurement requires symmetry

about the center of the lamp. Therefore, the two electrodes need to couple to two equivalent voltage sources. The necessary symmetry is achieved using two electrodes spanning two bulbs symmetrically as shown in Figure 2-6.

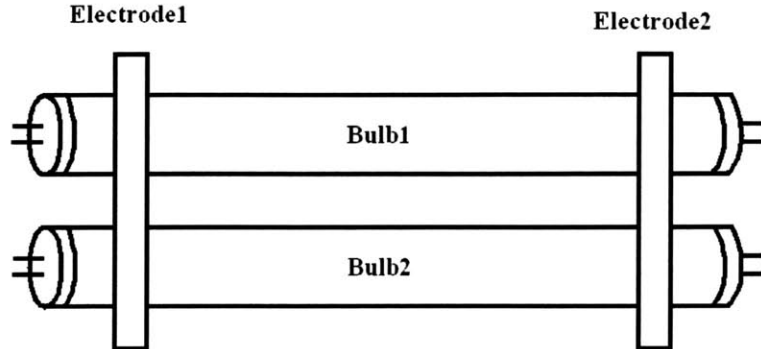


Figure 2-6: A two-electrode set up for differential measurements

The lamp segments behind each electrode can be abstracted as effective alternating voltage sources. Ideally, this configuration provides two lumped and symmetric effective voltage sources behind the electrodes. Under normal operation, the ballast drives the fluorescent bulbs in phase, meaning that the current through each bulb is instantaneously flowing in the same direction. The profile of the lengthwise bulb voltage due to the ballast current relative to one end of the bulb is nonlinear and asymmetric. A typical voltage profile of a fluorescent bulb is shown in Figure 2-7 provided by [10].

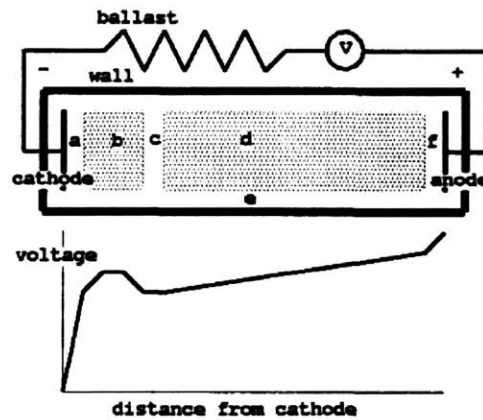


Figure 2-7: A typical lengthwise voltage profile of a fluorescent bulb[10].

To create symmetric effective voltage sources with respect to the center of the bulb, the

ballast connection to one of the two bulbs is reversed so that the bulbs are driven opposite each other. In that case, with the electrodes equidistant from the center of the lamp, the summed voltages relative to the center of the lamp due to the bulb segments behind the electrodes are the same for the both electrodes.

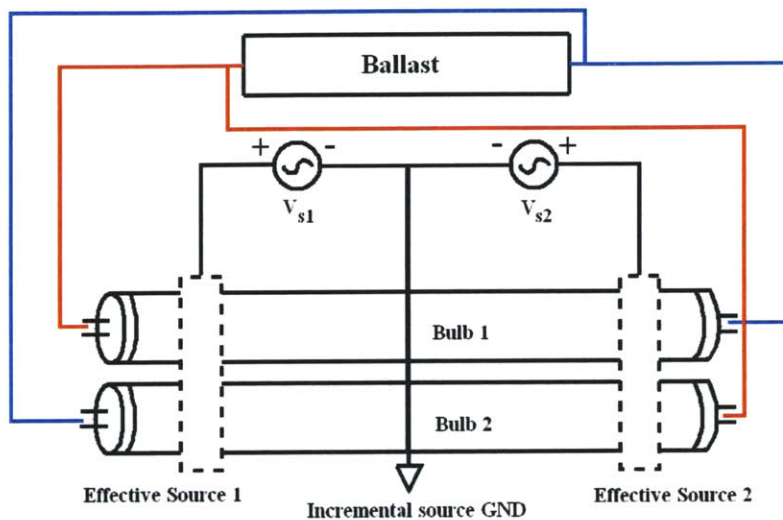


Figure 2-8: Two effective lumped and symmetric alternating voltage sources from the segments of the bulbs nearest the electrodes with the ballast connections to one of the bulbs reversed.

With two symmetric alternating voltage sources, the lamp as an alternating voltage source can be lumped and abstracted as in Figure 2-8. The two effective voltage sources V_{s1} and V_{s2} are equal to each other with respect to the center of the lamp. Therefore, the ground reference for the differential measurement is the potential at the center of the lamp and it is labeled in the picture as “Incremental source GND”. In the capacitive measurement scheme, the effective magnitude of the voltage sources is some ac rms voltage. Obtaining a value for the effective magnitude, however, is complicated because it depends on the particular geometry of the lamp, the electrode configuration and on the nonlinear voltage profile of the bulbs. Because the value of the voltage source magnitude is only useful for simulating absolute responses, it is not directly measured, although it will be inferred in Chapter 5 by comparing a real response to a simulated response.

2.3 Capacitive Sensing Models

With an understanding of the lamp as an electrical signal source, a capacitive model can be constructed that will be used to model the behavior of the electric fields below the lamp in response to a conducting or dielectric target. The abstraction of the effective and symmetrical voltage sources allows for a simplified lumped element model of the lamp sensor and target system. That lumped element model will be presented in two ways in this section.

2.3.1 Capacitance Model

As shown in section 2.1.3, measuring the electric flux that is incident on the measurement electrodes amounts to measuring capacitances in the lamp sensor and target system. Therefore, it is simplifying and useful to build a lumped element model of the capacitances between each of the conducting bodies in the lamp sensor and target system. Using this model, intelligent decisions about detection schemes can be made and an understanding of the output response of the lamp sensor system to a specific motion or body below the lamp can be achieved. Interfacing the capacitive model with the signal conditioning electronics of Chapter 3, and simulating the capacitances in the system, an expected output response can be attained.

By taking into account the capacitances between each of the conducting or dielectric bodies in the lamp sensor and target system, a full capacitive model like that in Figure 2-9, is obtained. In this model, the sources are shown as voltage sources V_{s1} and V_{s2} , referenced to the ground reference at the center of the lamp and the circuit elements are capacitances. Consequently, the signals in the system are alternating currents. Also shown are the earth ground connections for the backplane of the lamp and the floor beneath the lamp and the target. The conventional ground symbol represents earth ground or a surface connected to earth ground and the ground symbol shown as a hollow arrow head is used to represent the incremental source ground.

Because the goal is to measure changes in the electric fields below the lamp, it will also be useful to derive a lumped element circuit model of the lamp sensor and target system

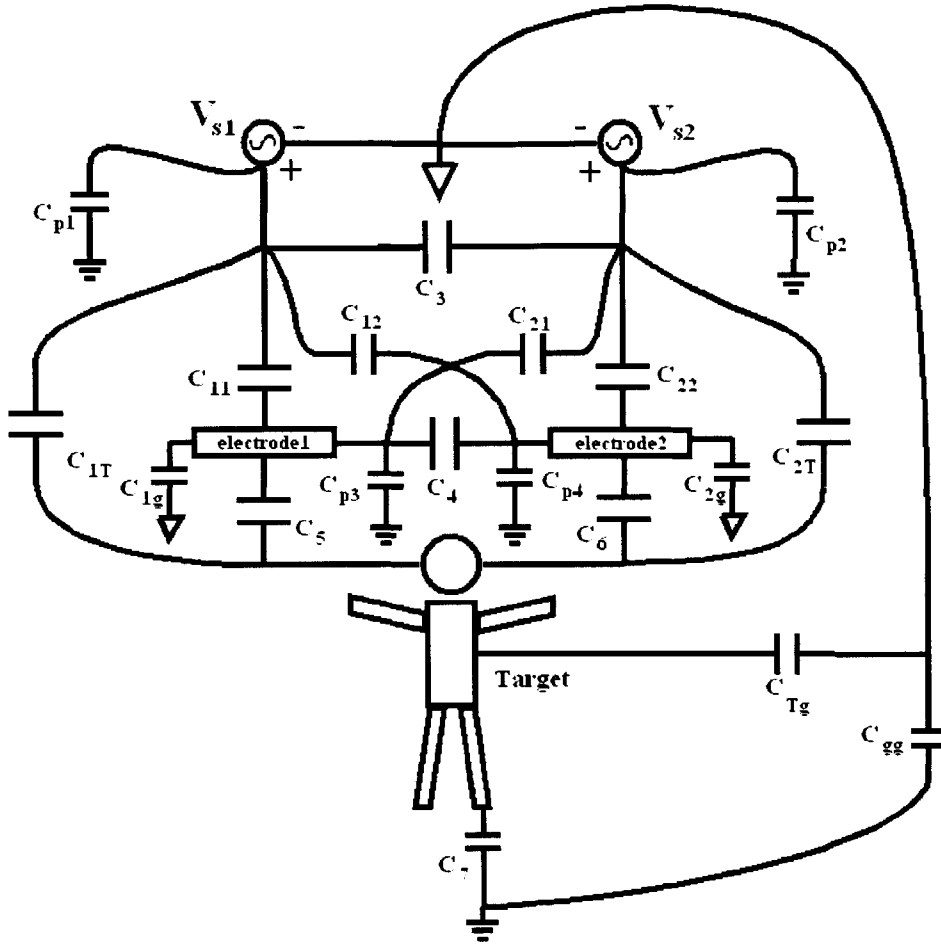


Figure 2-9: A lumped element capacitive model of the lamp sensor and target system.

that treats the signals in the system as electric flux. The model which treats the signals as electric flux will be presented in Section 2.3.2.

In Figure 2-9, capacitances are shown between the signal sources and the electrodes, ground or incremental ground potentials, and the target. For instance, capacitance C_{12} is the capacitance between the left-most voltage source and the right-most electrode. Physically, this is the lumped capacitance between the bulb surfaces behind the left-most electrode and the surface of the right-most electrode. Table 2.1 gives a physical description of each of the capacitances shown in the model and nominal values obtained from the finite element modeling software FastCap[21]. The lower bounds on the range of nominal values for the capacitances C_{1T} , C_{2T} , C_5 and C_6 are the smallest measurable capacitances for the system presented in this work.

Table 2.1: Capacitance descriptions and nominal values for the full capacitance model.

Label	Physical Description	Nominal Value(s)
C_{p1}	Left source to backplane	10 pF
C_{p2}	Right source to backplane	10 pF
C_3	Left source to right source	10 pF
C_{11}	Left source to left electrode	2 pF
C_{22}	Right source to right electrode	2 pF
C_{12}	Left source to right electrode	100 fF
C_{21}	Right source to left electrode	100 fF
C_{1T}	Left source to target	10 fF-1 pF
C_{2T}	Right source to target	10 fF-1 pF
C_4	Left electrode to right electrode	500 fF
C_5	Left electrode to target	10 fF-1 pF
C_6	Right electrode to target	10 fF-1 pF
C_{p3}	Left electrode to backplane	1 pF
C_{p4}	Right electrode to backplane	1 pF
C_7	Target to floor	10 pF
C_{gg}	Floor to incremental bulb ground	1 pF
C_{Tg}	Target to incremental bulb ground	1 pF
C_{1g}	Left electrode to incremental bulb ground	1 pF
C_{2g}	Right electrode to incremental bulb ground	1 pF

The capacitances $C_{p1,2}$ are parasitic or stray capacitances from the bulbs to earth ground. In this case, $C_{p1,2}$ are dominated by the capacitances from the bulbs to the backplane but also include the capacitances from the bulbs to the floor.

Many of the capacitances in the full capacitance model in Figure 2-9 will not end up affecting the output response or will be negligible compared to other capacitances. Therefore, a reduced capacitance model will be explained and presented in Chapter 4. Also, some capacitances are assumed to be fixed while others change as the target moves below the lamp. Capacitances which are assumed to be fixed include capacitances between any two conductors that are fixed in space. Capacitances which change include any capacitances between a fixed conductor and the target.

2.3.2 Dielectric Reluctance Model

In Section 2.3.1, the lumped element circuit model of the lamp sensor and target system consisted of capacitances. In the capacitive model, the signal sources were voltage sources

and the signals in the circuit elements were currents. We would like to develop some intuition about the behavior of the system with respect to how it measures changes in the electric fields. Therefore, it will also be useful to build a lumped element circuit model in which the signals in the circuit are electric flux. To quantify the behavior of electric flux below the lamp, we introduce a quantity called dielectric reluctance, \mathcal{T} , which acts on electric flux as an impedance acts on current.

The dielectric reluctance between conductors a and b , \mathcal{T}_{ab} , is the ratio of the electromotive force (EMF) between two conductors, \mathcal{E}_{ab} to the electric flux coupling the two conductors, $\Phi_{e,ab}$.

$$\mathcal{T}_{ab} \equiv \frac{\mathcal{E}_{ab}}{\Phi_{e,ab}} \quad (2.25)$$

Casting this definition in terms of capacitance by recognizing EMF to be equivalent to voltage,

$$Q_{a,b} = \epsilon_{ab}\Phi_{e,ab} \quad (2.26)$$

$$Q_{a,b} = C_{ab}V_{ab} \quad (2.27)$$

$$\mathcal{T}_{ab} = \frac{\epsilon_{ab}V_{ab}}{Q_{a,b}} \quad (2.28)$$

$$(2.29)$$

If follows that

$$\boxed{\mathcal{T}_{ab} = \frac{\epsilon_{ab}}{C_{ab}}}. \quad (2.30)$$

So that dielectric reluctance as defined above is the ratio of the permittivity of the space between the two conductors to the capacitance between them. For a fixed operating frequency, this quantity will be directly proportional to the capacitive impedance magnitude,

$$|Z_c| = \frac{1}{\omega C}. \quad (2.31)$$

An analogy can be drawn between the EMF source and dielectric reluctance system and a simple voltage source and resistance system. In this analogy, electric-flux becomes

current and dielectric reluctance becomes resistance.

$$\Phi_e \cdot e^{j\frac{\pi}{2}} \rightarrow i \quad (2.32)$$

$$T \rightarrow R, \quad (2.33)$$

where the exponential term represents the phase shift from the current to the electric flux.

Also, in this analogy, voltage remains as voltage because the analogous quantity \mathcal{E}_{ab} will be

$$\mathcal{E}_{ab} = T_{ab}\Phi_{e,ab} \quad (2.34)$$

$$= \frac{\epsilon_{ab}}{C_{ab}} \frac{Q_{a,b}}{\epsilon_{ab}}. \quad (2.35)$$

Using the definition of capacitance, the EMF becomes voltage:

$$C \equiv \frac{Q}{V} \quad (2.36)$$

$$\mathcal{E}_{ab} \rightarrow V_{ab}, \quad (2.37)$$

which is simply a consequence of the fact that EMF is physically indistinguishable from voltage. It is important not to confuse the current i in this analogy with the real measured current from (2.11) in the capacitive model. Because the current in this analogy represents electric flux, there is a 90° phase shift between it and the real current in the capacitive model and they cannot be the same quantity.

The full dielectric reluctance circuit model is shown in Figure 2-10. In this model, all of the capacitances are replaced with dielectric reluctances according to (2.30) while the voltage sources are replaced with EMF sources. The electric flux signals act on dielectric reluctances as currents do on impedances.

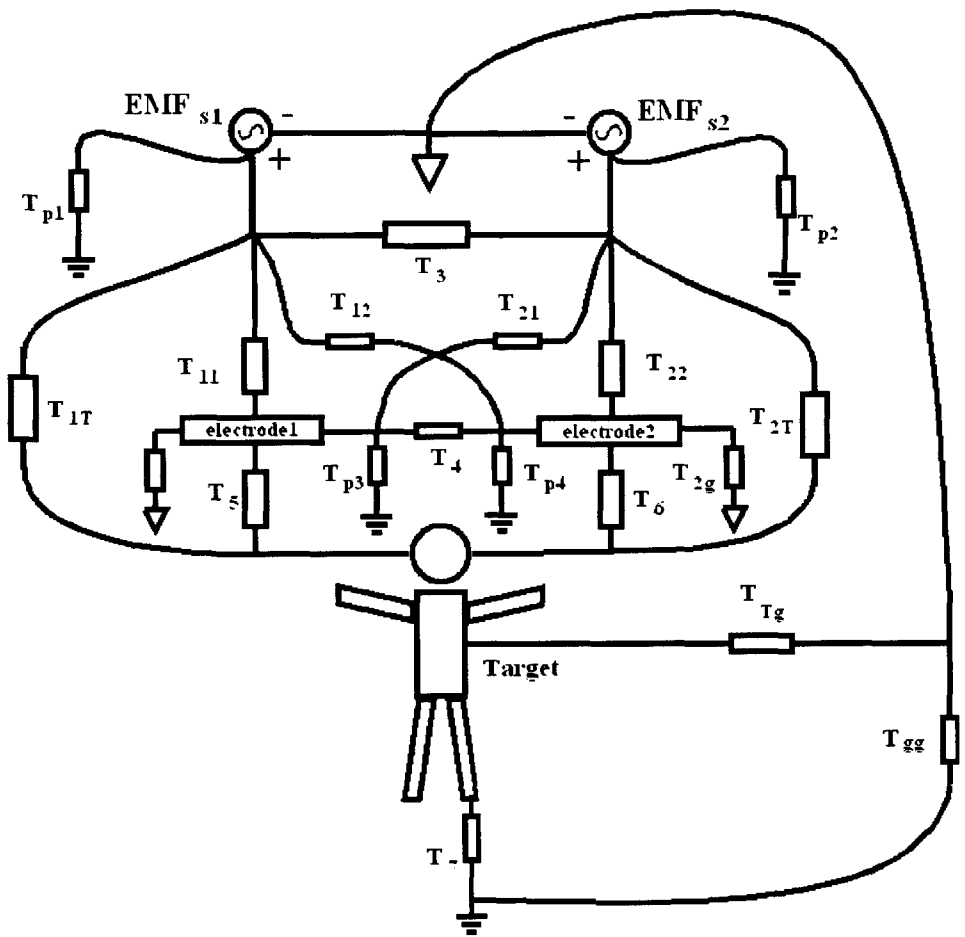


Figure 2-10: A lumped element dielectric reluctance model of the lamp sensor and target system.

Chapter 3

Signal Conditioning

In Chapter 2, the lamp was considered as an ac electrical signal source. A lumped element circuit was derived that models the behavior of the electric fields below the lamp in response to the conducting target. The next task is to design electronics to condition a signal from the lumped element circuit to detect the conducting target. The interface between the lumped element circuit and the signal conditioning electronics is the measurement electrodes placed in front of the lamp.

Detection is approached by measurement of differential signals in a nullable, balanced capacitive bridge. Because the nulling is capacitive and based on the geometry of sensing, as opposed to nulling at an op-amp summing junction, it is noise-free. Measuring changes in capacitances below the lamp as deviations from the nulled output has the advantage that the front-end amplifier can have very high gain without saturating its output in the absence of a detection. More subtly, a differential measurement of the electric fields below the lamp eliminates the need for a well-controlled dc voltage reference for detection. The output of the ballast is isolated so that there is theoretically no dc path from the output of the ballast to ground and ac impedances to ground are not controlled, therefore, the potential differences between the bulb surface and for instance, the grounded backplane of the lamp are not predictable.

The solution to the problem of not having a well-controlled voltage reference is an important innovation. The fact that the system is designed to be independent of any absolute ground reference is extremely advantageous for capacitive sensing applications. The only

ground reference that sensing will depend on is the inherent incremental source ground at the center of the lamp source. Particular advantages include that common-mode variations in the ground reference and reactive ground loops can be ignored, and that the target need not be coupled to earth ground in order to be detected.

The topology remains fully differential until digitization because this has the advantage of rejecting common-mode pick-up from interfering signals including 60 Hz ac from the utility power line within the signal conditioning electronics. Also, current-mode detection was chosen because it is insensitive to stray shunt capacitances at the measurement electrodes. Therefore, the front-end amplifier is a fully differential transimpedance amplifier for current-mode sensing.

The signal conditioning circuitry consists of the front-end amplifier, a synchronous demodulator, and an analog-to-digital interface. The basic operating principles include current-mode sensing to measure the electric flux at the measurement electrodes, and synchronous detection. This chapter concludes with a discussion of the noise sources which ultimately limit the detection range and resolution of the lamp sensor.

In summary, the important contributions and innovations presented in this Chapter are as follows. Sensing signals are conditioned from a nullable capacitive bridge. Nulling the output allows for a large differential gain in the front-end amplifier and the nulling is noiseless because it is capacitive and based on the geometry of the sensor. The differential measurement also removes the necessity for a well-controlled dc voltage reference which may be prone to uncontrolled voltage variations with respect to the alternating bulb surface potential. Finally, synchronous detection of the lamp signal provides insensitivity to stray signals.

3.1 Differential Transimpedance Front-End Amplifier for Current-Mode Detection

A schematic of the fully-differential front-end amplifier is shown in Figure 3-1. The fully differential amplifier in the front-end amplifier is the Texas Instruments part THS4140 [38].

This part was chosen for its sufficiently high Gain-Bandwidth (GBW) product of 150 MHz and for its dual-rail supply voltage capability. The front-end amplifier incorporates two JFET buffer amplifiers as the Analog Devices part AD8620[36]. This JFET op-amp was chosen to have very low input-referred current noise, as will be discussed in Section 3.4, and to have very low input bias current. Because the front-end amplifier will need to have a very large transimpedance in order to measure the small current signals, any differential input bias current to the input terminals of the amplifier (input offset current) will result in a relatively large output differential offset voltage. Consequently, a JFET input buffer is used to buffer the inputs to the op-amp which has a low input bias current of approximately 130 pA and more importantly, a low input offset current of approximately 20 pA[36].

Consider, for instance, a feedback impedance of $1 \text{ M}\Omega$ which roughly corresponds to a differential transimpedance of $1 \text{ M}\Omega$. If the inputs to the fully-differential amplifier were left unbuffered, the typical input offset current taken from the data sheet for the THS4140 of $0.1\mu\text{A}$ would result in a differential output voltage offset of 100mV. With the inputs buffered with the JFET AD8620 amplifiers, the differential output voltage offset will be nominally, $20 \mu\text{V}$ [36].

Also, the connection between the measurement electrode and the input to the transimpedance amplifier is made with shielded coaxial cables. The shields are connected to ground so that the connection is shielded from electric interference. The coaxial shield capacitance to ground is a significant capacitance in the stray capacitance from the measurement electrodes to ground, i.e. $C_{p3,4}$ from Section 2.3, however, as will be shown in Chapter 4, these stray capacitances will not affect the closed-loop output response.

Finally, the THS4140 uses common-mode feedback so that the output common-mode voltage is constant. This voltage is set to 2.5V with a resistor divider so that the common-mode input voltage to the Analog-to-Digital Converter (ADC) will be centered between its 0-5 V supply voltage rails.

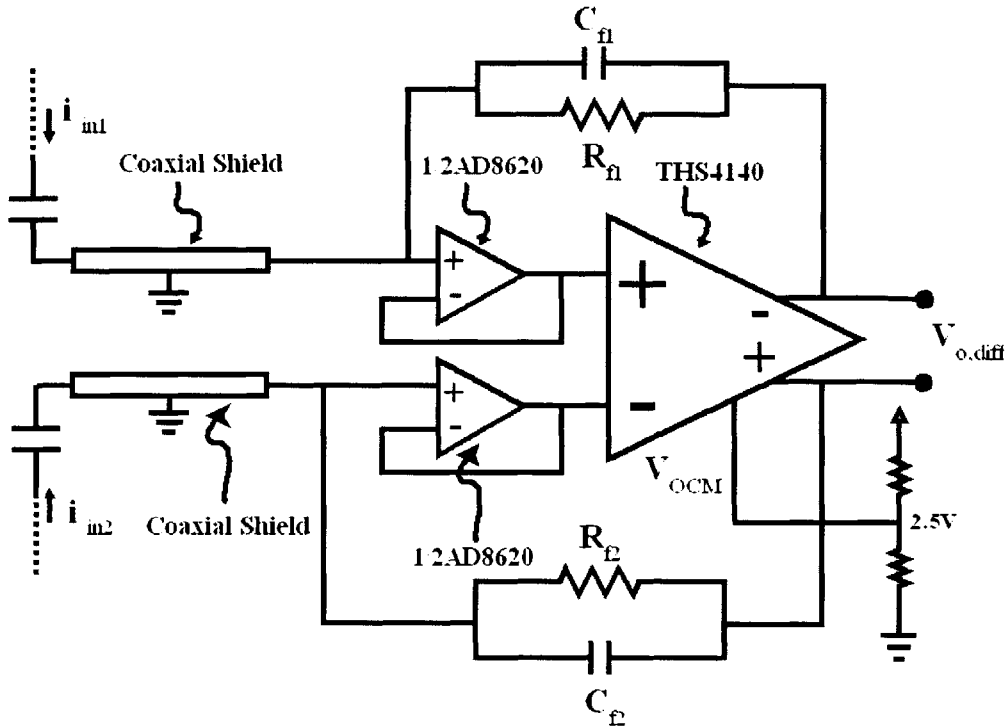


Figure 3-1: Schematic of the Low-Noise Analog Front-End Amplifier.

3.1.1 Differential Front-End Operating Principles

The lamp sensor electronics are implemented with a fully differential topology for the signal conditioning circuitry, meaning that the inputs and outputs of each stage are differential. One advantage of the fully differential topology is that it rejects common-mode interference. Interfacing the differential measurement with the balanced or symmetric capacitive bridge formed by the capacitances below the lamp has the advantage that the front-end amplifier can have very high gain without saturating its output. This is because in a balanced bridge, the no-detection case corresponds to zero differential output voltage. Then, the very high gain can be used to amplify small deviations in the electric flux measurements amidst large nominal or common-mode electric flux magnitudes. Figure 3-2 illustrates the general principle of detecting small signal deviations amidst large common-mode nominal signals with a differential measurement. Keeping in mind that in the figure,

$$V_{diff} = V_{left} - V_{right} \quad (3.1)$$

so that when

$$V_{left} = V_{right}, \quad (3.2)$$

$$V_{diff} = 0. \quad (3.3)$$

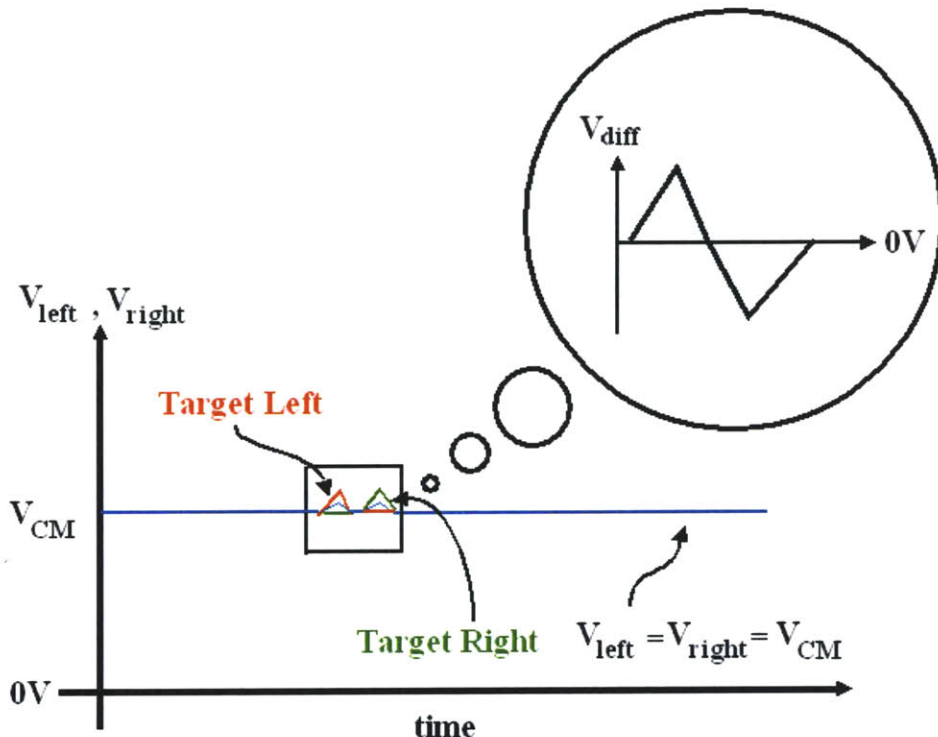


Figure 3-2: The concept of separating differential-mode signals from common-mode signals.

In addition to separating differential signals from common-mode signals, it is important to understand how the front-end amplifier measures current at the measurement electrodes. To see how the current-mode measurement takes place, it is argued that the differential-mode input voltage at the input terminals of the amplifier is essentially zero. This argument is similar to the argument for a more common single-ended op-amp in a negative feedback configuration like that shown in Figure 3-3.

Because the response of the op-amp to input voltages is

$$v_{out} = A(v_+ - v_-) \quad (3.4)$$

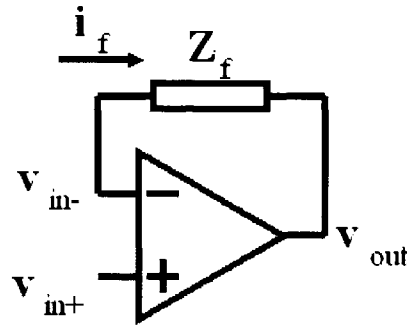


Figure 3-3: A typical op-amp negative feedback connection

and A is very large, any differential input voltage $v_+ - v_-$ results in a large output voltage v_{out} . If there is a positive differential input voltage, i.e.

$$v_+ > v_-, \quad (3.5)$$

the output voltage increases so that the inverting terminal voltage increases, thus decreasing the differential input voltage. If there is a negative differential input voltage the output voltage decreases so that the inverting terminal voltage decreases, thus decreasing the differential input voltage. The result is that the differential input voltage is always nearly 0V. In other words, the two input terminal voltages are nearly equal.

This reasoning can be extended to the fully differential amplifier, as in Figure 3-4 for which the open-loop gain is differential:

$$A_{v,d} \equiv \frac{v_{o,d}}{v_{in,d}}. \quad (3.6)$$

Now, a differential input voltage increases the differential output voltage. The negative feedback in the fully differential case is implemented so that the inverting output terminal feeds back to the non-inverting input terminal and the non-inverting output terminal feeds back to the inverting input terminal. Increasing the differential input voltage increases the differential output voltage and causes the input differential voltage to decrease. Therefore the differential input voltage is always nearly 0 V. In other words, the two input terminal voltages are nearly equal.

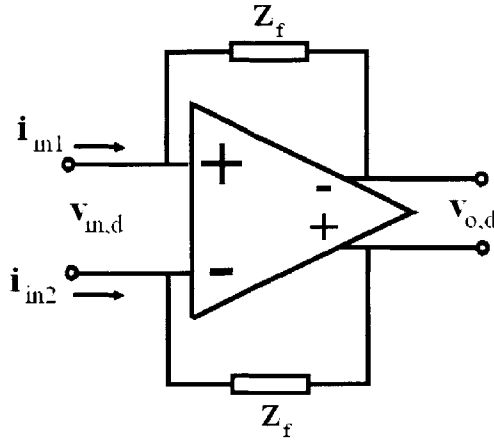


Figure 3-4: Differential input current in a differential amplifier

In the context of current-mode detection, the differential transimpedance amplifier draws a differential current at its input such that its input terminal voltages remain equal. For an ideal amplifier with infinite open-loop gain ($A \rightarrow \infty$), the differential amplifier has a differential transimpedance, Z_d equal to the impedance of the feedback impedance formed by the parallel combination of R_f and C_f ,

$$Z_d(s) = Z_f(s) = \frac{R_f}{R_f s C_f + 1}. \quad (3.7)$$

Therefore, in the negative feedback connection, the fully differential transimpedance amplifier in Figure 3-4 measures a differential input current $i_{in,d}$ and multiplies it by the differential transimpedance $Z_d(s)$ so that the output is

$$\boxed{v_{o,d} = i_{in,d} Z_d}, \quad (3.8)$$

where

$$i_{in,d} = i_{in1} - i_{in2}. \quad (3.9)$$

3.1.2 Differential Transimpedance Amplifier Input Characteristics

The impedances presented by the capacitances in the lumped element capacitance model of Chapter 2 are relatively large. A nominal value for the capacitance between the sig-

nal source and the measurement electrode in front of that source is 1 pF. With the ballast operating frequency of 42 kHz, the capacitive impedance is

$$|Z_c(j\omega)| = \frac{1}{\omega C} = 3.79 \text{ M}\Omega. \quad (3.10)$$

Nominal values of the capacitive impedance between the source and the target are generally even larger. For a capacitance of 10 fF, the impedance is 379 MΩ. The front-end amplifier should be able to accurately sense the small current signals in the capacitive circuit. There are two input characteristics of the front-end amplifier that make it appropriate for accurate current-mode measurement. First, very little current should be lost to the input terminals of the op-amp or any shunt impedance at the measurement nodes in the front-end amplifier. Second, the differential input impedance of the front-end amplifier should be very small.

To see that very little current is lost to the input terminals of the op-amp, consider the effect of the shunt impedance at the measurement node on the differential output voltage in Figure 3-5. In current-mode detection, the measurement electrode is connected directly to the input terminal of the high gain operational amplifier.

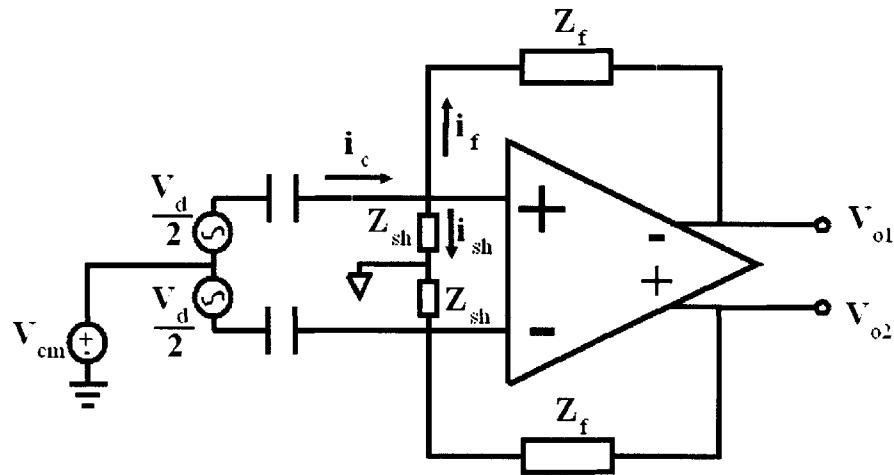


Figure 3-5: A fully differential amplifier taking into account shunt impedances from the measurement nodes to incremental ground.

The shunt impedance, Z_{sh} , represents both the op-amp input terminal impedance and any parasitic capacitive impedances at the measurement node. In order to see the effect of

the shunt impedance on the output voltage, the half-circuit shown in Figure 3-6 is considered.

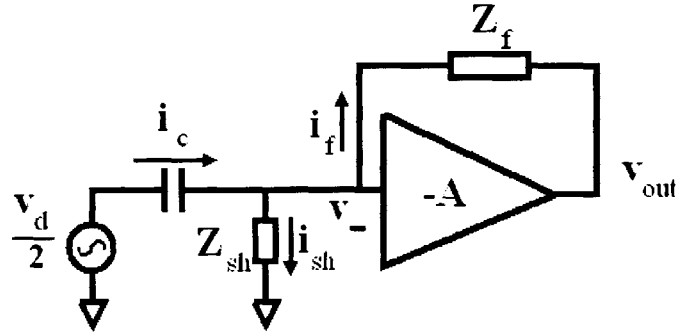


Figure 3-6: The half-circuit with incremental grounds for calculating the effect of the shunt impedance on the output voltage.

The output voltage of the amplifier is

$$v_{out} = -Av_- \quad (3.11)$$

and accounting for the current that flows into the input impedance of the op-amp yields

$$v_- = (i_c - i_f)Z_{in} \quad (3.12)$$

$$v_{out} = -A(i_c - i_f)Z_{sh} \quad (3.13)$$

$$v_- = i_f Z_f + v_{out} \quad (3.14)$$

Eliminating v_{out} and v_- ,

$$i_f Z_f = v_-(1 + A) \quad (3.15)$$

$$\frac{i_f Z_f}{1 + A} = Z_{sh}(i_c - i_f), \quad (3.16)$$

so that the ratio of the input current to the feedback current is

$$\frac{i_c}{i_f} = \frac{\frac{Z_f}{1+A} + Z_{sh}}{Z_{sh}}. \quad (3.17)$$

Finally, taking the limit of (3.17),

$$\lim_{A \rightarrow \infty} \left(\frac{i_c}{i_f} \right) = 1, \quad (3.18)$$

which implies that the effective shunt impedance at the input of the amplifier is

$$Z_{in,sh} = \infty, \quad (3.19)$$

so that

$$i_c \approx i_f. \quad (3.20)$$

Therefore, the effective input impedance of the op-amp terminals $Z_{in,sh}$ approaches ∞ as the gain A approaches ∞ . Rearranging the expression in (3.17) gives

$$\frac{i_c}{i_f} = \frac{Z_f + Z_{sh}(1 + A)}{Z_{sh}(1 + A)} \quad (3.21)$$

and comparing it to the relation between i_c and i_f in the simple current divider circuit in Figure 3-7,

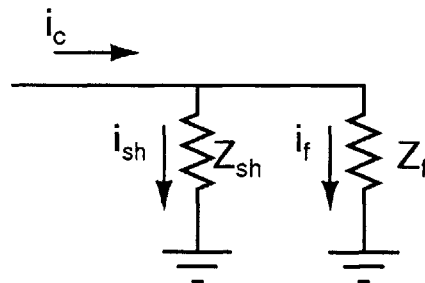


Figure 3-7: A current divider between the currents in the op-amp circuit with the op-amp removed.

$$\frac{i_c}{i_f} = \frac{Z_f + Z_{sh}}{Z_{sh}} \quad (3.22)$$

the shunt impedance Z_{sh} appears multiplied by the open-loop gain of the op-amp.

$Z_{sh} \rightarrow Z_{sh}(1 + A)$

(3.23)

Therefore, any differential shunt impedance from an input terminal of the op-amp to ground has the effect of a shunt impedance multiplied by the open-loop gain and can therefore generally be neglected. This argument, although commonplace for op-amp circuits, will be important in neglecting the effect of certain stray capacitances in Chapter 4. In particular, the stray capacitances from the electrodes and input terminals to incremental ground will appear as capacitive impedances in parallel with the input terminal impedance of the op-amp and will be multiplied by the open-loop gain.

Using real values for the input terminal impedance of the op-amp and the open-loop gain, the amount of current shunted away from the feedback stage as a result of the finite input terminal impedance can be calculated. The differential amplifier in the lamp sensor, the THS4140, has an open-loop gain of

$$A = 2200 \quad (3.24)$$

at the signal frequency of 42 kHz[38]. From the data sheet for the input JFET voltage buffer amplifier [36], the input impedance is the impedance due to the differential-mode input capacitance of 8pF,

$$C_{in} = 8 \text{ pF}. \quad (3.25)$$

The input and feedback impedance magnitudes for the operating frequency of the ballast are

$$|Z_{in}(j\omega)| = 474 \text{ k}\Omega \quad (3.26)$$

$$|Z_f(j\omega)| = 966 \text{ k}\Omega. \quad (3.27)$$

The input impedance value, $|Z_{in}(j\omega)|$, is taken to be fixed. In reality, it is changes in the effective input impedance as the capacitances change below the lamp that will be measured. However, the change in the input impedance will be very small compared to the nominal input impedance which is dominated by the fixed capacitance from the electrode to the bulbs.

The feedback impedance values will be discussed in Section 3.1.3. Finally, (3.17) gives

$$\frac{|i_{in}|}{|i_f|} = \frac{\left|\frac{Z_f}{1+A} + Z_{in}\right|}{|Z_{in}|} \quad (3.28)$$

$$= \frac{\frac{966 \text{ k}\Omega}{1+2200} + 474 \text{ k}\Omega}{474 \text{ k}\Omega} \quad (3.29)$$

$$\frac{|i_{in}|}{|i_f|} = 1.0009, \quad (3.30)$$

so that 0.09% of the input current is lost to the shunt impedance to ground at the input terminal of the amplifier in the worst case. As a matter of fact, the shunt impedance at the measurement node does not present a significant load to the input signal in the closed-loop configuration until it is smaller than the feedback impedance by a factor of the open-loop gain.

Although the op-amp terminal input impedance is very large, the differential-mode input impedance of the front-end amplifier is very small so that the amplifier is appropriate for measuring differential-mode currents. The differential-mode input impedance can be found again referring to Figure 3-5. The differential-mode input impedance is defined to be the amount that the differential input voltage increases for a differential input current.

$$Z_{in,d} \equiv \frac{v_{in,d}}{i_{in,d}} \quad (3.31)$$

Again accounting for the current into the input impedance of the amplifier results in the expressions in (3.11), (3.12), (3.13), and (3.14). Then, i_{in} in terms of v_- is

$$i_{in} = v_- \left(\frac{1}{Z_{in}} + \frac{1+A}{Z_f} \right). \quad (3.32)$$

Therefore, the differential-mode input impedance is

$$Z_{in,d} = \frac{v_-}{i_{in}} = \frac{Z_{in}Z_f}{Z_f + (1+A)Z_{in}}. \quad (3.33)$$

For a very large amplifier gain A , the differential-mode input impedance vanishes:

$$\lim_{A \rightarrow \infty} (Z_{in,d}) = \lim_{A \rightarrow \infty} \left(\frac{Z_{in} Z_f}{Z_f + (1 + A) Z_{in}} \right) = 0. \quad (3.34)$$

For the real amplifier the differential-mode input impedance is

$$|Z_{in,d}| = 438 \Omega, \quad (3.35)$$

which is very small compared to the impedances presented by the capacitive system at the input of the amplifier.

3.1.3 Feedback Compensation

The feedback capacitors $C_{f1,2}$ that appear in parallel with the feedback resistors compensate the amplifier so that it provides a stable output. The compensation of the transimpedance amplifier must be examined both for the closed-loop and open-loop frequency response. The closed-loop frequency response must be examined because a transimpedance amplifier measuring current through a capacitive impedance at its input exhibits a voltage gain from the voltage source to its output that increases indefinitely with frequency for the uncompensated system.

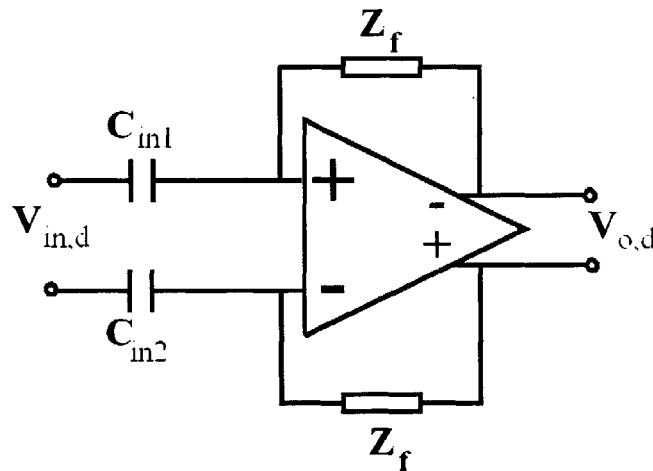


Figure 3-8: A differential transimpedance amplifier measuring current through capacitive impedances.

The differential voltage gain in Figure 3-8 is

$$A_{v,d} = \frac{Z_d}{Z_{in,d}} = \frac{Z_d}{\frac{1}{sC_{in,d}}}, \quad (3.36)$$

where

$$C_{in,d} = C_{in1} = C_{in2} \quad (3.37)$$

$$Z_d = Z_f. \quad (3.38)$$

For a fixed differential input capacitance the voltage gain increases with frequency without limit. This is the theoretical flaw with the differentiating amplifier. Although the voltage gain may be appropriate for the signal frequency of interest, the voltage gain for higher-frequency signals, such as input-referred thermal noise, is arbitrarily large. Therefore, an uncompensated differentiating amplifier will exhibit out-of-band sensitivities due to the extremely high gain for certain input signals be they random noise fluctuations or deterministic signals. Closed-loop bode plots for various compensations of the transimpedance amplifier using the THS4140 are shown in Figure 3-9. The input differential capacitance is taken to be 1 pF and the feedback resistance is 1 MΩ as it is for the actual front-end amplifier.

The top-most magnitude plot shows significant peaking in the uncompensated configuration, i.e. with no feedback capacitance. The voltage gain does not increase without limit but is limited by the GBW of the THS4140. However, the peaking in the gain is significant enough to create undesired output behavior. A datapoint near the ballast operating frequency of

$$f_{op} = 42 \text{ kHz} \quad (3.39)$$

is marked on the bode plots. We would like the gain at that frequency to be maximized while still limiting the high-frequency gain sufficiently enough so that the amplifier provides a predictable output voltage. Predictable output is obtained with the feedback capacitance value of 1 pF which is the depicted by the frequency response second to top-most in

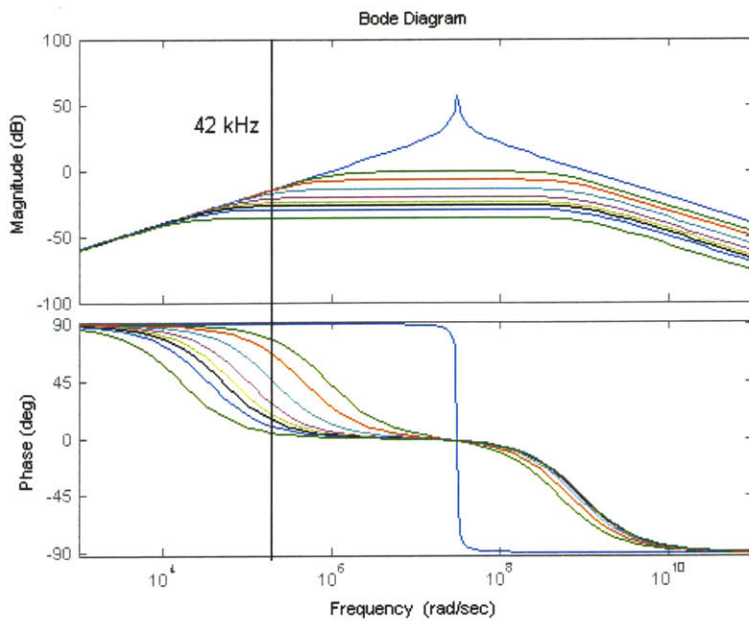


Figure 3-9: Closed-loop bode plots of the voltage transfer function of the Front-End amplifier with a fixed differential input capacitance. Plots are shown with various feedback capacitances $0 \leq C_f \leq 62 \text{ pF}$ and $R_f = 1 \text{ M}\Omega$.

Figure 3-9. Therefore, the feedback impedance is the parallel combination of

$$R_f = 1 \text{ M}\Omega, C_f = 1 \text{ pF}. \quad (3.40)$$

To see that the front-end amplifier is stable requires an examination of the open-loop transfer function. Figure 3-10 shows a half-circuit that can be used to evaluate the differential loop transfer function of the closed-loop system.

A feedback block diagram is used to model the dynamics. The input voltage v_- is amplified by the op-amp transfer function $-A(s)$. The output voltage is then attenuated and added back to the inverting input with the voltage divider formed by the feedback impedance and the parallel combination of C_{sh} and C_{in} . The block diagram is shown in Figure 3-11. In the block diagram

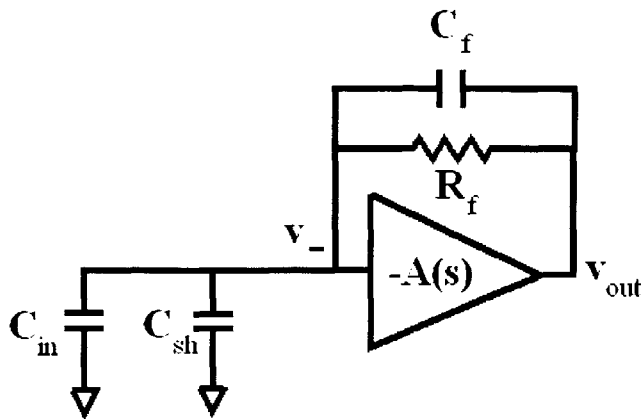


Figure 3-10: The half-circuit for calculating the stability of the differential front-end amplifier.

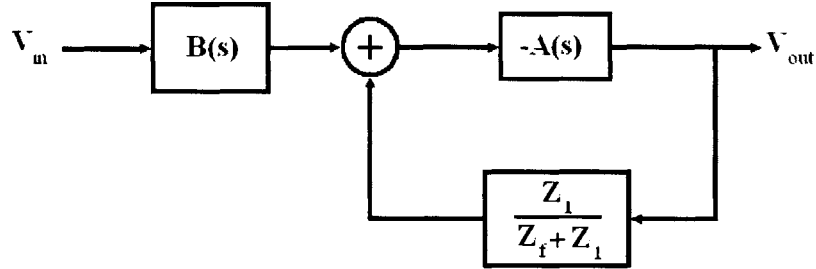


Figure 3-11: The block diagram for the differential closed-loop front-end amplifier system.

$$Z_{in} = \frac{1}{sC_{in}} \quad (3.41)$$

$$Z_f = \frac{R_f}{1 + R_f s C_f} \quad (3.42)$$

$$Z_{sh} = \frac{1}{sC_{sh}} \quad (3.43)$$

and

$$Z_1 = Z_{sh} \parallel Z_{in} \quad (3.44)$$

$$B(s) = \frac{Z_{sh} Z_{in}}{Z_f Z_{sh} + Z_f Z_{in} + Z_{sh} Z_{in}}. \quad (3.45)$$

The loop transfer function is

$$L(s) = A(s) \frac{Z_1}{Z_f + Z_1}. \quad (3.46)$$

From the datasheet for the THS4140, the single-pole approximation to the open-loop dynamical transfer function can be deduced. Using the gain-bandwidth product and open-loop gain of the amplifier, $A(s)$ is [38]

$$A(s) = \frac{2238.7}{1 + \frac{s}{2\pi \times 67 \text{ kHz}}}. \quad (3.47)$$

Therefore, $L(s)$ can be written as

$$L(s) = \boxed{\frac{2238.7}{1 + \frac{s}{2\pi \times 67 \text{ kHz}}} \cdot \frac{1 + R_f s C_f}{1 + R_f s (C_{in} + C_{sh} + C_f)}}. \quad (3.48)$$

The uncompensated loop transfer function, $L'(s)$, would have been

$$L'(s) = \frac{2238.7}{1 + \frac{s}{2\pi \times 67 \text{ kHz}}} \cdot \frac{1}{1 + R_f s (C_{in} + C_{sh})}. \quad (3.49)$$

The uncompensated bode plot ($C_f = 0 \text{ pF}$) is shown in Figure 3-12 for $R_f = 1 \text{ M}\Omega$. The uncompensated system shows a phase margin of only 6.5° which is not suitably stable. The instability in the uncompensated system arises because of the two poles from the op-amp frequency response and from the combination of input and shunt capacitances, C_{in} and C_{sh} with the feedback resistance, R_f . Because of the two-pole roll-off and the lack of a zero in the vicinity, the phase is allowed to approach -180° near cross-over. From (3.48) the feedback capacitance, C_f adds a zero in the loop-transfer function in the vicinity of at least one of the poles. This significantly reduces the phase error from the input to the output near cross-over thereby increasing the phase margin of the system. The addition of the parallel capacitance, C_f , in the feedback network is a form of lead compensation because it adds leading phase shift or positive phase to the output signal relative to the input signal[23].

A plot of the loop transfer function in MATLAB in Figure 3-13 shows the gain and phase margin of the closed loop system with the feedback elements from (3.40). The input capacitance is taken to be 1 pF because this is the nominal value of the total fixed capacitance from the electrode at the input of the amplifier to the fluorescent bulbs. Also, there is a stray input capacitance to ground at the input to the amplifier. This stray capacitance is dominated by the coaxial shield of the cable at the input to the amplifier but also includes

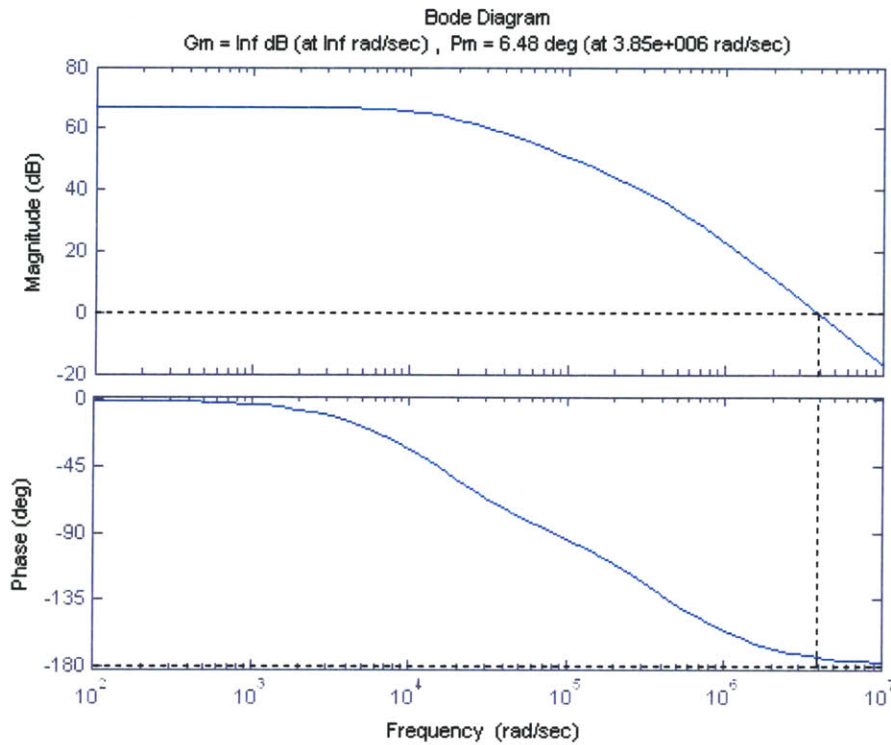


Figure 3-12: Bode plot of the loop transfer function for the uncompensated system ($C_f = 0$) showing poor phase margin.

stray capacitances from the electrodes and the amplifier inputs to any incremental ground. The shield capacitance is taken to be 31 pF based on the length of the cables typically connecting the input of the amplifier to the electrodes. The bode plot shows a phase margin of 88° which implies that the front-end amplifier will be stable.

Increasing the stray capacitance from the input to ground should decrease the phase margin or stability of the amplifier because it should increase the phase of the input relative to the output. In Figure 3-14, the stray input capacitance has been increased from 31 pF to 3.1 nF (two orders of magnitude). The phase margin of 67° is significantly reduced as expected. However, the system is still suitably stable so that we can be sure that no reasonable stray input capacitance will result in instability.

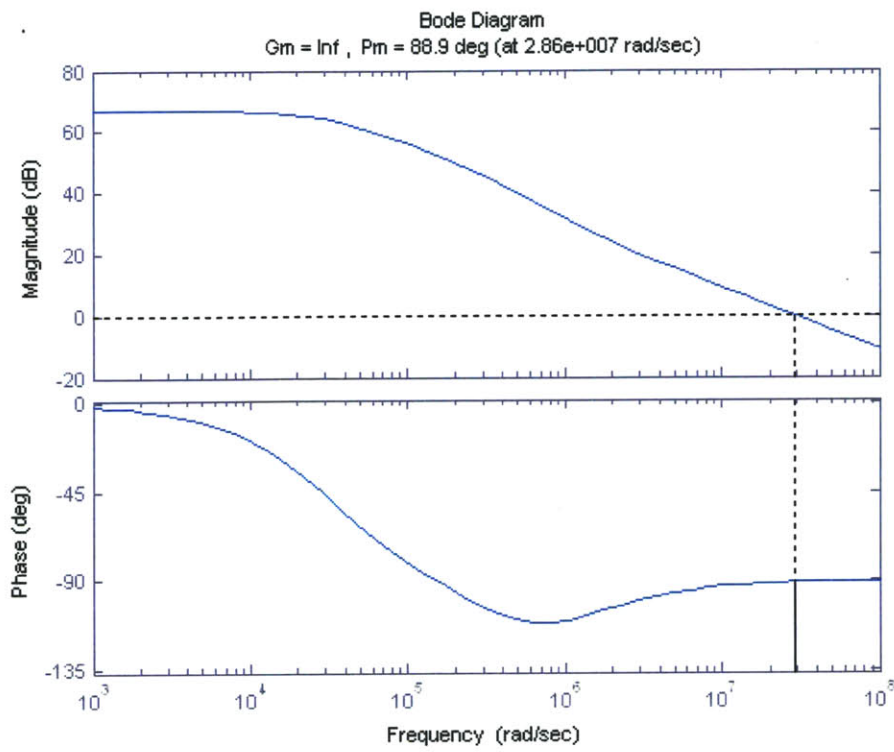


Figure 3-13: Bode plot of the compensated loop transfer function showing good phase margin. The addition of C_f in the feedback network is a form of lead compensation.

3.1.4 Common-Mode Rejection

Common-mode rejection is important for the lamp sensor electronics because common-mode modulations in the lamp source amplitude may be significant and are not well-controlled so they should be rejected at the differential output. The THS4140 was also chosen for its high common-mode rejection ratio (CMRR) of 84 dB. The CMRR specification is important in implementing the fully differential topology and exploiting the advantages that it presents. The higher the CMRR, the less that the differential output of the amplifier will respond to coupling or interference that is present equally on the input terminals.

It is important to understand what is meant by CMRR in the context of the fully-differential amplifier. What we are concerned with in the fully-differential topology is the ability to attenuate the effect of common-mode input signals on differential-mode output signals. The effect of common-mode input signals on common-mode output signals is less

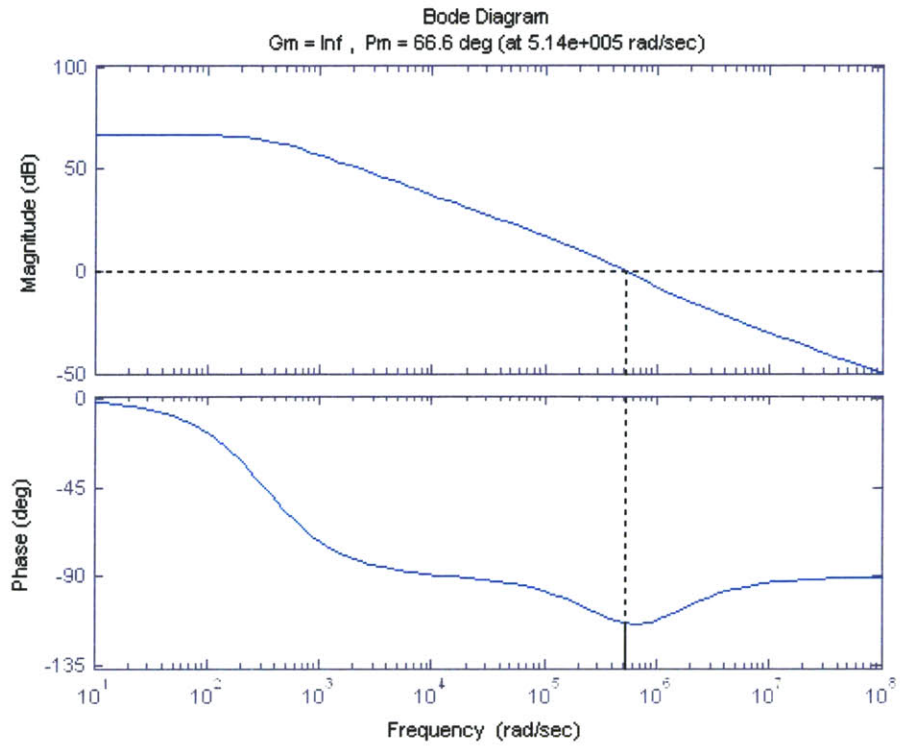


Figure 3-14: Bode plot of the compensated system with extra input capacitance showing degraded but acceptable phase margin.

important because the fully-differential topology is maintained all the way to the input of the ADC and the CMRR of the ADC is 120 dB[42]. Therefore, any common-mode gain, as long as it is small, is of no concern because common-mode signals remain separated from differential-mode signals throughout the signal processing electronics.

Figure 3-15 shows a simplified schematic of the THS4140. The front-end of the part is a fully-differential amplifier itself. The current source that supplies the constant current which is divided between the two legs of the differential amplifier is an important factor in determining the CMRR. The extent to which that current stays constant or the extent to which the current source's output impedance is infinitely large, is in part the extent to which the differential front-end rejects common-mode signals. If a common-mode signal is present on the input terminals, for that signal to appear at the output as a differential-mode signal, the currents in the two legs of the differential amplifier must both change together yielding a net change in the current through the current source. That being said, for the net change in tail current through the current source to cause a differential output

voltage change as opposed to a common-mode output voltage change, there must also be mismatches in the devices internal to the fully-differential op-amp. Therefore, the CMRR of the op-amp itself is mainly a function of the output impedance of the tail current source in the front-end amplifier stage, and the matching of the devices throughout the amplifier. In the case of the THS4140, the CMRR of 84 dB is relatively high. A common-mode input signal and a differential-mode input signal with the same magnitude will be appear at the output with the differential-mode signal being amplified more than four orders of magnitude more than the common-mode signal.

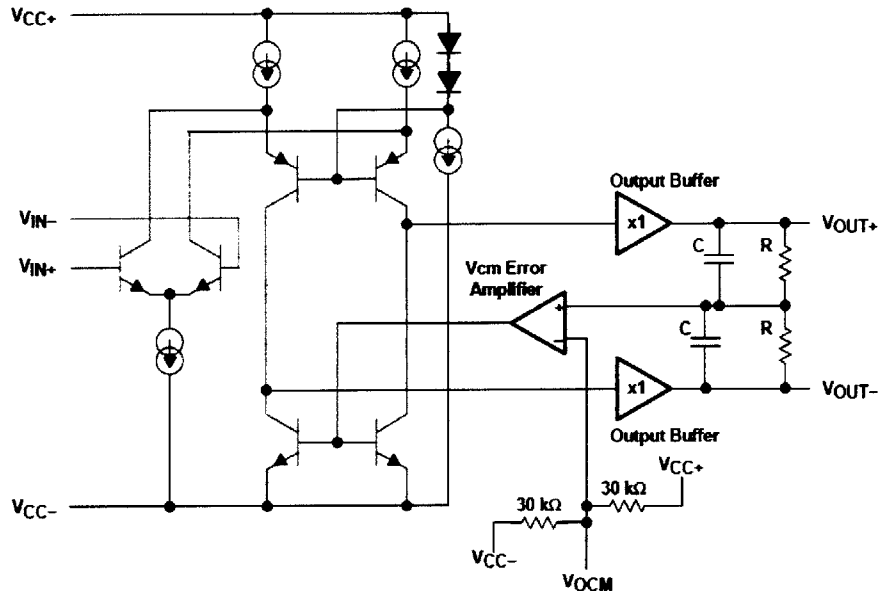


Figure 3-15: Simplified schematic of THS4140[38].

It is also important to consider how common-mode rejection is affected by the matching of the external circuit elements. In general, the CMRR is the ratio of the differential-mode gain to the common-mode gain^[7].¹²

$$\text{CMRR} \equiv \frac{|A_d|}{|A_c|} \quad (3.50)$$

¹CMRR is alternatively defined as the reciprocal of the definition here, but this work defines CMRR as the ratio of the differential to common-mode gain and cites Chong-gun Yu and the THS4140 datasheet as references[7][38].

²CMRR values are typically expressed in dB but the logarithm may be left out for simplicity in calculations and Chong-gun Yu is cited as a reference [7].

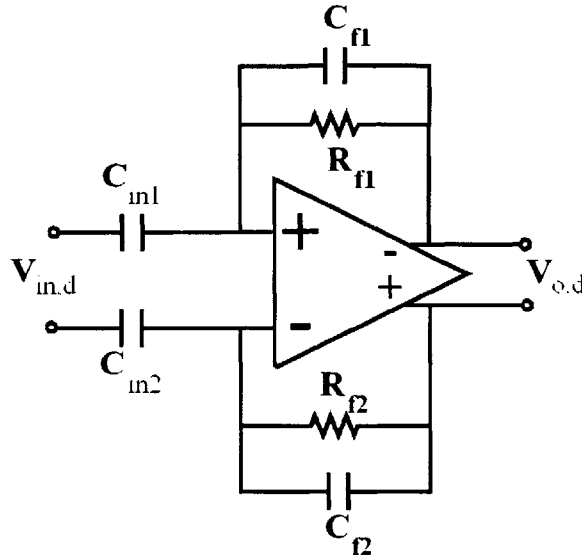


Figure 3-16: The differential amplifier with component mismatches.

Referring to Figure 3-16, the CMRR in terms of the matching of the external circuit elements is described by the differential-mode and common-mode gains:

$$A_d = \frac{Z_f}{Z_{in}} \quad (3.51)$$

$$A_c = \frac{Z_{f1}}{Z_{in1}} - \frac{Z_{f2}}{Z_{in2}}, \quad (3.52)$$

so that

$$\text{CMRR}_{ext} = \frac{\left| \frac{Z_f}{Z_{in}} \right|}{\left| \frac{Z_{f1}}{Z_{in1}} - \frac{Z_{f2}}{Z_{in2}} \right|}. \quad (3.53)$$

In (3.50), A_d is fixed and for small mismatches, the reciprocal of the CMRR can be written in terms of the sum of common-mode gains due to each mismatch while holding the other mismatches to zero:

$$\frac{1}{\text{CMRR}} \approx \frac{1}{|A_d|} (|A_{c1}| + |A_{c2}| + |A_{c3}| + \dots). \quad (3.54)$$

The individual common-mode gains are the sensitivities and they can be written as functions of mismatches in the external components so that the sensitivity due to each

mismatch is separated in the sum as is the CMRR of the op-amp, CMRR_{amp} :

$$\frac{1}{\text{CMRR}} \approx \frac{1}{|A_d|} (|f(\delta_{R_f})| + |f(\delta_{C_f})| + |f(\delta_{C_{in}})|) + \frac{1}{\text{CMRR}_{amp}}, \quad (3.55)$$

in which the sensitivity functions are evaluated with the other δ terms set to zero, for instance,

$$f(\delta_{R_f}) = f(\delta_{R_f})|_{\delta_{C_f}, \delta_{C_{in}}=0}. \quad (3.56)$$

The sensitivities are found as follows.

$$f(\delta_{R_f}) = \frac{Z_{f1} - Z_{f2}}{Z_{in}} = sC_{in} \left(\frac{R_f}{R_f s C_f + 1} - \frac{R_f + \delta_{R_f}}{(R_f + \delta_{R_f}) s C_f + 1} \right) \quad (3.57)$$

$$f(\delta_{C_f}) = sC_{in} \left(\frac{R_f}{R_f s C_f + 1} - \frac{R_f}{R_f s (C_f + \delta_{C_f}) + 1} \right) \quad (3.58)$$

$$f(\delta_{C_{in}}) = \frac{Z_f}{Z_{in1} - Z_{in2}} = Z_f s \delta_{C_{in}}. \quad (3.59)$$

For small δ_{R_f} , the sensitivity to mismatches in the feedback resistances can be further approximated as

$$f(\delta_{R_f}) \approx sC_{in} \left(\frac{\delta_{R_f}}{R_f s C_f + 1} \right) \quad (3.60)$$

and the full mismatch sensitivity can be written

$$\frac{1}{\text{CMRR}} = \quad (3.61)$$

$$\frac{1}{|A_d|} \left(|sC_{in} \frac{\delta_{R_f}}{R_f s C_f + 1}| \right) \quad (3.62)$$

$$+ |sC_{in} \left(\frac{R_f}{R_f s C_f + 1} - \frac{R_f}{R_f s (C_f + \delta_{C_f}) + 1} \right)| \quad (3.63)$$

$$+ |Z_f s \delta_{C_{in}}| \quad (3.64)$$

$$+ \frac{1}{\text{CMRR}_{amp}}. \quad (3.65)$$

Remembering that the reciprocal CMRR or sensitivity is

$$\frac{1}{\text{CMRR}} = \frac{|A_c|}{|A_d|}, \quad (3.66)$$

the sensitivity to modulations in the common-mode input voltage increases as any of the mismatches, δ_{R_f} , δ_{C_f} , or $\delta_{C_{in}}$ increase and it also of course increases as the CMRR of the amplifier, CMRR_{amp} decreases. In general, the mismatch in C_{in} can be controlled because it is dominated by the capacitance from the bulbs to each electrode which can be physically manipulated. In order to match the input capacitances, the electrode position in front of the lamp must be well-controlled. For instance, to not degrade the CMRR of the front-end beyond the degradation due to the 0.1% tolerance of the feedback resistors, the position of the electrodes in front of the lamp must be matched to within 0.1%. For a general parallel plate capacitance,

$$C(x) = \frac{\epsilon A}{x} \quad (3.67)$$

where, ϵ is the permittivity of the material between the plates, A is the cross-sectional area of the plates and x is the separation between the plates.

The Taylor series approximation of changes in the capacitance to deviations in x is

$$C(x) \approx C(x_0) + \frac{d}{dx}C(x)|_{x=x_0}(x - x_0) \quad (3.68)$$

And the second term

$$\frac{d}{dx}C(x)|_{x=x_0}(x - x_0) = -\frac{\epsilon A}{x_0^2}(x - x_0) \approx \Delta C, \quad (3.69)$$

but

$$\Delta C < -10^{-3}C(x_0) = -10^{-3}\frac{\epsilon A}{x_0} \quad (3.70)$$

so, from (3.69) and (3.70),

$$x - x_0 = \Delta x < 0.1\%x_0, \quad (3.71)$$

so that 0.1% changes in the depth are closely approximated to correspond to 0.1% changes in capacitance. The electrode positions are nulled in practice, by adjusting the depth of one electrode in the absence of a detection while watching the differential output voltage of the lamp sensor approach 0 V.

3.2 Synchronous Detection Operating Principle and Implementation

The lamp sensor receiving circuitry uses a synchronous detection operating principle. In a synchronous detector, there is a high-frequency signal source or carrier, and there is a low-frequency signal or modulating signal that modulates the carrier. The detection is synchronous because the receiving circuitry uses a copy of the carrier signal to demodulate the up-modulated signal. In our system, the carrier signal is the high-frequency flux signal from the alternating voltage source. The modulating signal or baseband signal is the low-frequency changes in the capacitive coupling caused by the movement of the target below the lamp.

3.2.1 Synchronous Detection Operating Principle

There are two principle advantages to using a synchronous detection scheme. First, the receiving circuitry only measures modulations in the carrier signal and not modulations in any other signals. This is true as long as no other signals present at the receiver have a phase and frequency close to the carrier signal. The fact that the synchronous detector is sensitive only to a specific carrier signal makes the system insensitive to ambient interference. The ability to isolate the lamp sensor's own signal is very important for this application because of the uncontrolled environment below the lamp along with signals from other fluorescent lamps.

The second advantage has to do with noise in the op-amp in the front-end amplifier. Figure 3-17 shows a basic plot of the noise densities for the two main types of noise in circuits, thermal noise and $1/f$ noise. Below a certain frequency range, the $1/f$ noise dominates and can be very significant because it increases with decreasing frequency. Above that frequency range, thermal noise dominates and is generally less significant than $1/f$ noise. The transition from one regime to the other is marked as the $1/f$ corner in the plot.

The $1/f$ corners for the two amplifier parts in the front-end amplifier, the THS4140, and the AD8620 are depicted in the plots of Figure 3-18. From the plots, the $1/f$ corner occurs

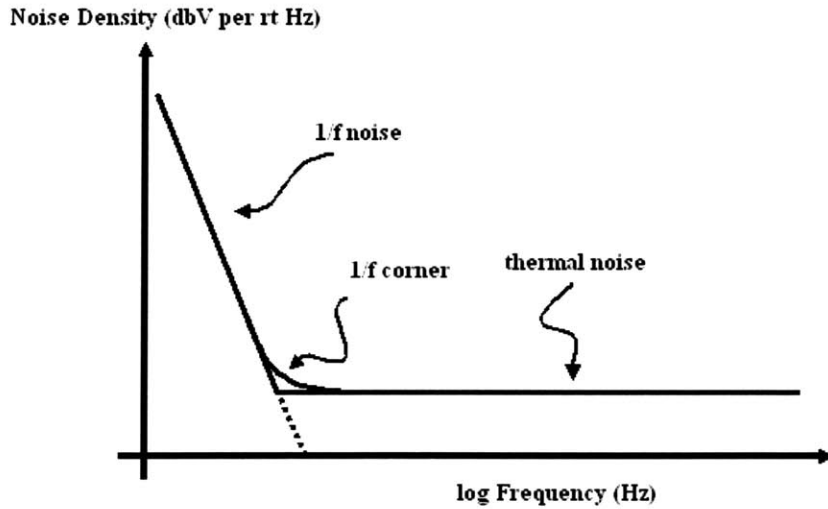


Figure 3-17: Basic plot of 1/f noise and thermal noise densities.

at about 2 kHz for each part.

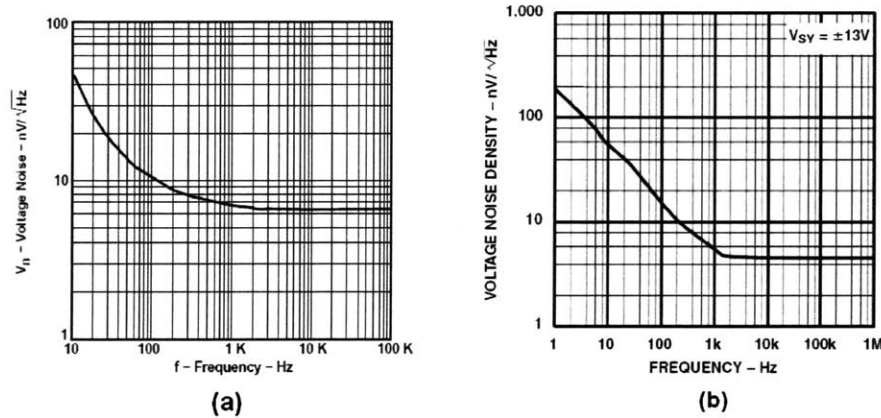


Figure 3-18: Plots of the voltage noise spectral densities for the THS4140 (a) and AD8620 (b)[38][36].

The effect of modulating the carrier signal by the low-frequency signal is that the front-end amplifier noise in the frequency range of the signal is dominated by thermal rather than 1/f noise. In Figure 3-20, the carrier signal frequency is in a frequency range in which the two parts in the front-end amplifier contribute mostly thermal noise and very little 1/f noise. However, the modulating signal is in a frequency range in which the signal may be overwhelmed by the 1/f noise contributed by the front-end amplifier.

By modulating the carrier signal with the baseband signal, the up-modulated signal now spans a frequency range in which the front-end amplifier contributes only thermal noise.

In the synchronous demodulator, the signal will be demodulated back to the low-frequency band after the signal has been amplified, leaving out the $1/f$ noise contribution from the front-end amplifier.

The two advantages described above, isolating specific carrier signals and leaving out $1/f$ noise, are not fundamentally different if the $1/f$ noise is considered a stray signal that is to be excluded.

A block diagram of the synchronous detection system is shown in Figure 3-19. In the block diagram, labels are given to the various signals and these labels correspond to the frequency domain plots of the signals in the Figures 3-20, 3-21, and 3-22. The approach to the graphical technique used here is that multiplying two time-domain signals, $s(t)$ and $p(t)$ for modulation and for demodulation is represented by convolving the two Fourier transforms of the signals, $S(j\omega)$ and $P(j\omega)$, in the frequency domain [22]. If

$$r(t) = s(t) \times p(t), \quad (3.72)$$

then

$$R(j\omega) = \frac{1}{2\pi} [S(j\omega) \otimes P(j\omega)]. \quad (3.73)$$

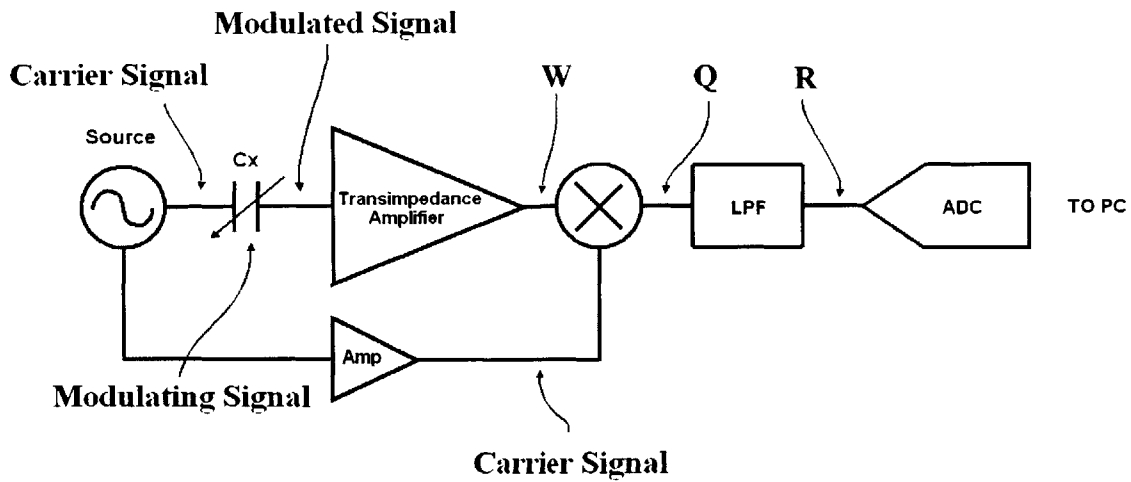


Figure 3-19: Block diagram of the synchronous detection system

In the synchronous detection system, the alternating flux from the voltage source is the carrier signal and changes in the measured capacitance C_x is the modulating signal.

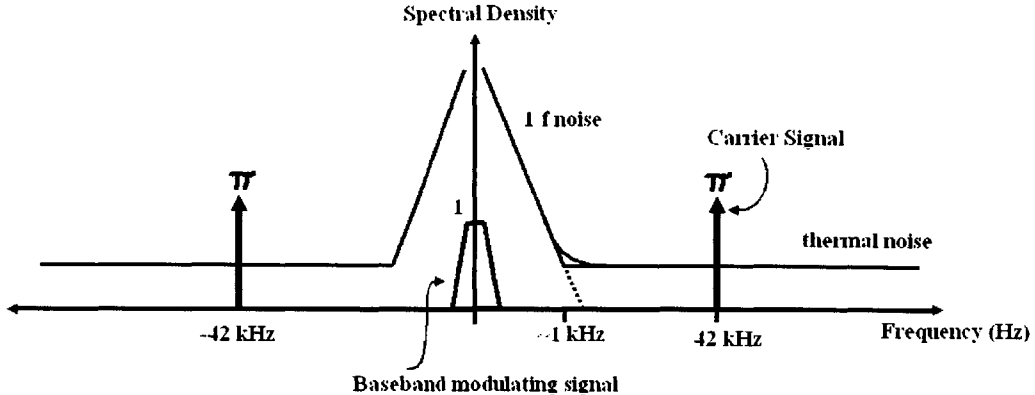


Figure 3-20: Frequency-domain plot of the modulating signal, carrier signal, and amplifier noise.

Figure 3-20 shows a frequency-domain plot of the modulating signal and the carrier signal superimposed on the front-end amplifier noise. By modulating the carrier signal with changes in C_x , the up-modulated signal spans a frequency range that is dominated by thermal and not 1/f noise. The output of the amplifier is labeled W and is shown multiplied by the carrier signal in Figure 3-21. The output of the multiplier is labeled Q and is shown as the result in Figure 3-21. Now, the baseband signal has been demodulated and 1/f noise from the amplifier is negligible in the low-frequency regime. This detection scheme is similar to chopper stabilization of op-amps. In chopper stabilization, the low-frequency signal to be amplified is first up-modulated to a high-frequency regime, then amplified as an up-modulated signal and finally demodulated back to the baseband following the amplifier stage[8].

Finally, the output of the low-pass filter is labeled R and is shown in Figure 3-22. What is left is the modulating signal and thermal noise that was originally surrounding the carrier signal. The relative magnitudes of the demodulated baseband signal and the thermal noise in Figure 3-22 are simply a result of the magnitudes assigned to the carrier signal (π in each case) in the previous development. The actual relative magnitudes of the two signals at the output of the synchronous detector depend on the magnitudes of the carrier signal at the input of the system and the carrier signal input to the multiplier as will be discussed in Section 3.2.2.

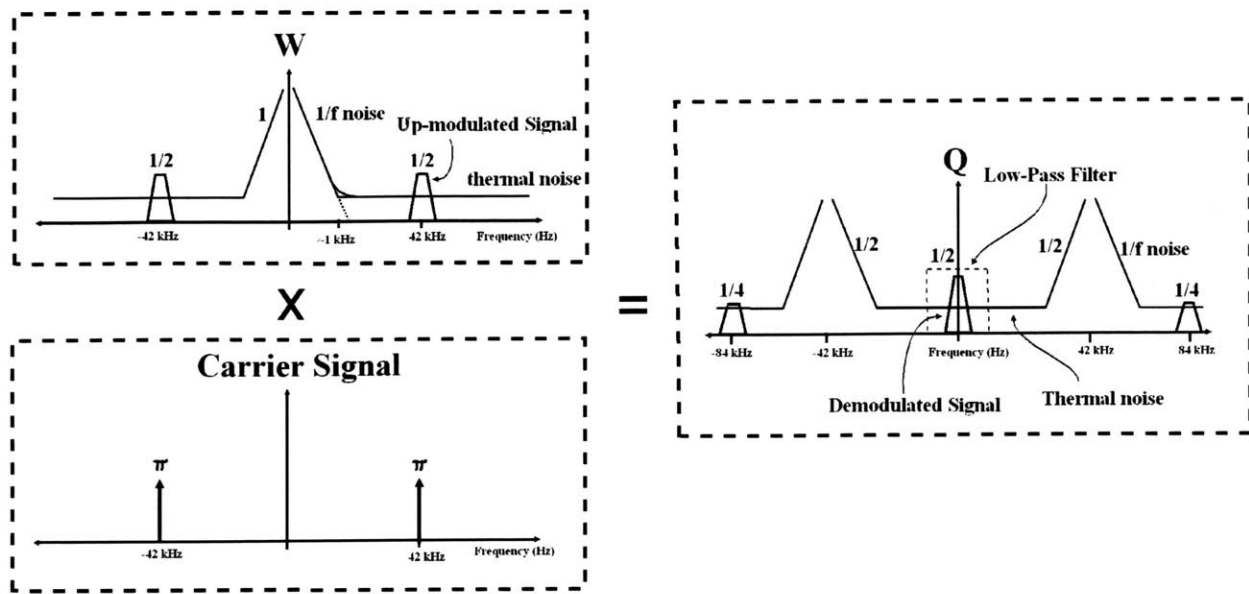


Figure 3-21: Demodulation of the amplified up-modulated signal by multiplication with the carrier.

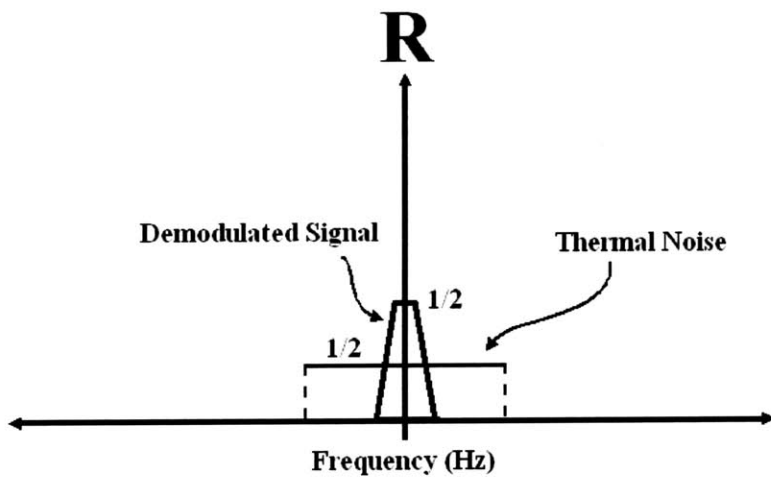


Figure 3-22: Output of the synchronous detection system.

The synchronous detector is a phase and frequency sensitive detector. It is a frequency sensitive detector, because stray high-frequency signals are demodulated back to the baseband sub-optimally and are filtered by the LPF. The narrower the bandwidth of the LPF, the less sensitive the synchronous detector is to stray high-frequency signals.

The synchronous detector is a phase sensitive detector because of the following. Multiplying a carrier frequency signal by the clock signal with some phase error between the

two, ϕ_{err} , results in

$$V_{out} = \cos(\omega_c t) \cos(\omega_c t + \phi_{err}) \quad (3.74)$$

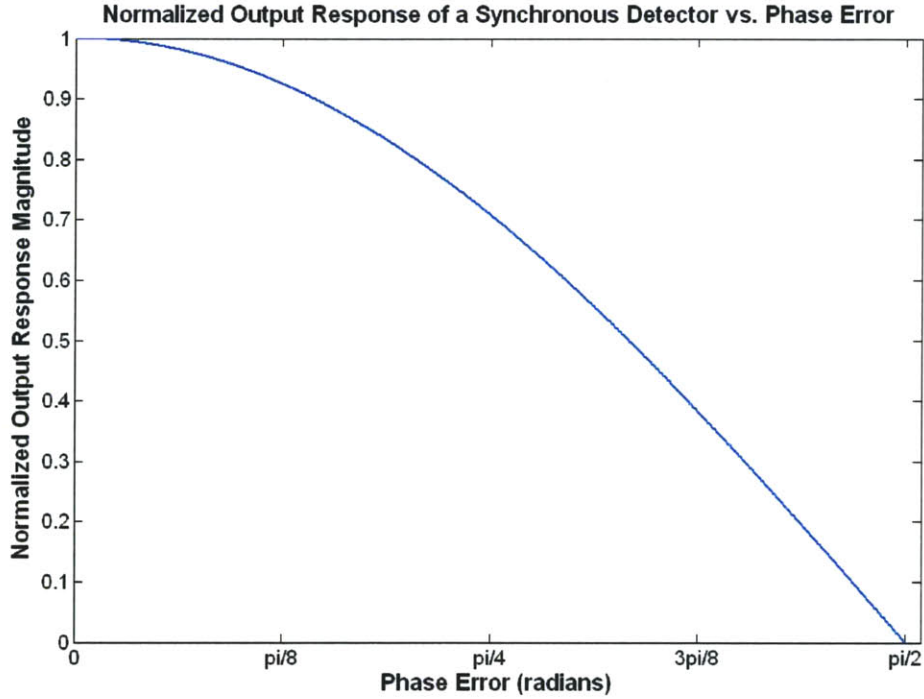


Figure 3-23: Normalized output response of the synchronous detector plotted against phase error between the measured signal and the clock signal.

Plotting this output response as a function of the phase error we see that the output response decreases with phase error until it vanishes for $\phi_{err} = \frac{\pi}{2}$ as shown in Figure 3-23.

3.2.2 Synchronous Detection Implementation

The actual implementation of the synchronous detection system begins with the analog front-end amplifier shown in Figure 3-1. The other pieces of the synchronous detection system include the clock generation circuit, the multiplier, and the low-pass filter (LPF).

In order to generate the clock or synchronous signal for demodulation, an in-phase measurement of the alternating voltage source is taken from the lamp. A small electrode is placed against one of the bulbs and the signal is detected with a transimpedance amplifier. The transimpedance amplifier is shown in Figure 3-24.

Two square wave clock signals are generated by the clock generation circuit. These

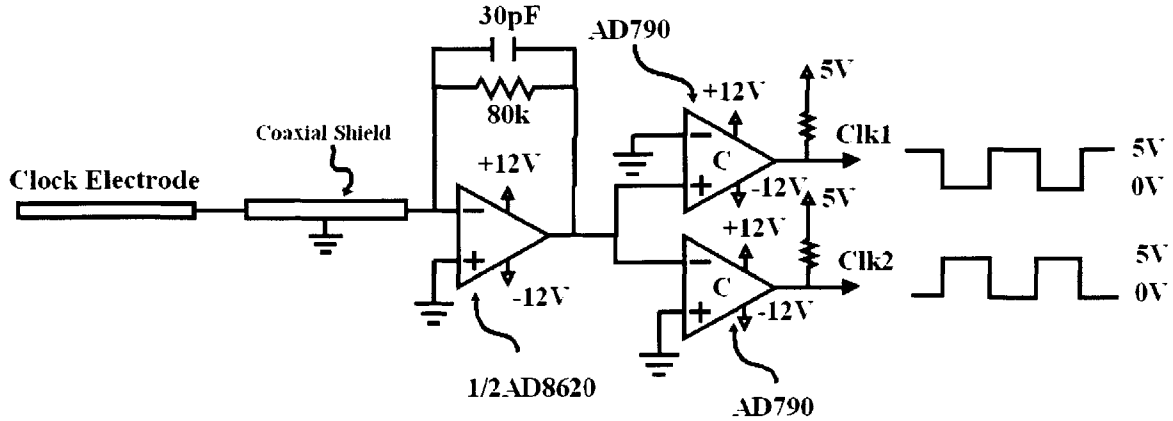


Figure 3-24: Clock generation circuit[39].

will be used to control the multiplier block. Again, a transimpedance amplifier is used to amplify the clock signal in part so that the clock signal and measured signal exhibit identical phase shifts from the bulb surface potential. This amplifier also needed to be compensated much like the front-end amplifier. The compensation of this amplifier need not be optimal. It only needs to provide a stable output that does not saturate the output stage of the op-amp and that is large enough to generate a clean signal for the input to the comparators. A feedback network consisting of the following values provides a stable output with a 2V_{pp} output.

$$R_f = 80 \text{ k}\Omega, C_f = 30 \text{ pF} \quad (3.75)$$

The transimpedance amplifier in this case is single-ended, meaning that the output is not differential as it was in the front-end amplifier. The output of the clock amplifier is centered on 0 V and is connected to the inputs of two comparators. Because the output of the clock amplifier is connected to the non-inverting input of one comparator and to the inverting input of the other comparator and because the other input terminals of the comparators are connected to 0 V, the outputs of the two comparators are 50% duty cycle square waves inverted of each other. The pull-up resistors on the open-collector outputs of the comparators are connected to 5 V and the ground references (not shown) for the comparators result in two TTL square waves at the outputs. These square waves are the two opposite switching control signals for the multiplier. The multiplier is implemented as a full-bridge switch multiplier for square-wave multiplication. It is a full-bridge switch multiplier so that the

fully differential topology is preserved from the input to the output of the multiplier. The multiplier circuit is shown in Figure 3-25.

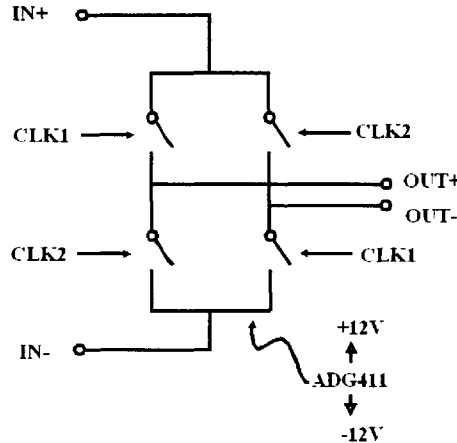


Figure 3-25: Fully differential square wave multiplier[41].

The time-domain square wave, $sq(t)$, can be written as the infinite sum of its Fourier series terms,

$$sq(t) = \frac{4}{\pi} \sum_{n=1,3,5,\dots}^{\infty} \frac{1}{n} \sin(\omega_n t), \quad (3.76)$$

where

$$\omega_n = n \times \omega_1 \quad (3.77)$$

and ω_1 is the fundamental frequency of the square wave in rps.

Demodulation using square-wave multiplication results in a demodulated signal, $d(t)$, consisting of the sum of the odd harmonics of the up-modulated signal, $s(t)$ having frequency components with magnitudes S_n for each frequency component n , each multiplied by the corresponding term in the fourier series of the square wave (assuming no phase error),

$$d(t) = \frac{4}{\pi} \sum_{n=1,3,5,\dots}^{\infty} [\frac{1}{n} \sin(\omega_n t) \times S_n \sin(\omega_n t)]. \quad (3.78)$$

The frequency-domain illustration of demodulation was shown previously. Examining the time-domain sum expression of the demodulated signal, $d(t)$ in (3.78), the dc compo-

nent of the demodulated signal can be recovered because

$$\frac{4}{\pi} \frac{1}{n} \sin(\omega_n t) \times S_n \sin(\omega_n t) = \frac{4}{\pi n} \times S_n \times [\frac{1}{2} - \frac{1}{2} \cos(2\omega_n t)] \quad (3.79)$$

$$d(t) = \frac{4}{\pi} \sum_{n=1,3,5...}^{\infty} \frac{1}{n} S_n [\frac{1}{2} - \frac{1}{2} \cos(2\omega_n t)] \quad (3.80)$$

so the multiplication results in a zero-frequency or dc component and frequency components with frequencies that are twice each of the odd harmonic frequencies. The demodulated signal is low-pass filtered in order to reject the non-dc components so that the baseband signal at the output of the LPF, $f(t)$, is (ignoring the attenuated high-frequency components)

$$f(t) = \frac{4}{\pi} \sum_{n=1,3,5...}^{\infty} \frac{1}{2n} S_n. \quad (3.81)$$

Therefore, demodulation implemented with a square wave multiplier results in a baseband signal consisting of a sum of the odd-harmonic magnitudes in the up-modulated signal each multiplied by the scaling factor $\frac{2}{\pi n}$.

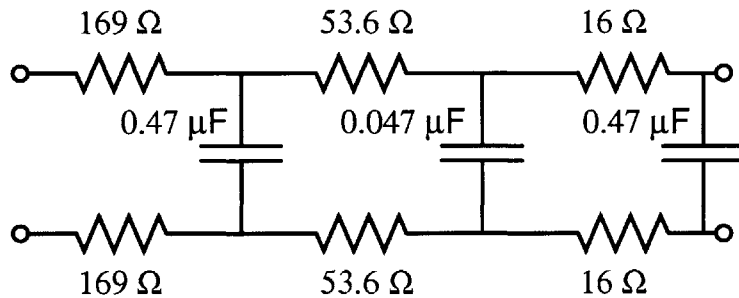


Figure 3-26: Fully differential LPF

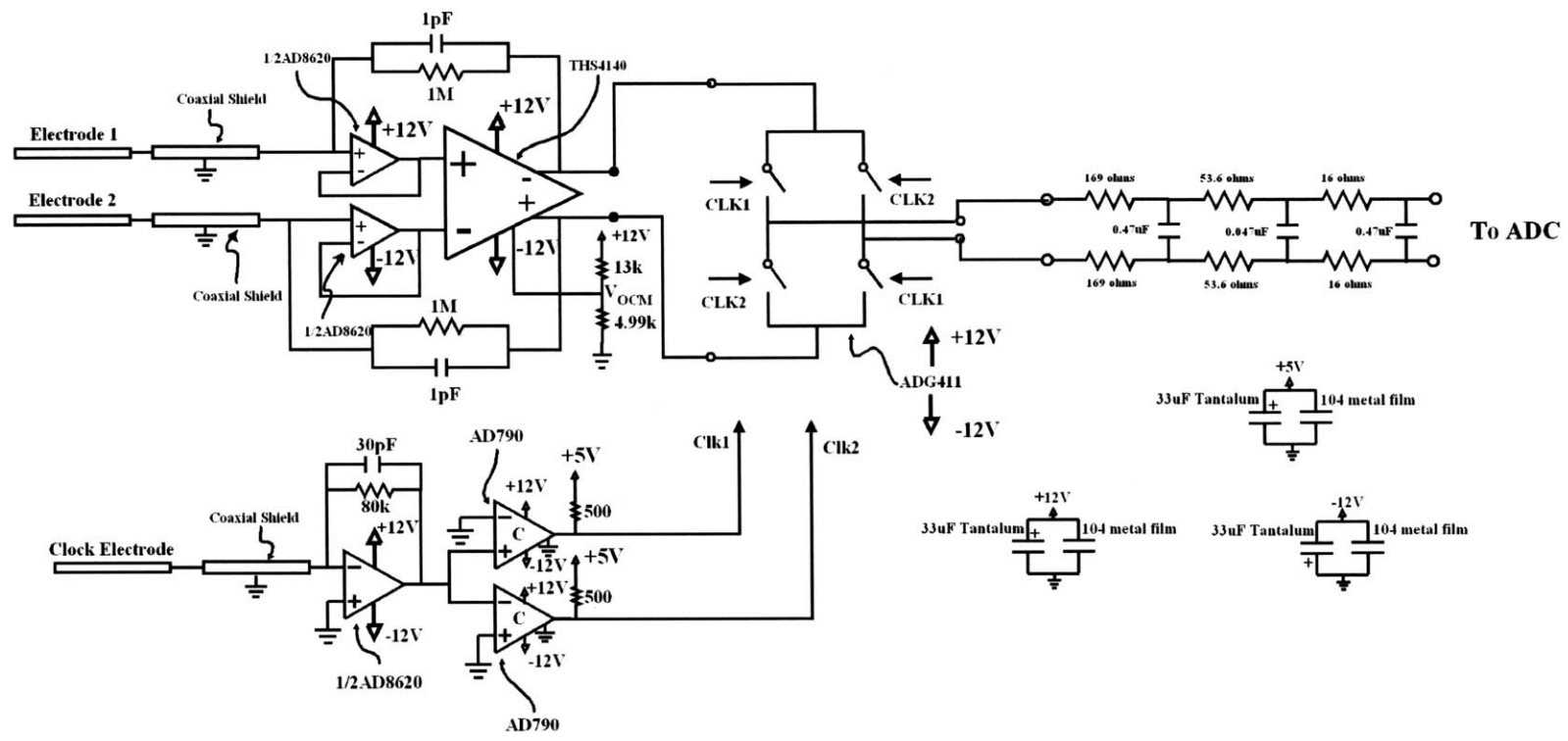
Finally, the LPF is implemented as a fully differential passive 3-pole RC ladder. The LPF need only band-limit the signal enough in order to sufficiently diminish aliasing in the analog-to-digital converter (ADC). This is important because it determines the frequency-sensitivity of the synchronous detection system as described previously. Stray out-of-band signals such as signals that appear at the measurement electrodes with frequencies near that of the carrier signal will be aliased into the output of the ADC and appear at the output of

the ADC. These signals are not wanted because the effect of modulating these signals with the target below the lamp cannot be predicted in general.

The LTC2440 is a sigma-delta ADC with an over-sampling ratio at the input that simplifies the anti-aliasing filter requirements[42]. The actual sampling rate at the input is a constant that is independent of the output sample rate. Therefore, the over-sampling ratio decreases as the output sample rate increases. The ratio of the over-sampling ratio to the output sample rate (or the actual sampling rate) is such that the Nyquist criterion gives a maximum input bandwidth of 54 kHz in order to prevent aliasing. As long as the input signal to the ADC is bandlimited to prevent aliasing, the ADC can be left to further properly bandlimit the signal with respect to the output sampling rate. The bandwidth of the LPF is approximately 800 Hz. It is a 3-pole passive RC filter and the attenuation is 20 dB per decade beyond 800 Hz but steepens so that it is 60 dB for each decade in frequency beyond 10 kHz.

The full topology of the analog receiving network is shown in Figure 3-27.

Figure 3-27: The full schematic of the analog receiving network.



3.3 Analog to Digital Interface

The full connection diagram for the analog-to-digital interface is shown in Figure 3-28. The analog differential output voltage from the analog stage of the receiver is connected to the analog differential input to the analog-to-digital converter (ADC). The ADC in the circuit is the Linear Technology part LT2440 which is accurate to 21-bits at its lowest sampling rate[42]. The ADC samples the input at a rate determined by a data byte transmitted from the PIC16F876 (PIC) [43] every sample interval. When the ADC has finished converting a data sample it pulls its Busy pin low (0 V). When that happens, the PIC outputs a serial data clock signal on pin RC3/SCK that shifts the four byte long data sample into its SDI register. When the entire data sample has been shifted out of the ADC's SDO register, it begins another conversion and the Busy pin goes high (5 V). The PIC then converts the data sample to a four character long ASCII string that represents the sign and value of the data sample. This string is then transmitted to the serial port of a PC using the RS-232 protocol and buffered with a MAX232 serial driver[44]. An 11.0592 MHz oscillator is connected to the CLKin pin on the PIC for accurate RS-232 transmission rates. In this case, the data rate of 115.2 kBPS is used for serial data transmission. The serial data rate is fast compared to any sample rate that will be achievable by the ADC so that the PIC output is never the limiting factor in the allowable data rate.

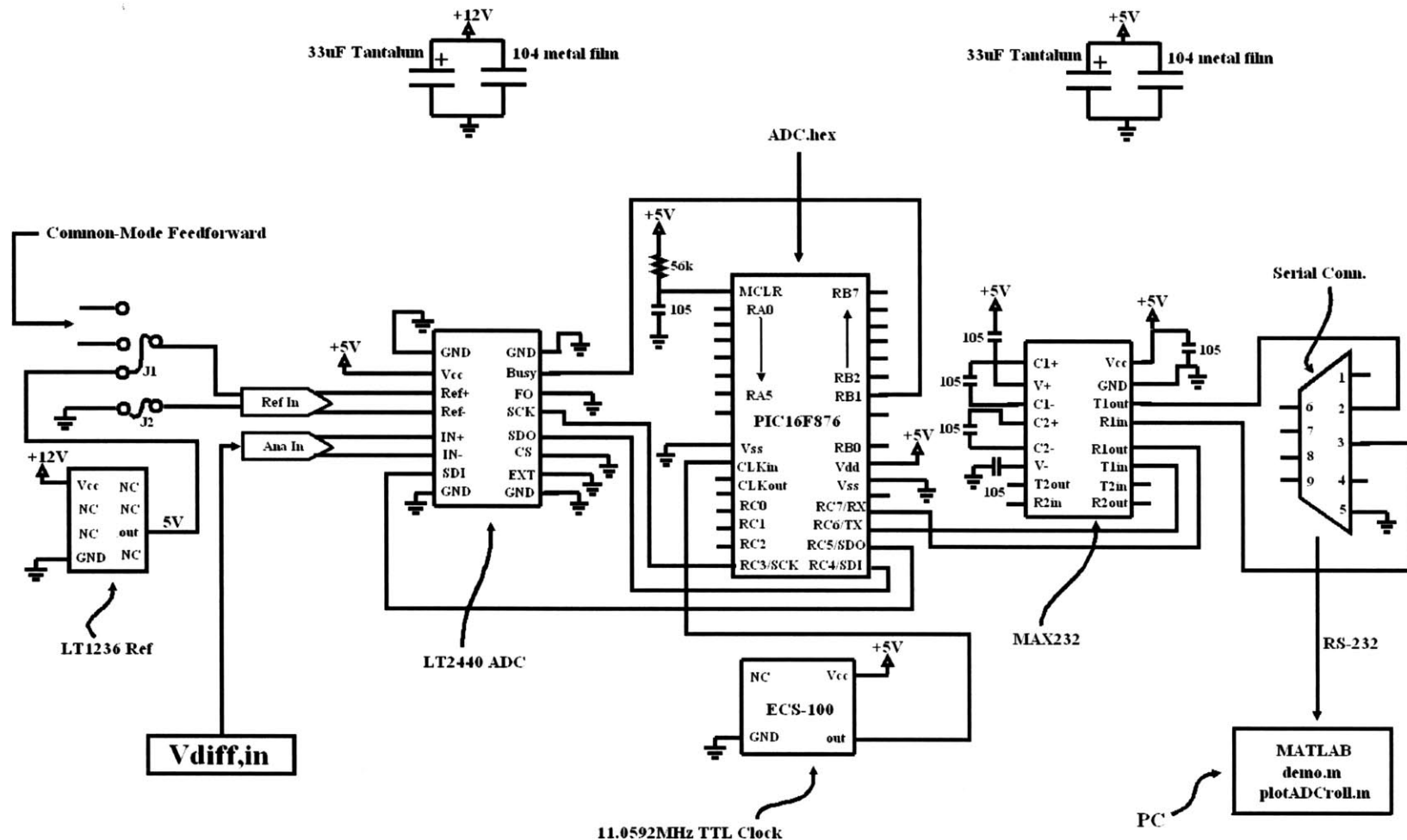
On the PC, MATLAB script were written to read the serial data from the serial port. Those scripts can be found in Appendix B. Nominal data rates for the ADC are 7 samples per second (sps), 14 sps, and 28 sps. The effective total output noise from the ADC itself increases as the sampling rate increases. Therefore, the slowest useable data rate is used, which for our initial application was 13.7 sps. The effective output bandwidth of the ADC for this sampling rate is 6.6 Hz. To verify that this is a useful bandwidth consider a person running below the lamp at 4 m/s which is a quick running pace. If the electrodes are spaced 40 inches apart, the time that it takes the target to pass from one electrode to the next is 0.25 s. An output voltage waveform depicting the target running below the lamp would have a frequency of roughly 4 Hz which is reasonable for the bandwidth of 6.6 Hz.

The ADC needs a reference voltage so that its output data sample is normalized and

can always span the full binary range from $0 \rightarrow 2^{21}$. The voltage reference value must be known to the user so that he can input that value on the PC in order to get absolute voltage values from the ADC. The PCB that was built for the prototype lamp sensor gives the user two choices for the voltage reference by way of jumpers J1 and J2.

The first choice is a 5V precision reference IC. The part that was chosen is the Linear Technology part LT1236 [40]. This part was chosen for its nominal output voltage and for its very low total output voltage noise. The second choice for the voltage reference is labeled “common-mode feedforward”. This is the output of another analog receiving network identical to that in Figure 3-27. The difference is that this receiving network takes a single-ended common-mode measurement of the alternating electric flux magnitude which is unaffected by the target. This is accomplished by placing an electrode directly on the surface of the bulbs, and spanning the two bulbs. The common-mode feedforward may be useful for normalizing the output response by low-frequency common-mode variations in the source voltage magnitude so that the output response to a fixed target does not change over time. In Chapter 6 about further work, the potential to use differential-mode feed-forward to cancel differential-mode noise from the source will be discussed. As will be evident in Section 3.4, a successful implementation of differential-mode feedforward normalization could potentially improve the already useable detection range and resolution of the lamp sensor.

Figure 3-28: Connection diagram of the analog-to-digital interface.



3.4 Noise Sources

The noise sources in the lamp sensor system include the signal conditioning electronics as well as the signal source. Approximate measurements of the noise floor are available from the output by measuring the ac_{rms} voltage of the real-time output. For the purposes of the lamp sensor, the noise floor will be measured as the ac_{rms} voltage of the baseband output from the ADC in a three-second-long window. A nominal range for the total output voltage noise in a three-second window is $50 \rightarrow 150 \mu V_{rms}$ based on time-domain measurements for a signal bandwidth of 6.6Hz from the output of the ADC.

Time-domain measurements show that the noise floor of the lamp sensor system is dominated by differential-mode noise from the fluorescent bulbs and ballast. Comparing the output noise with the source connected to the output noise with source disconnected (connecting and disconnecting the measurement electrodes; the source must remain on in either case because the clock signal for the multiplier is taken from the bulbs), showed that the lamp source was the dominant noise source. The ac_{rms} voltage measured at the output of the ADC was approximately $5 \rightarrow 10 \mu V_{rms}$ without the measurement electrodes connected compared to $50 \rightarrow 150 \mu V_{rms}$ with the electrodes connected.

To quantify the total output noise from the synchronous detector, the output bandwidth must be specified. For the ADC sample rate of 13.7 sps, the effective output bandwidth is [42]

$$BW = 6.6 \text{ Hz.} \quad (3.82)$$

and the effective noise bandwidth for the ADC taken from the datasheet is[42]

$$BW_{neff} = 12.4 \text{ Hz.} \quad (3.83)$$

Frequency-domain measurements of the output voltage noise from the front-end amplifier were taken with a Tektronix RSA3303A Spectrum Analyzer. In order to measure the noise of the front-end amplifier, the inputs are open-circuited. Typically, the inputs to an amplifier are shorted to incremental ground for noise measurements. The difference here, is that the front-end amplifier is a transimpedance or current amplifier rather than a voltage

amplifier. The input-referred voltage noise sources will be gained to the output by a factor of $(1 + \frac{Z_f}{Z_{in}})$, where Z_{in} is the input impedance and Z_f is the feedback impedance. In the current amplifier, Z_{in} is large not small relative to Z_f and so the voltage noise gain is on the order of unity. In a voltage amplifier, Z_{in} is generally small relative to Z_f and so the voltage noise gain will be large. By shorting the input terminals of the transimpedance amplifier, Z_{in} will be the impedance of the wire connecting the input terminal to ground and the voltage noise gain will therefore be very high resulting in an artificially large contribution of the voltage noise source to the output voltage noise. Therefore, the appropriate way to measure the output voltage noise of the transimpedance amplifier is to open-circuit the inputs, or more accurately, to load the inputs with the large impedance that will actually be seen at the input.

In the first plot in Figure 3-29, the spectral density of the output voltage from the front-end is shown from dc to 20 kHz. The 1/f corner occurs at about 2 kHz which is expected from the data sheets for the parts in the front-end amplifier. Above 2 kHz, the noise at the output of the front-end is dominated by thermal rather than 1/f noise and it has a flat spectral density.

The second plot in Figure 3-30, shows the output voltage spectrum around the carrier frequency of 42kHz from the front-end with its inputs disconnected from the electrodes. Examining the spectral density of the output voltage in this case amounts to measuring the noise contributed by the front-end amplifier itself. Around the carrier frequency the noise density is $-18.39 \text{ dB}\mu\text{V}_{rms}/\sqrt{\text{Hz}}$.³ In order to convert the spot noise density to the total voltage noise at the output of the synchronous detector, we convert from $\text{dB}\mu\text{V}_{rms}$ to μV_{rms} ,

$$-18.39 \frac{\text{dB}\mu\text{V}}{\sqrt{\text{Hz}}} = 10^{\frac{-18.39}{20}} \frac{\mu\text{V}_{rms}}{\sqrt{\text{Hz}}} \quad (3.84)$$

$$= 0.12 \frac{\mu\text{V}_{rms}}{\sqrt{\text{Hz}}} \quad (3.85)$$

so that the total output voltage noise is the product of the noise density and the square root

³ $\text{dB}\mu\text{V}/\text{Hz}$ is meant to be $\text{dB}\mu\text{V}/\sqrt{\text{Hz}}$ in the display. This was confirmed by Tektronix Technical Support

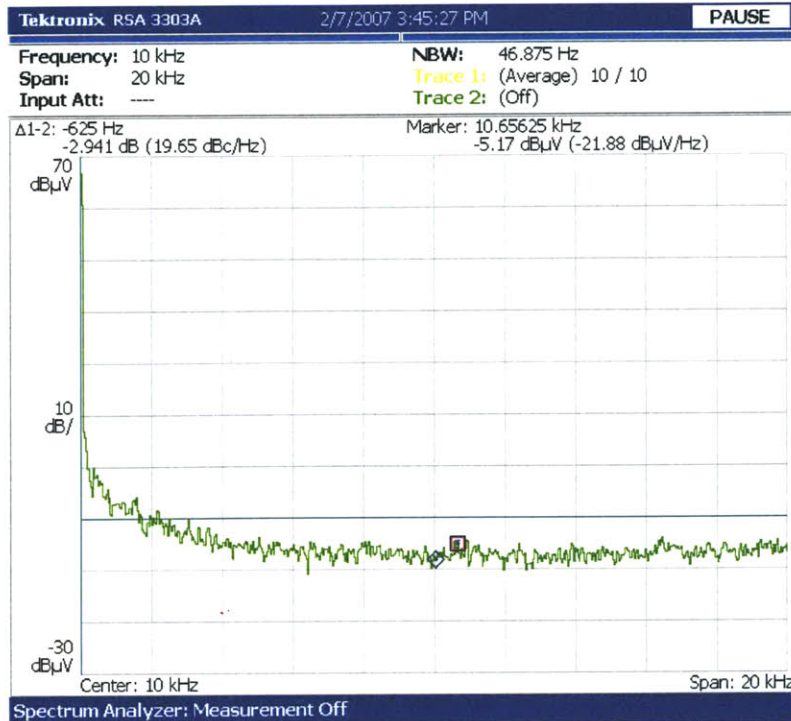


Figure 3-29: Voltage spectral density of the differential output of the front-end amplifier from dc to 20 kHz showing the 1/f corner.

of the effective noise bandwidth:

$$V_{ntot} = 0.12 \frac{\mu V_{rms}}{\sqrt{Hz}} \times \sqrt{12.4 \text{ Hz}} \quad (3.86)$$

The total voltage noise contributed by the front-end amplifier at the output of the synchronous detector according to the frequency-domain measurement is

$$V_{ntot1} = 0.42 \mu V_{rms}. \quad (3.87)$$

For completeness, the total output voltage noise from the front-end measured in the frequency domain is compared to the calculated total output voltage noise using the data sheets. The circuit in Figure 3-31 takes into account the input-referred differential current and voltage noise sources. Common-mode noise sources are not considered because they will be attenuated by the CMRR of the amplifier and will not be measurable at the output compared to the effect of the differential noise sources.



Figure 3-30: Voltage spectral density surrounding the carrier frequency of 42 kHz at the differential output of the front-end amplifier with no input signal and the inputs open-circuited. Interference from other lamps appear as stray signals in the plot.

The total differential output voltage noise from the front-end amplifier can be calculated as follows. Generally, each terminal of the total differential output noise will have a contribution from the input-referred current and voltage noise sources and from the feedback resistor. Treating the feedback resistors as noiseless resistors in parallel with current source thermal noise generators with current noise density $4kT/R$, the total output voltage squared noise density for each output terminal of the amplifier will be

$$e_{no}(s)^2 = e_n^2 \left(1 + \frac{Z_f}{Z_{in}} \right)^2 + i_n^2 Z_f^2 + \frac{4kT}{R_f} Z_f^2, \quad (3.88)$$

in which the voltage noise gain is $\left(1 + \frac{Z_f}{Z_{in}}\right)$ and the current noise gain for the input-referred

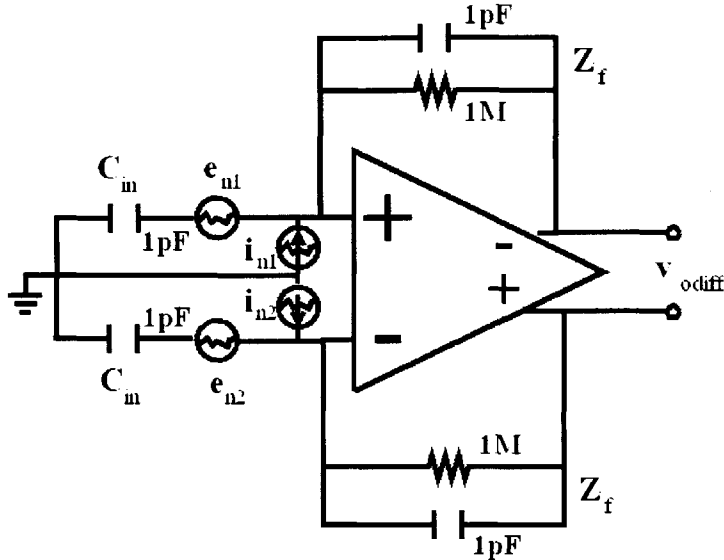


Figure 3-31: Differential circuit for calculating differential output voltage noise from input-referred current and voltage noise sources.

current noise and for the resistor current noise source is Z_f [26], where

$$Z_{in}(s) = \frac{1}{sC_{in}} \quad (3.89)$$

$$Z_f(s) = \frac{R_f}{R_f s C_f + 1}. \quad (3.90)$$

$$(3.91)$$

The total output voltage noise squared for each terminal will be the frequency integral of $e_{no}(jf)^2$ multiplied by the squared frequency response of the system, $|A_v(jf)|^2$:

$$v_{ontot}^2 = \int_0^\infty |A_v(jf)|^2 e_{no}(jf)^2 df. \quad (3.92)$$

The integral is simplified by realizing that the frequency-dependent impedances do not vary much over the small bandwidth of 6.6 Hz. Therefore, nominal values of the impedances are used for the ballast operating frequency of 42 kHz. So,

$$e_{no}(jf) = e_{no} \quad (3.93)$$

and it can be taken out of the frequency integral so that

$$v_{ontot}^2 = e_{no}^2 \int_0^\infty |A_v(jf)|^2 df. \quad (3.94)$$

In this case, the term $|A_v(jf)|$ will represent the low-pass frequency response of the lowest-pass after the demodulator which will be the 6.6Hz bandwidth of the ADC. Approximating $|A_v(jf)|$ as

$$|A_v(jf)| = \frac{1}{1 + j \frac{f}{6.6 \text{ Hz}}}, \quad (3.95)$$

the integral reduces to

$$\int_0^\infty |A_v(jf)|^2 df = \int_0^\infty \frac{1}{1 + (\frac{f}{6.6 \text{ Hz}})^2} = \frac{\pi}{2} \times 6.6 \text{ Hz} = 10.3 \text{ Hz}. \quad (3.96)$$

The difference between the effective noise bandwidth calculated here and the effective noise bandwidth of the ADC listed in the datasheet is due to the fact that the digital low-pass filter in the ADC is not simply a single-pole low-pass filter. Therefore, the actual effective noise bandwidth of 12.4 Hz will be used instead of the approximated effective noise bandwidth of 10.3 Hz.

The total output voltage noise for each terminal is simply

$$v_{ontot} = e_{no} \sqrt{\text{BW}_{neff}} \quad (3.97)$$

$$= \sqrt{12.4 \text{ Hz}} \sqrt{e_n^2 \left(1 + \frac{Z_f}{Z_{in}}\right)^2 + i_n^2 Z_f^2 + \frac{4kT}{R_f} Z_f^2}. \quad (3.98)$$

The total differential output voltage noise is

$$v_{ontotd} = \sqrt{v_{ontot1}^2 + (-v_{ontot2})^2} \quad (3.99)$$

$$= \sqrt{v_{ontot1}^2 + v_{ontot2}^2} \quad (3.100)$$

$$= \sqrt{2v_{ontot1}^2} \quad (3.101)$$

$$v_{ontotd} = \sqrt{12.4 \text{ Hz}} \sqrt{2} \sqrt{e_n^2 \left(1 + \frac{Z_f}{Z_{in}}\right)^2 + i_n^2 Z_f^2 + \frac{4kT}{R_f} Z_f^2}. \quad (3.102)$$

As previously mentioned, the JFET buffers preceding the voltage input terminals of the fully-differential amplifier in the front-end were chosen to have very low input-referred current noise. This advantage is exploited in the following calculation. From the data sheet for the JFET input buffers [36] at the inputs to the front-end amplifier, the input-referred current noise is

$$i_n = 5 \frac{\text{fA}}{\sqrt{\text{Hz}}}, \quad (3.103)$$

and the input-referred voltage noise is actually the combination of the input-referred voltage noise from the JFET buffers e_{njfet} and from the fully-differential op-amp e_{nTI}

$$e_{njfet} = 6 \frac{\text{nV}}{\sqrt{\text{Hz}}} [36] \quad (3.104)$$

$$e_{nTI} = 6.5 \frac{\text{nV}}{\sqrt{\text{Hz}}} [38] \quad (3.105)$$

$$e_n = \sqrt{e_{njfet}^2 + e_{nTI}^2} = 8.8 \frac{\text{nV}}{\sqrt{\text{Hz}}}. \quad (3.106)$$

Values for the impedances at the operating frequency are

$$|Z_{in}| = 3.79 \text{ M}\Omega \quad (3.107)$$

$$|Z_f| = 966 \text{ k}\Omega \quad (3.108)$$

and, Boltzmann's constant is $k = 1.38^{-23} \text{ m}^2 \text{ kg/s}^2 \text{ K}$. The ambient temperature is taken to be $T \approx 300 \text{ K}$. Inserting these values into (3.102) results in

$$v_{ontotd} = 0.61 \mu\text{V}_{rms}, \quad (3.109)$$

which agrees well with the measurements above. In (3.102), it may be intuitive that the voltage noise sources can be neglected because the amplifier is treated as a transimpedance amplifier and not a voltage amplifier. Fundamentally, this intuition is correct because the transimpedance amplifier is measuring currents from a high-impedance network. Therefore, the voltage gain for the noise voltage, $(1 + \frac{Z_f}{Z_{in}})$, will not be much larger than unity. This is the case in our transimpedance amplifier. The voltage squared noise densities con-

tributed by the three noise sources in the front-end amplifier are

$$e_n^2 \left(1 + \frac{Z_f}{Z_{in}} \right)^2 = 6.97 \times 10^{-16} \frac{\text{V}^2}{\text{Hz}} \quad (3.110)$$

$$i_n^2 Z_f^2 = 2.33 \times 10^{-17} \frac{\text{V}^2}{\text{Hz}} \quad (3.111)$$

$$\frac{4kT}{R_f} Z_f^2 = 1.55 \times 10^{-14} \frac{\text{V}^2}{\text{Hz}}. \quad (3.112)$$

Because of the large input impedances, the voltage noise source is negligible. Also, because of the choice of input buffer, the current noise source is negligible. If the inputs to the differential op-amp were left unbuffered, then the input-referred current noise would be $1.25 \frac{\text{pA}}{\sqrt{\text{Hz}}}$ [38] and the output voltage noise squared contribution from the current noise would be

$$i_n^2 Z_f^2 = 1.46 \times 10^{-12} \frac{\text{V}^2}{\text{Hz}}, \quad (3.113)$$

so that the input-referred current noise would dominate among the noise sources and the total output voltage noise would be

$$v_{ontotd,unbuffered} = 6.3 \mu\text{V}_{rms}, \quad (3.114)$$

which is a factor of ten worse than the actual total output noise.

The dominant noise source in the front-end amplifier is the thermal noise in the feedback resistors. This noise source is not however troublesome because the Signal-to-noise ratio (SNR) for a signal input to the transimpedance amplifier increases with the square root of the value of that resistance in general. This can be seen if the feedback impedance is approximated by the resistance.

$$v_{ontotd} \approx \sqrt{\text{BW}_{neff}} \sqrt{\frac{4kT}{R_f} Z_f^2} \quad (3.115)$$

$$Z_f \sim R_f, \quad (3.116)$$

so that

$$v_{ontotd} \approx \sqrt{\text{BW}_{neff} 4kTR_f}. \quad (3.117)$$

But, the signal at the output of the amplifier goes as R_f :

$$v_{o,d} \approx i_{in}R_f, \quad (3.118)$$

so the SNR is approximately

$$\text{SNR} \approx \frac{i_{in}R_F}{\sqrt{\text{BW}_{neff}4kTR_f}} \propto \sqrt{R_f}. \quad (3.119)$$

Therefore, a large resistance value gives more noise contributed by the resistance itself, but the amplification of the input signal increases faster with the value of the resistance so the largest value is optimal for the SNR.

The only other significant noise contributor except for the signal source itself is the voltage reference for the ADC. From the Data sheet of the LT1236, the total output voltage noise from the voltage reference is $5 \mu\text{V}_{rms}$ [40].

The dominant noise source is the differential-mode noise from the signal source itself. The differential-mode noise from the source must be random amplitude variations that are localized along the lengths of the bulbs. Because the coupling between the electrodes and the bulbs varies with the electrode configuration, the noise floor is a function of the electrode configuration. In section 5.1, the electrode configuration will be varied and the noise floor will be remeasured each time. The time-domain ac_{rms} baseband output voltage provides the most readily available measurement of the noise contributed by the source. Real-time measurements and measurements in the range-test both show that the total output voltage noise as the ac_{rms} in a three second window varies between 50 and $150 \mu\text{V}_{rms}$.

Time-domain measurements agree with the noise calculations for the front-end amplifier and band-gap reference above. The ac_{rms} baseband output voltage noise measured by the ADC, without the measurement electrodes connected gives values of $5-10 \mu\text{V}_{rms}$ for a three second window, which agrees well with the expected noise from the front-end amplifier and the voltage reference together. Because the total output noise with the measurement electrodes connected is much greater than the noise contributed by the other sources, the noise contributed by the source is taken to be $50-150 \mu\text{V}_{rms}$.

In summary, the significant noise sources add in quadrature as follows. The front-

end contributes about $1 \mu\text{V}_{rms}$ noise. The band-gap reference used as a reference for the ADC contributes $5 \mu\text{V}_{rms}$ of noise. The bulb and ballast contribute approximately 50-150 μV_{rms} of noise depending on the electrode configuration. The total output voltage noise is consistent with time-domain measurements and is supported by calculation using the data sheets for the significant noise contributors in the electronics and frequency-domain measurements.

Table 3.1: Significant Noise Sources

Source	Noise (μV_{rms})
Front-End Amplifier	1
Band-Gap Reference for ADC	5
Bulbs and Ballast	50 – 150
Total	50.3 – 150.1

Chapter 4

Expected Output Behavior

With an abstraction of the lamp sensor and a lumped element circuit interfaced with signal conditioning electronics, the actual output response to a target can be calculated and simulated. Knowledge of the input characteristics of the front-end amplifier allows for simplification of the lumped element models of Chapter 2. Then, the output response in terms of the lumped elements left in the models can be calculated. The actual response to a target is best predicted with simulation rather than hand calculation due to the complexity of the system which includes the lamp sensor and the target.

4.1 Reduced Reluctance and Capacitance Models

The full lumped element capacitance and therefore dielectric reluctance models can be simplified. The full capacitance model is repeated in Figure 4-1 for convenience.

This model will be simplified using knowledge of the input characteristics of the front-end amplifier, and by neglecting certain capacitances that will not dramatically affect the output response. What makes a capacitance negligible is if it is both small relative to the other capacitances in the system and is present symmetrically in the system as a common-mode capacitance. The latter criterion explains why potentially small differential-mode capacitances of interest are not neglected.

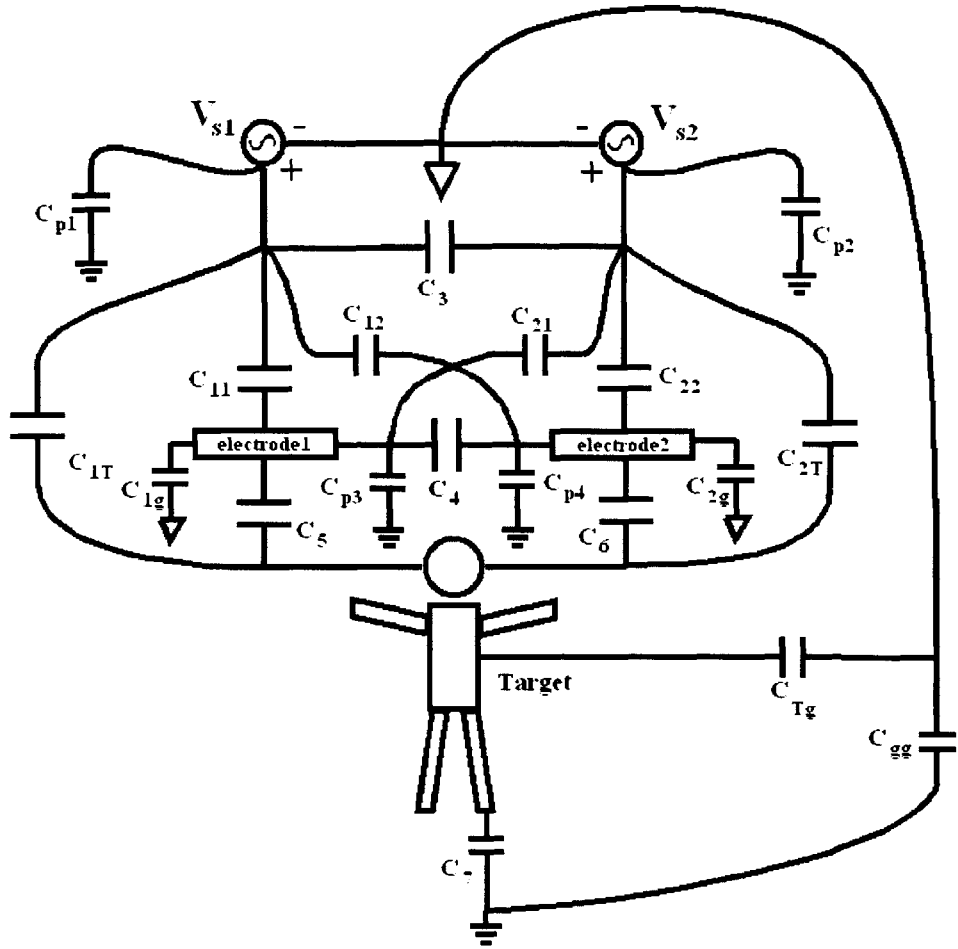


Figure 4-1: The full capacitive model of the lamp sensor and target system.

4.1.1 Stray Capacitances and Negligible Capacitances

Capacitances which can be neglected as small common-mode capacitances include C_{21} and C_{12} because they appear symmetrically and are small relative to C_{11} and C_{22} . Also, C_3 can be decomposed into two equal common-mode capacitances from the sources to incremental ground. Because these capacitances will be small compared to C_{p1} and C_{p2} they can also be neglected. The capacitances, C_{p1} and C_{p2} , between the voltage sources and ground (the backplane) can be ignored because the sources are low-impedance voltage sources.

Next, the input characteristics of the front-end amplifier can be considered in order to eliminate capacitances. One of the input characteristics of the front-end amplifier is that the two input terminals are at the same potential. These input potentials appear at the measurement electrodes. This effectively shorts the capacitance between the two electrodes

eliminating C_4 . Another input characteristic of the amplifier is that shunt impedances are effectively multiplied by the open-loop gain of the amplifier and are therefore negligibly large. Therefore, the stray capacitances between the measurement nodes and ground can be ignored. This eliminates the stray capacitances C_{p3} and C_{p4} and the capacitances from the electrodes to the incremental source ground, C_{1g} and C_{2g} . Eliminating all of these capacitances leaves us with the simplified or reduced lumped element capacitance model in Figure 4-2.

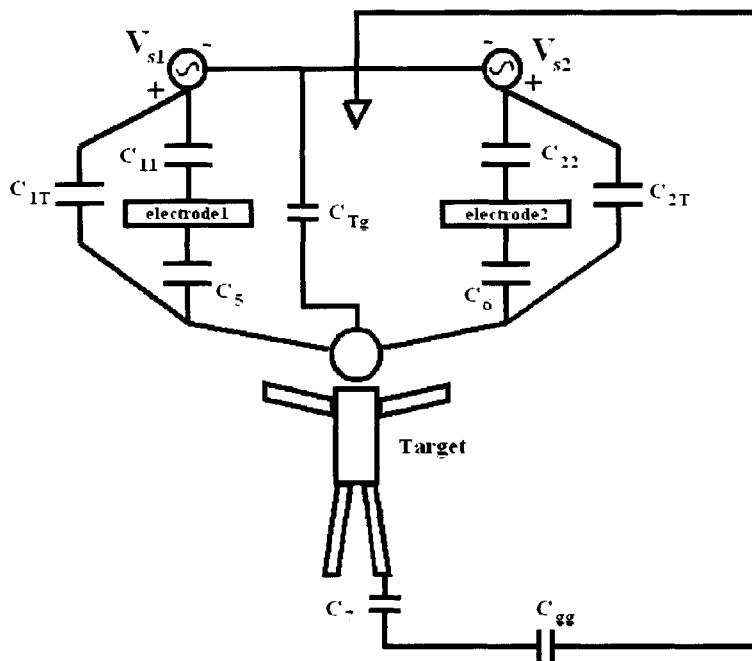


Figure 4-2: Reduced capacitance model.

By replacing the capacitances with dielectric reluctances and the voltage sources with EMF sources as in Chapter 2, the reduced dielectric reluctance model can be extracted from the reduced capacitance model. The reduced dielectric reluctance model is shown in Figure 4-3.

The basic operating principles of detection are clear from the lumped element models. Electric flux couples to the measurement electrodes through dielectric reluctances T_{11} and T_{22} . Some extra electric flux appears at the measurement electrodes via dielectric reluctances from the source to the target $T_{1T,2T}$ and from the target back to the electrodes $T_{5,6}$. The differential measurement is nulled for the “no detection” case by setting up the elec-

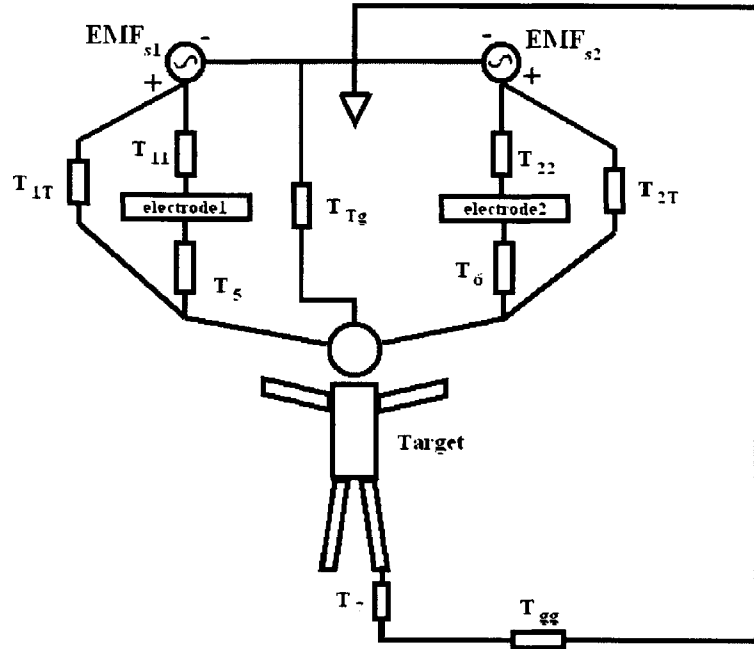


Figure 4-3: Reduced dielectric reluctance model.

trodes so that they couple to the source equally. This means that the dielectric reluctances T_{11} and T_{22} are equal. The combinations of T_{1T} and T_5 and of T_{2T} and T_6 are detected as differential dielectric reluctances and have the effect on the output that is summarized in Figure 3-2. The combination of dielectric reluctances T_{Tg} , T_7 , and T_{gg} provides a return path to incremental ground for the electric flux.

4.2 Expected Output Response

In general, we expect the output differential voltage to behave in the following way. A target that is close to one electrode and far from the other should result in a non-zero differential output voltage. If the target is then closer to the second electrode instead, this should result in a differential output voltage of the opposite sign. The differential measurement between the two electrodes should result in the two electrodes having an equal but opposite effect on the output response. For example, imagine a human target passing below the lamp sensor, walking first below one electrode and then below the other electrode. The differential output voltage response of the system should deviate from 0 V in one direction, then return

to 0 V as the target is centered between the two electrodes and then it should deviate in the other direction before returning to 0 V as the target passes under the second electrode and finally out of the detection range. With this response, the direction and even velocity of the target can be readily measured. Measurements of more subtle variables in the detection field will be discussed in Chapter 6.

4.2.1 Calculated Output Response

In order to calculate the output response of the system, we extract a circuit model of the system from the physical capacitive model and evaluate how the differential amplifier measures the currents in that circuit. The differential-mode capacitive circuit extracted from the physical model is shown in Figure 4-4. Because the front-end amplifier draws a differential current such that its input terminal voltages remain equal, the differential current can be modeled as the current that would flow through a short from one electrode to the other electrode, labeled i_{diff} . It is important to distinguish between this circuit model and one in which the differential current is the difference in currents from one electrode to ground and from the other electrode to ground. In the latter case, the input common-mode voltage of the front-end amplifier would have to be fixed. The differential amplifier does not constrain its input common-mode voltage to be fixed. It only constrains the voltage between its two input terminals to be 0 V. Therefore, the common-mode input voltage can vary and the appropriate circuit model is simply a short from one electrode to the other due to the small differential input impedance of the amplifier.

$$i_{diff} = i_1 - i_2. \quad (4.1)$$

i_{diff} can be solved for by using linear superposition of the two sources. Figures 4-5 and 4-6 show half circuits in which one voltage or EMF source is shorted to ground and the current or flux due to the other can be calculated. In order to avoid defining capacitive impedances for each capacitance in the circuit, we will derive the differential output first from the dielectric reluctance model. It will then be simple to rewrite the result in terms of capacitances.

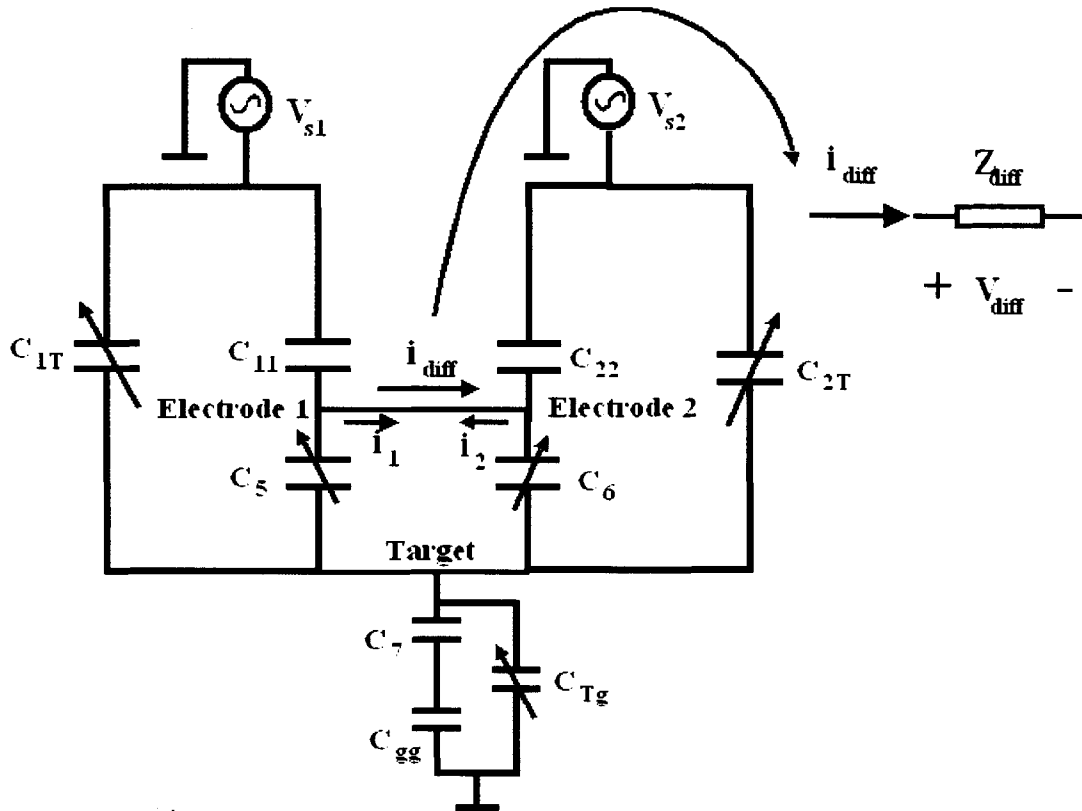


Figure 4-4: Incremental capacitive circuit extracted from the physical model and interfaced with the transimpedance amplifier.

In order to calculate the differential output voltage due to the target below the lamp, first we need to calculate the differential current between the two electrodes. In the dielectric reluctance circuit we start by calculating the effective differential electric flux and then convert the result to current. In the dielectric reluctance circuit, EMF and electric flux act on dielectric reluctance as voltage and current do on impedance. To solve the circuit, we begin by writing node equations to constrain the independent EMF nodes labeled, v_1 and v_2 . This results in two independent equations:

$$\frac{\mathcal{E}_1 - v_1}{T_{11}} = \frac{v_1}{T_{22}} + \frac{v_1 - v_2}{T_5 \parallel T_6} \quad (4.2)$$

$$\frac{v_2}{T_7} = \frac{\mathcal{E}_1 - v_2}{T_{1T}} + \frac{v_1 - v_2}{T_5 \parallel T_6} + \frac{0 - v_2}{T_{2T}}. \quad (4.3)$$

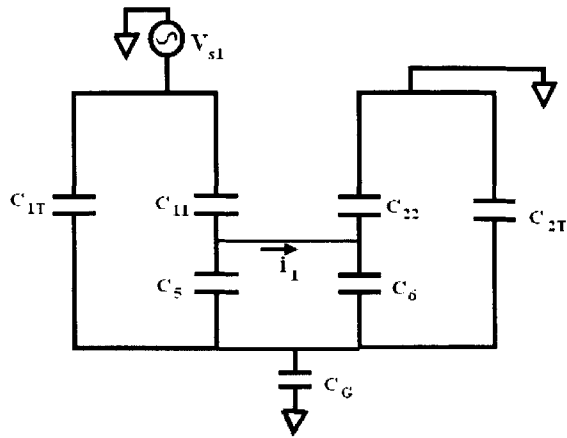


Figure 4-5: A capacitive half circuit for calculating differential current in the capacitive system.

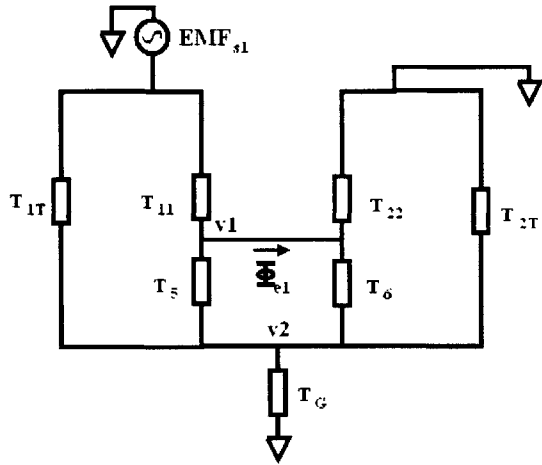


Figure 4-6: A dielectric reluctance half circuit for calculating differential electric flux in the capacitive system.

Isolating the node variables,

$$v_1 \left(\frac{1}{T_{22}} + \frac{1}{T_5 \parallel T_6} + \frac{1}{T_{11}} \right) = \frac{\mathcal{E}_1}{T_{11}} + \frac{v_2}{T_5 \parallel T_6} \quad (4.4)$$

$$v_2 \left(\frac{1}{T_G} + \frac{1}{T_{1T}} + \frac{1}{T_5 \parallel T_6} + \frac{1}{T_{2T}} \right) = \frac{\mathcal{E}_1}{T_{1T}} + \frac{v_1}{T_5 \parallel T_6}. \quad (4.5)$$

The quantities in parentheses are lumped for simplicity as

$$\left(\frac{1}{T_{22}} + \frac{1}{T_5 \parallel T_6} + \frac{1}{T_{11}} \right) \equiv Y_1 \quad (4.6)$$

$$\left(\frac{1}{T_G} + \frac{1}{T_{1T}} + \frac{1}{T_5 \parallel T_6} + \frac{1}{T_{2T}} \right) \equiv Y_2 \quad (4.7)$$

and they are symmetric in the circuit so they will be the same when superposing the effect of the opposite EMF source.

Solving for v_2 in terms v_1 and vice versa gives

$$v_1 = \frac{1}{Y_1} \left(\frac{\mathcal{E}_1}{T_{11}} + \frac{v_2}{T_5 \parallel T_6} \right) \quad (4.8)$$

$$v_2 = \frac{1}{Y_2} \left(\frac{\mathcal{E}_1}{T_{1T}} + \frac{v_1}{T_5 \parallel T_6} \right). \quad (4.9)$$

Eliminating v_1 from v_2 and vice versa gives

$$v_1 = \frac{\mathcal{E}_1(\frac{1}{T_{11}} + \frac{1}{T_{1T}Y_2T_5\|T_6})}{Y_1(1 - \frac{1}{Y_1Y_2(T_5\|T_6)^2})} \quad (4.10)$$

$$v_2 = \frac{1}{Y_2} \left(\frac{\mathcal{E}_1}{T_{1T}} + \frac{1}{T_5\|T_6} \left(\frac{\mathcal{E}_1(\frac{1}{T_{11}} + \frac{1}{T_{1T}Y_2T_5\|T_6})}{Y_1(1 - \frac{1}{Y_1Y_2(T_5\|T_6)^2})} \right) \right). \quad (4.11)$$

The flux due to the first source then is

$$\Phi_{e1} = v_1 \left(\frac{1}{T_{22}} + \frac{1}{T_6} \right) - \frac{v_2}{T_6} \cdot e^{-j\frac{\pi}{2}} \quad (4.12)$$

in which the exponential term represents the phase shift from current to electric flux. Similarly the electric flux in the opposite direction due to the other source will be

$$\Phi_{e2} = v'_1 \left(\frac{1}{T_{11}} + \frac{1}{T_5} \right) - \frac{v'_2}{T_5} \cdot e^{-j\frac{\pi}{2}} \quad (4.13)$$

where

$$v'_1 = \frac{\mathcal{E}_2(\frac{1}{T_{22}} + \frac{1}{T_{2T}Y_2T_5\|T_6})}{Y_1(1 - \frac{1}{Y_1Y_2(T_5\|T_6)^2})} \quad (4.14)$$

$$v'_2 = \frac{1}{Y_2} \left(\frac{\mathcal{E}_2}{T_{2T}} + \frac{1}{T_5\|T_6} \left(\frac{\mathcal{E}_2(\frac{1}{T_{22}} + \frac{1}{T_{2T}Y_2T_5\|T_6})}{Y_1(1 - \frac{1}{Y_1Y_2(T_5\|T_6)^2})} \right) \right) \quad (4.15)$$

and the effective differential electric flux is

$$\Phi_{e,diff} = \Phi_{e1} - \Phi_{e2} = \left(v_1 \left(\frac{1}{T_{22}} + \frac{1}{T_6} \right) - v'_1 \left(\frac{1}{T_{11}} + \frac{1}{T_5} \right) - v_2 \frac{1}{T_6} + v'_2 \frac{1}{T_5} \right) \cdot e^{-j\frac{\pi}{2}}. \quad (4.16)$$

Converting the dielectric reluctance result to a capacitive result goes as follows. EMF will be converted to voltage so the node potentials v_1 and v_2 can be left alone. Flux is converted to current according to

$$i_{diff} = \Phi_e \epsilon \omega \cdot e^{j\frac{\pi}{2}}, \quad (4.17)$$

in which the exponential term represents the phase shift from electric flux to current and

dielectric reluctance is converted to capacitance according to

$$T = \frac{\epsilon}{C}. \quad (4.18)$$

The differential current is

$$i_{diff} = \epsilon\omega \left(v_1 \left(\frac{C_{22}}{\epsilon} + \frac{C_6}{\epsilon} \right) - v'_1 \left(\frac{C_{11}}{\epsilon} + \frac{C_5}{\epsilon} \right) - v_2 \frac{C_6}{\epsilon} + v'_2 \frac{C_5}{\epsilon} \right) \quad (4.19)$$

and the differential output voltage, $v_{o,d}$ is simply the product of the differential transimpedance Z_d and the differential current, i_{diff} :

$$v_{o,d} = Z_d \omega (v_1(C_{22} + C_6) - v'_1(C_{11} + C_5) - v_2 C_6 + v'_2 C_5) \quad (4.20)$$

The form of the differential output voltage is complicated although it will be useful for simulating the output response. However, the symmetry in (4.20) is telling of the opposite effect that the target will have when it is below one electrode versus when it is below the other. Furthermore, it can be seen that the output voltage will be 0 V when the system is physically nulled. In order to null the output of the system in the absence of a detection, C_{11} and C_{22} are set equal to each other by matching the distances between the lamp and the two electrodes. Upon examining (4.20) with the system nulled,

$$C_{11} = C_{22} \quad (4.21)$$

and in the event of no detection,

$$C_5 = C_6 \quad (4.22)$$

$$C_{1T} = C_{2T}, \quad (4.23)$$

and noting that the two voltage sources are equal

$$\mathcal{E}_1 = \mathcal{E}_2, \quad (4.24)$$

the node potentials resulting from each source become equal:

$$v_1 = v'_1 \quad (4.25)$$

$$v_2 = v'_2, \quad (4.26)$$

and the differential output voltage vanishes

$$v_{diff} = 0 V \quad (4.27)$$

as expected. The system is nulled in practice by adjusting the electrode depths from the lamp and watching the output voltage approach 0 V. One electrode depth is fixed and then the other is adjusted until the output voltage is relatively close to 0 V. The closeness of the output voltage to 0 V determines the CMRR degradation of the front-end amplifier due to the mismatch in the input capacitances as described in Section 3.1.4.

4.2.2 Simulated Output Response

We would like to verify that the output voltage of our system in simulation matches our intuition. Therefore, we would like to plot the differential output voltage as a human target walks below the lamp. In Chapter 5 these simulations will be compared to real collected data. For the time being, the strength of the alternating voltage source,

$$V_s \equiv |V_1| = |V_2| = |\mathcal{E}_1| = |\mathcal{E}_2|, \quad (4.28)$$

has still not been directly measured, so the simulated output voltage is left normalized by the voltage source magnitude. By comparing the simulated output response to the real output response in Chapter 5, a value for V_s will be obtained.

In order to obtain values for the capacitances below the lamp as a human target passes by, the finite-element modeling software Fastcap is used[21]. The first Fastcap model presented represents a case in which the lamp is on its side and the human is walking at a fixed distance in front of the lamp. This is because in the lab, the lamp sensor was initially



Figure 4-7: A screenshot of the Fastcap model for the horizontal lamp setup.



Figure 4-8: A screenshot of the Fastcap model for the hanging lamp setup.

mounted this way for prototyping. Therefore, the range test in Chapter 5 was taken for this configuration and we should have simulations to compare to that data. Simulated output of the more likely case, in which the human is walking below a hanging lamp, will also be presented. A screenshot of the first model in Fastcap is shown in Figure 4-7 including the lamp sensor and human. The lamp sensor consists of two bulbs, two electrodes, and the backplane to the lamp. The human is represented by a rectangular solid. The overall permittivity is the permittivity of free space which is approximately equal to the permittivity of air. Nominal values for the fixed capacitances were simulated in Fastcap and then held constant throughout the simulation of the target passing under the lamp. The capacitances C_{11} and C_{22} remain constant throughout the simulation at 1 pF. The capacitance from the target to ground, C_G , remains constant at 10 pF. The capacitance from the floor to the incremental source ground, C_{gg} , remains constant at 1 pF. Also, the capacitance from the target to the incremental source ground, C_{Tg} , varies as the target moves and is approximated as the average of the capacitances from the target to each voltage source.

An example of the Fastcap output capacitance matrix for the model is shown in Figure

4-9. In the capacitance matrix each row and column represents a conductor in the system. The intersections in the matrix are capacitances between two conductors and are output as negative values. The diagonal elements are self-capacitances. The conductors in the Fastcap model are described in Table 4.1.

```
CAPACITANCE MATRIX, femtofarads
      1       2       3       4       5       6
1%model.1st 1 2.938e+004   -4352    -2534   -82.36  -229.6 -1.852e+004
1%GROUP2    2       -4352  2.932e+004   -85.03   -2548   -269.6 -1.841e+004
1%GROUP3    3       -2534   -85.03    5511   -19.38   -78.84   -1490
1%GROUP4    4       -82.36   -2548    -19.38    5510   -98.08   -1471
1%GROUP5    5       -229.6   -269.6   -78.84   -98.08  4.778e+004   -1126
1%GROUP6    6  -1.852e+004 -1.841e+004   -1490   -1471   -1126  5.818e+004
```

Figure 4-9: An example of the Fastcap output matrix.

Table 4.1: Conductors in the Fastcap model.

Conductor	Description
1	V_1
2	V_2
3	Left Electrode
4	Right Electrode
5	Target
6	Backplane

Matlab scripts were written to read in a file that is filled with matrices of the kind in Figure 4-9 and extract the capacitances of interest with the correct units. Those scripts can be found in Appendix B. The scripts plot the differential output voltage normalized by the voltage source magnitude V_s for each matrix. By producing a matrix for discrete configurations that simulate the human passing in front of the lamp, a plot is generated that simulates the output response of the lamp sensor to a human passing in front of the lamp in time. A plot of this kind is shown in Figure 4-10. *In this simulation the electrodes were spaced 39in. apart symmetrically about the center of the lamp. The electrodes are at a depth of 3in. in front of the lamp and the detection range to the human is 4ft. which is the closest range in the data taken for the range test in Chapter 5.*

A simplifying assumption is made because the simulation plots the output response as the position of the target changes without regard for the velocity with which the target is

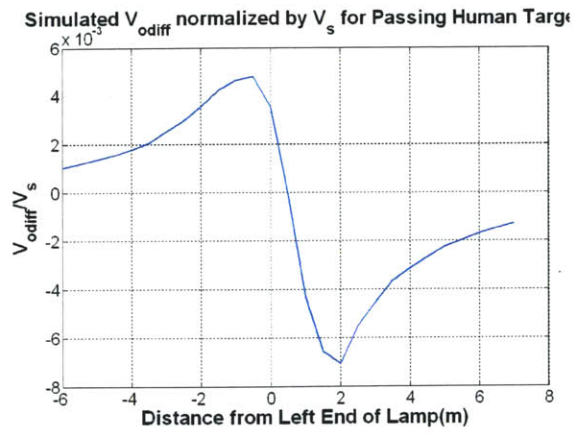


Figure 4-10: A plot of the simulated output voltage as a human target passes in front of the lamp.

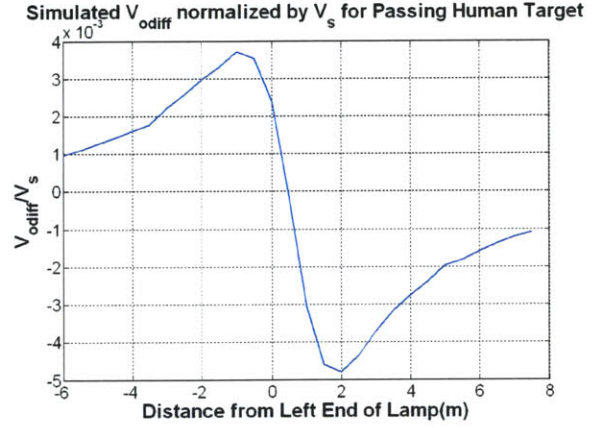


Figure 4-11: A plot of the simulated output voltage as a human target passes below the lamp.

passing below the lamp. The assumption then, is that the target in the simulation is moving slowly enough that the output bandwidth of the lamp sensor does not attenuate the output response. The simulated plots are shown as the normalized output voltage vs. distance from one end of the lamp rather than normalized output voltage vs. time.

The plot of the output voltage in response to a human passing in front of the lamp matches our intuition. The differential output voltage begins at 0 V, deviates in one direction, then the other and the returns to 0 V as the target passes out of the detection range.

The simulation was repeated for the more likely case in which the human is passing below a hanging lamp. In this simulation the range of detection, which is the perpendicular distance between the lamp and the top of the target, is 4ft. The electrode spacing and depth is the same as it was in the previous simulation. A screenshot of the model for this simulation is shown in Figure 4-8. The simulated, normalized output voltage response is plotted in Figure 4-11.

Chapter 5

Results, Data Analysis and Demonstration

A prototype lamp sensor was used to collect data in a range test for a human target walking below the lamp and for building a real-time output demonstration. A photograph of the cart-mounted lamp sensor prototype is shown in Figure 5-1. In this Chapter, data from the lamp sensor as well as code and output for a real-time demonstration in MATLAB are presented. Comparing the measured output response to the simulated output response, a value for the strength of the effective voltage source will be calculated.

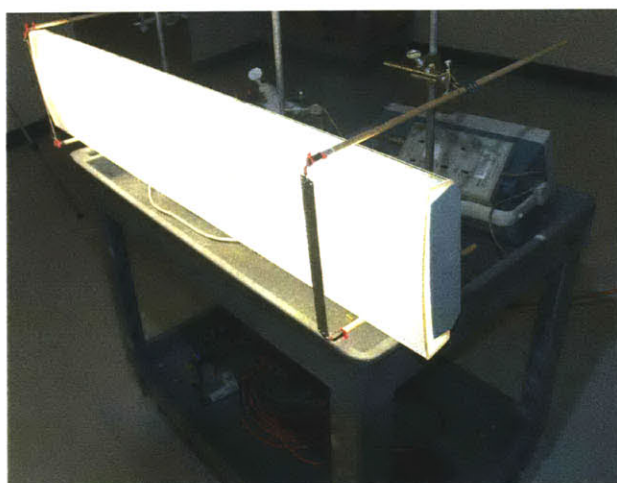


Figure 5-1: A photograph of the cart-mounted prototype lamp sensor.

5.1 Measured Output Response and Range Test Data

The measured output response matches the expected output response. Examples of the output voltage data collected from the cart-mounted lamp sensor as a 6 foot tall human target walks in front of the lamp are shown in Figure 5-2. In the data collection, the situation represents the situation modeled by the horizontal configuration in Figures 4-7 and 4-10. The range of detection is labeled underneath each of the pots in Figure 5-2. The range is defined as the perpendicular distance between the fluorescent bulbs and the closest edge of the human target to the lamp. Comparing the plots of the output response data collected from the lamp sensor to the simulated output response, it is clear that the model developed for the lamp sensor system is well-matched to the real lamp sensor system.

The detection range varies as a function of the electrode configuration. Because a differential measurement is taken between two electrodes, varying the relative length-scale of the separation of the electrodes and the depth of the electrodes from the lamp with respect to the detection range, the sensitivity is varied. The data in the plots of Figure 5-2 are taken from an electrode configuration that resulted in one of the longest detection ranges.

Data was taken in 20 different electrode configurations. Each configuration consisted of an electrode spacing and depth from the lamp. Each sample consisted of one pass of a target person walking in front of the horizontally mounted lamp. The metric for each sample was the ac_{rms} output voltage ($V_{ac,rms}$). For each configuration, 10 control samples were taken with no target passing under the lamp. Then, for each range in each electrode configuration, 5 samples were taken of a target person passing under the lamp.

A Z-test [12] in MATLAB was performed on the data comparing each 5-sample set of data to the control set for that configuration. The chosen detection rule is that the sample set must demonstrate a mean $V_{ac,rms}$ larger than that of the control sample set with a confidence level of 99% or better. The data is shown in Table 5.1 at the boundary of the detection rule. The range varies along the columns. The configuration varies along the rows. Each configuration is labeled as an electrode spacing (the distance between the two electrodes) and electrode depth (the distance from the lamp to the electrodes).

The Z-test measures the statistical likelihood that the means of two gaussian-distributed

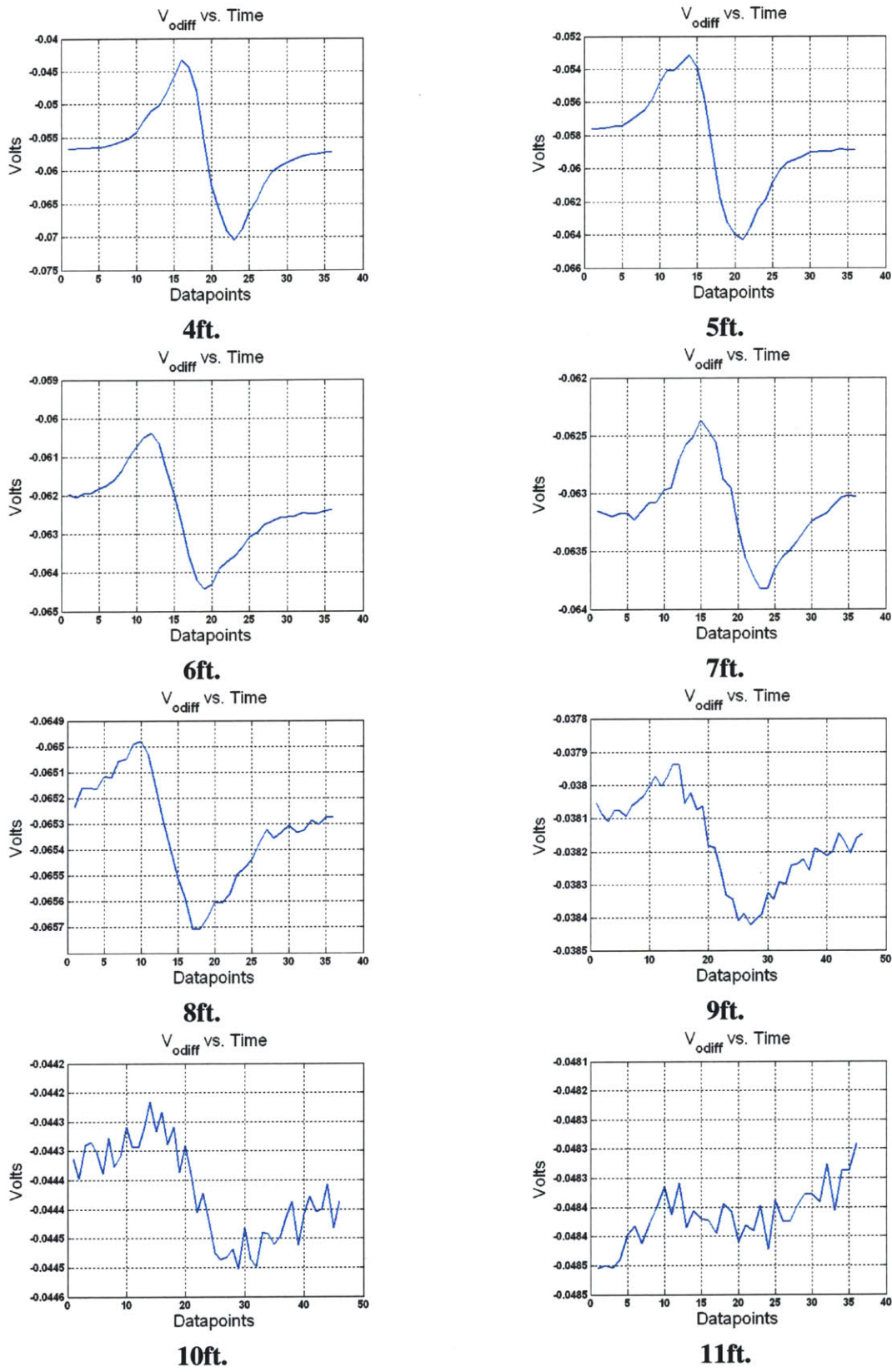


Figure 5-2: Examples of plots of sample detections from the range test. [Configuration 44x5]

random variables are different based on the mean and variance calculated from sample sets of the two variables. We introduce the *p-value* to quantify the confidence level of detection where, p is the probability that the means of the two sample sets are equal. Thus a higher *p-value* signifies a higher probability that there is no detection. Therefore, the confidence level α that there has been a detection is defined as:

$$\alpha = 1 - p. \quad (5.1)$$

or, the percent confidence that there has been a detection is

$$P_C = 100\alpha. \quad (5.2)$$

So, for example the percent confidence for the 10 foot range in the configuration with the electrodes two inches from the lamp and 28 inches apart (2x28) is

$$P_C = 100(1 - p) = 100(1 - 0.027) = 97.3\% \quad (5.3)$$

and it is rejected as a detection based on the 99% confidence level rule.

In the table, a *p-value* of 0 means nearly zero, so that the confidence level is negligibly less than 100%. “N/A” means that a range lesser than the current range has shown questionable detection and this range is not considered. Thus the *p-values* for sample sets up to the first sample set when $p > 0.01$ or $100\alpha < 99\%$ are shown in the table. Also, all *p-values* at the detection range boundary that are less than 10^{-7} are listed as $< 10^{-7}$. The noise floor is listed with each configuration. It is calculated as the mean of the $V_{ac,rms}$ measurements for the 10 control samples taken for that configuration.

For each configuration the two ranges which straddle the detection range are highlighted. The trend for the detection range to decrease as the electrode spacing and depth decreases matches our intuition about controlling the detection range by controlling the electrode configurations. The example plots of output data samples in Figure 5-2 were taken for the configuration in the table with electrode spacing of 44in. and depth of 5in. (44x5). It is interesting to compare the time-domain waveforms in the plots with the sta-

tistical analysis in the table. In the plots near the edge of the detection range, the random noise variations become prominent. At the range of 11ft., the noise begins to overwhelm the deviations caused by the target. In the table, the 11ft. range is considered marginal in terms of confidence level of detection. This is consistent with the time-domain data plot in which the deviations from the target are slightly noticeable, but the noise variations are significant.

Table 5.1: Detection Data p – values for Various Electrode Configurations at the Limit of the Detection Range.

Spacing(in.)	Depth(in.)	p-values					Noise Floor ($\mu\text{V}_{ac,rms}$)
		7ft.	8ft.	9ft.	10ft.	11ft.	
44	5	0	0	0	2.53×10^{-4}	0.328	54.5
	4	0	0	4.63×10^{-7}	0.0165	N/A	65.1
	3	0	0	0	4.85×10^{-6}	0.661	98.9
	2	0	$< 10^{-7}$	0.0426	N/A	N/A	168.5
38	5	0	0	3.05×10^{-5}	0.0240	N/A	61.8
	4	0	0	4.93×10^{-5}	0.865	N/A	67.3
	3	0	0	$< 10^{-7}$	0.133	N/A	62.7
	2	0	0	0.00200	0.0160	N/A	74.0
28	5	0	0	0	$< 10^{-7}$	0.306	45.2
	4	0	0	1.19×10^{-4}	0.676	N/A	70.7
	3	0	0	$< 10^{-7}$	0.884	N/A	52.3
	2	0	2.62×10^{-5}	0.00100	0.0270	N/A	65.3
19	5	0	$< 10^{-7}$	0.382	N/A	N/A	55.4
	4	0	0	$< 10^{-7}$	0.126	N/A	41.6
	3	0	$< 10^{-7}$	0.0120	N/A	N/A	45.4
	2	0	0	1.01×10^{-5}	0.0340	N/A	42.2
15	5	0	$< 10^{-7}$	0.0360	N/A	N/A	40.9
	4	$< 10^{-7}$	0.0210	N/A	N/A	N/A	51.5
	3	0	$< 10^{-7}$	0.0640	N/A	N/A	49.9
	2	$< 10^{-7}$	0.0120	N/A	N/A	N/A	57.2

5.2 Signal Source Magnitude Calibration

So far, the simulated output response has been normalized by the strength of the effective voltage source V_s . By comparing samples of the measured and simulated data, a value for V_s can be calculated. Because the synchronous detector measures the rms voltage at the output of the differential front-end amplifier, the units of V_s are rms Volts.

The data in Table 5-4 is the peak deviation for a person walking in front of the horizontally oriented lamp at a range of 4ft., with the electrodes separated by 39in. and at a depth of 3in. from the lamp. Plots of the data samples are overlayed in a plot in Figure 5-3. This data can be compared to simulated data which was normalized by the magnitude of V_s be-

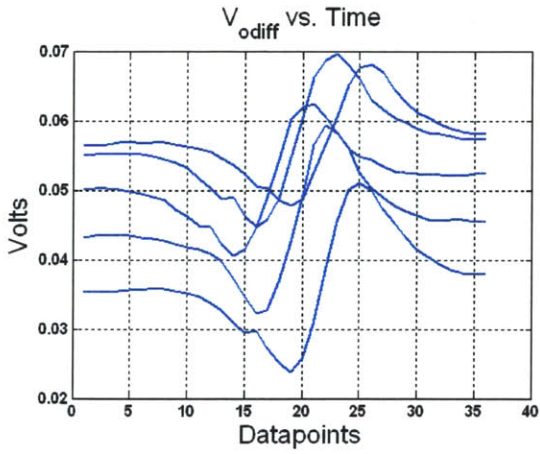


Figure 5-3: Overlayed plots of the real output response for calibration of V_s .

Trial	Peak Deviation (mV)
1	13.6
2	13.5
3	11.0
4	12.5
5	10.2
Average	12.1

Figure 5-4: Tabulated data of the peak deviation of the real output response for calibration of V_s .

cause the physical configuration is the same. The simulated output data normalized by V_s showed an average peak deviation of $5.94mV/V_{rms}$. Finally, we can deduce the magnitude of V_s as

$$V_s = \frac{12.1mV}{5.94mV/V_{rms}} = 2.04V_{rms}. \quad (5.4)$$

$$\boxed{V_s = 2.04V_{rms}}. \quad (5.5)$$

The voltage source magnitude above was calculated for a specific situation which consists of electrode configuration and clock generation scheme. The voltage source magnitude that was calculated is a good nominal value for the effective voltage source strength particularly because the situation for which it was calculated is a configuration with maximum detection range and reasonable geometry. However, it is important to understand that varying the electrode configuration or the geometry of the lamp itself changes the effective strength of the measured voltage source. Keep in mind that the alternating surface potential on one bulb changes in magnitude as we move along the length of the bulb. Changing the electrode configuration in spacing will change the strength of the alternating electric voltage seen by the two electrodes. Changing the electrode depth from the lamp will also change the effective voltage seen by the two electrodes because they will couple more weakly to the segments directly behind the electrodes and more strongly to the segments to

the sides of the electrodes. Therefore, having a generalized voltage source magnitude for each case is very complicated and only useful for simulating absolute responses. That is why the simulated output response was left normalized by V_s until now.

5.3 Real-Time MATLAB Demonstration

Data from the lamp sensor, can be transferred to a PC via an RS-232 connection in real-time. This allows for real-time detection of targets below the lamp. MATLAB scripts were written to interface a PC with the lamp sensor using the serial port. These scripts can be found in Appendix B. A screenshot of the output of the real-time MATLAB demonstration is shown in Figure 5-5. The demonstration output consists of three plots. The top two plots are real-time output voltage data. The top plot is auto-scaled to show the largest variations in the output data. Therefore, in the case of no detection this plot shows random noise variations. The middle plot is a fixed-scale window showing the same real-time output voltage data. The lowest plot is a record of what MATLAB detects as an event below the lamp.

When initialized, the demonstration takes data in the absence of a detection in order to calibrate itself. This calibration sets the minimum auto-scale and represents a measurement of the noise-floor at the output of the lamp sensor. An event is detected as a significant deviation in the ac_{rms} output voltage compared to the calibrated noise level. In the screenshot, the bottom plot shows a record of output voltage data that depicts a person walking below the lamp at a range of 5ft. Incidentally, the deviation shown in the top plot depicts the operator moving under the lamp to push the print-screen button for the screen capture, so this Figure shows both event recognition and real-time detection.

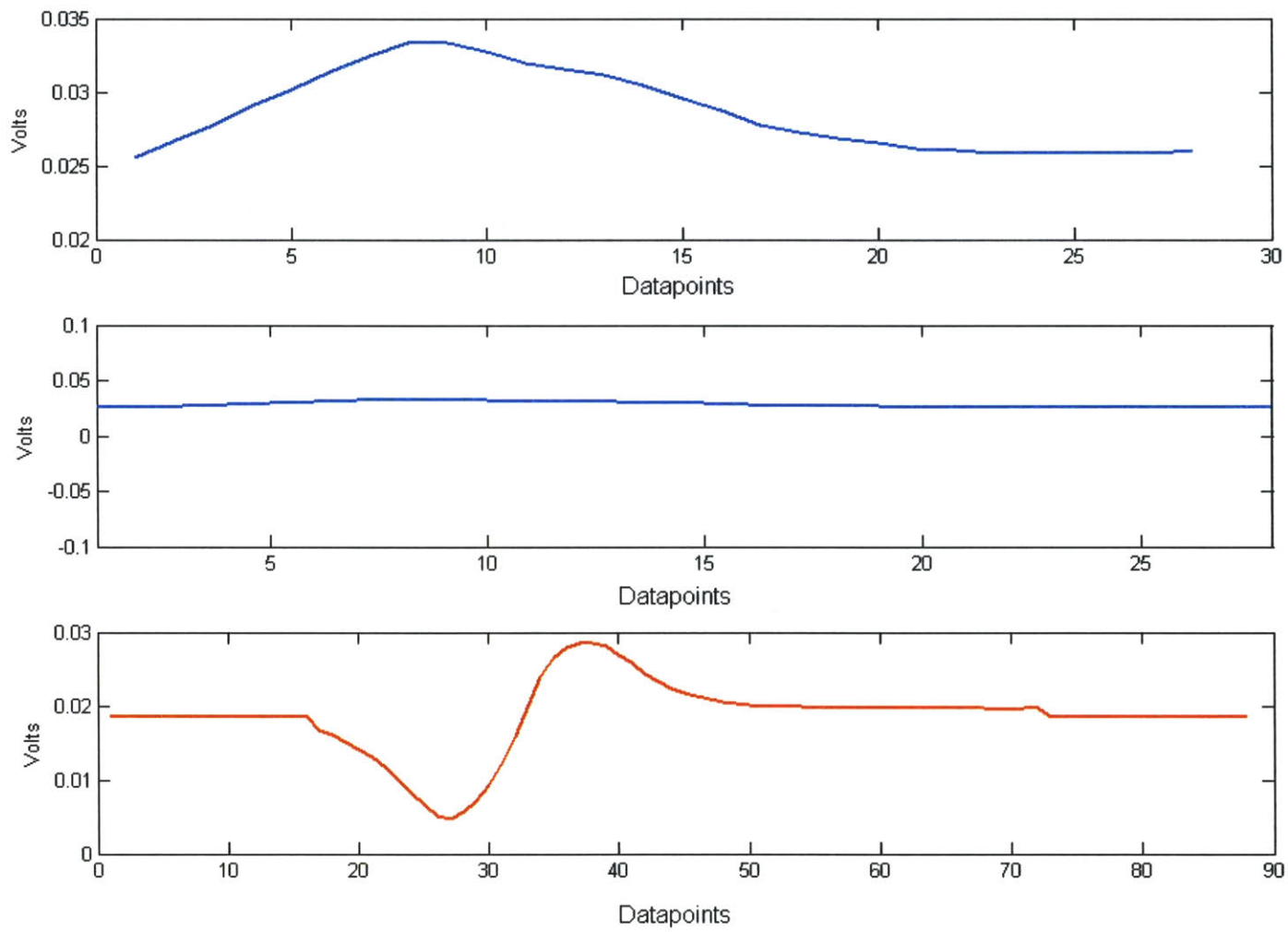


Figure 5-5: A screenshot of the real-time Matlab demo.

Chapter 6

Multiple Electrode Pair System and Further Work

The lamp sensor has been demonstrated as a proof of concept for detection of human targets at practical ranges below the lamp. Up to this point, the information presented in this work will be useful in understanding the operating principles of the lamp sensor, how a useful signal can be conditioned from its output and in making further intelligent decisions to improve the system and to add functionality. This chapter will explore the initial results from one particular extension of the lamp sensor system. It will then conclude with a description of the limitations of the prototype system, suggestions for further work, and possible immediate improvements and oversights revealed in the writing of this work. In Appendix A, some practical considerations for repeating the results in this work are described.

6.1 Controlling the Sensing Range

In Section 5.1, the measured data reflected the fact that the detection range is dependent on the electrode configuration. The lamp sensor takes a differential measurement between two electrodes. By decreasing the distance between those two electrodes, the difference in the electric field seen by the two electrodes should also decrease. The data showed that by decreasing either the electrode spacing (the distance between the two electrodes) or the electrode depth (the distance between the lamp and the electrodes), the detection range

decreased. In this chapter, the electrode spacing will be varied to control the sensitivity of the lamp sensor.

It is intuitive that decreasing the electrode spacing should decrease the sensitivity of the differential measurement. Decreasing the length-scale of the separation between the electrodes relative to the length-scale of detection decreases the difference measurement between the two electrodes. Fastcap was used to simulate the effect of varying the electrode spacing on the sensing range. The human target was a fixed distance of four feet from the lamp and was always standing directly in front of the right electrode. The electrode spacing varied from 47 inches (the full length of the lamp) to seven inches (the spacing at which the output response nearly vanishes) with the electrodes always spaced symmetrically about the center of the lamp and always at a fixed depth of three inches from the lamp. The effect of changing the electrode configuration on the effective voltage source strength was discussed in Section 5.2. For the simulation, the voltage source strength was taken to be constant at 1 V_{rms} . A more accurate simulation would incorporate the change in the effective voltage source strength when varying the electrode configuration. However, only the effect of the electrode spacing on the differential measurement is considered here. Figure 6-1 shows a plot of the simulated output voltage deviation as the electrode spacing

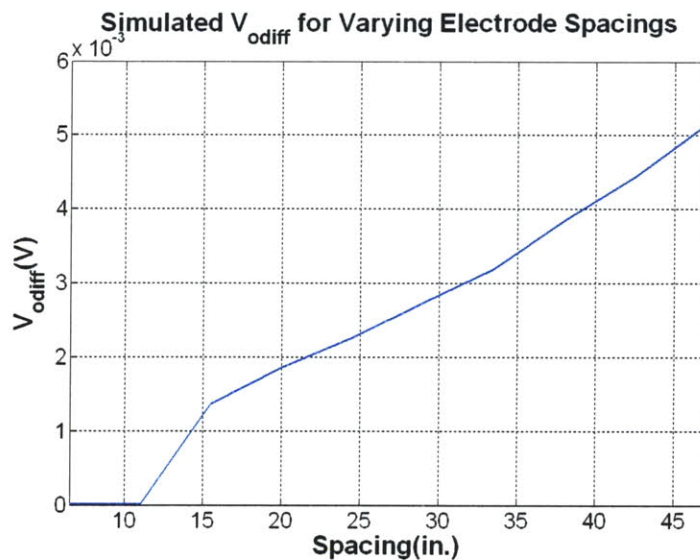


Figure 6-1: A plot of the simulated output voltage for varying electrode spacings.

is varied. Consistent with intuition and with the data collected from the lamp sensor, the

output response decreases as the electrode spacing is decreased. Using this information, we can control the sensing profile of the lamp sensor. The actual sensitivity of the lamp sensor is determined by the SNR of the system for the specific electrode configuration. As shown in table 5.1, the noise floor does not vary dramatically as the spacing is varied in comparison to the decrease in the output response. Therefore, the SNR can be assumed to decrease as the signal level decreases and the output signal magnitude can be taken to represent the detection range. The ability to control the sensing profile could be used to differentiate between conducting objects at varying heights below the lamp and could therefore be used for vertical scanning. In practice, a lamp sensor system could be implemented so that multiple electrode pairs were installed in the lamp as clear Indium Tin-Oxide electrodes inside the cover[4]. Then, the signal conditioning circuitry could take measurements from each of the electrode pairs and use the data to determine characteristics of the target as they vary along the vertical axis.

6.2 A Prototype Mixed-Signal System for Multiple Electrode Pair Measurements

A prototype multiple electrode pair measurement system was built in order to implement a vertical scanning experiment. The connection diagram for the multiple electrode pair system is shown in Figure 6-4. A master PIC16F876 [43] is used to poll four lamp sensor channels, one at a time, for their measured data. Each channel measures its input when it is enabled by the master PIC. The time scale between poling each channel is short enough that the measured data from all of the channels can be considered to be taken simultaneously for this experiment. The master PIC then addresses the Analog MUX so that each channel's data is transferred one at a time to a PC via a serial port connection. The master PIC also opens relays at the inputs to the unused channels while data is being measured on a particular channel. The inputs from the unused channels are disconnected from their amplifiers so that their amplifiers' input characteristics do not influence the measurement of the channel for which data is being taken. The same portA signals that are used to

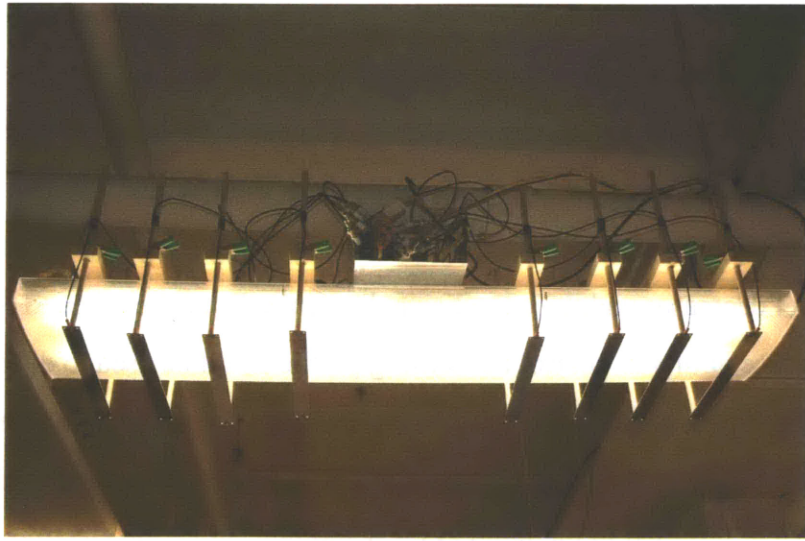


Figure 6-2: A photograph of the multiple electrode system setup.

address the analog MUX, TI part CD4067 [45], for serial data transmission are used to control the relays. Therefore, the MUX switches were chosen so that only one address bit selects each MUX switch (switches 0,1,2, and 4). PortB on the Master PIC is used to enable the ADC measurement on each channel. The particular PortB registers used as slave enable registers were chosen for ease of programming the PIC during debugging.

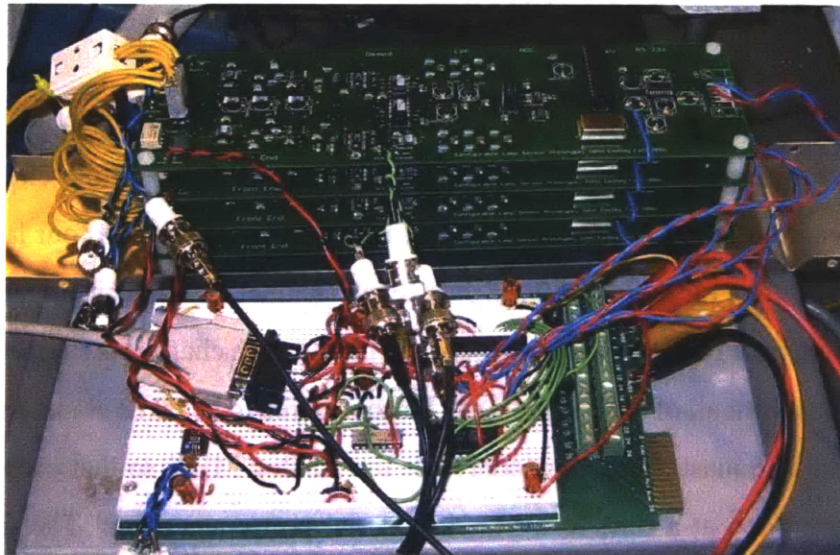


Figure 6-3: A photograph of the multiple electrode pair system electronics.

The serial output data is taken directly from each channel and is selected for output to the PC by the Master PIC with the analog MUX. The serial input data is taken from the

serial driver/receiver, Maxim part MAX232 [44], directly to the master PIC and is used for controlling the mode of operation. The full multiple channel system can be used to scan between the channels or it can be used as the demonstration from Chapter 5 for any of the channels.

A photograph of the electrode setup for the hanging multiple electrode pair system is shown in Figure 6-2 and a photograph of the electronics is shown in Figure 6-3.

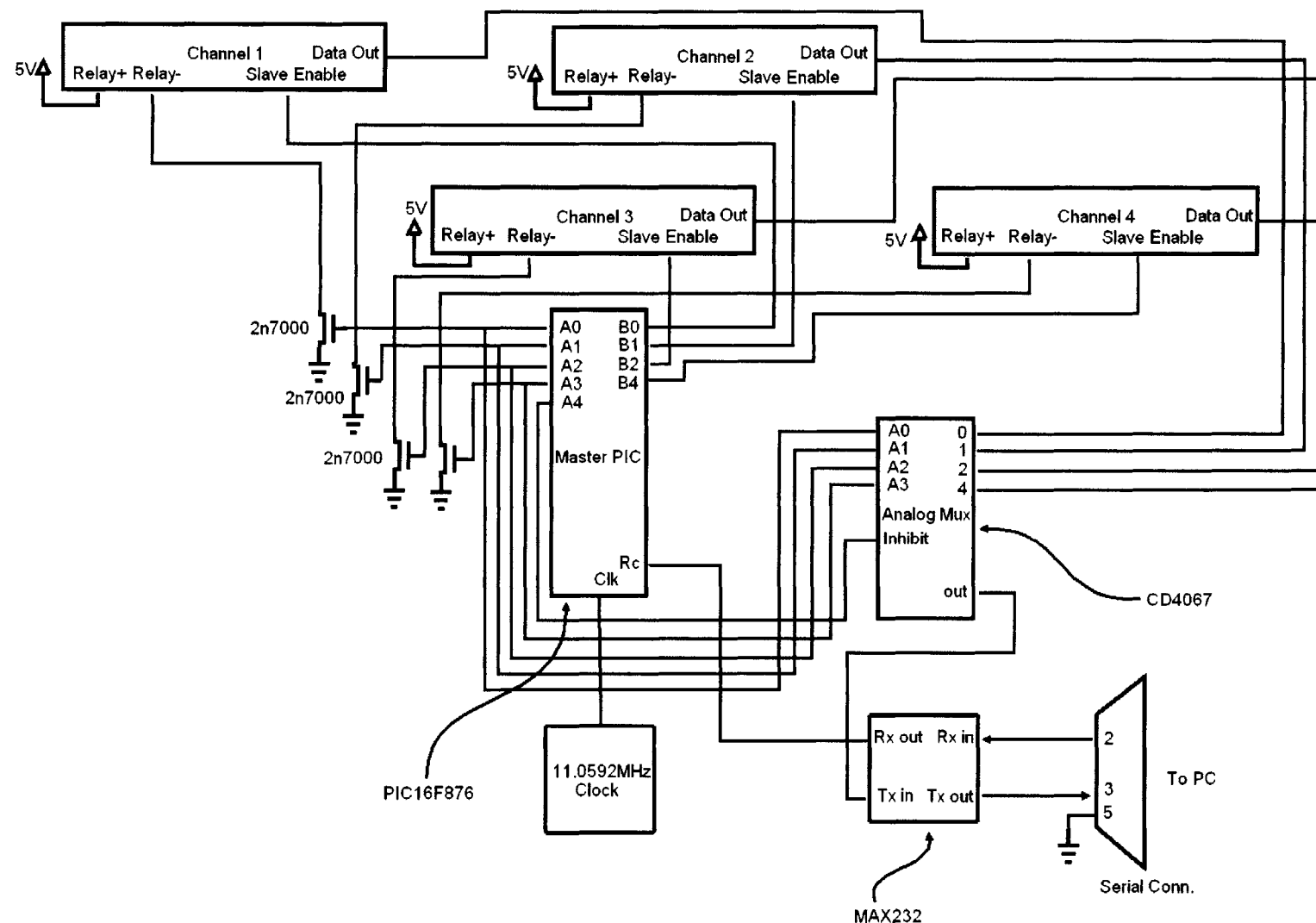


Figure 6-4: The connection diagram for the prototype multiple channel system.

6.2.1 Initial Data and Conclusions

An experiment was performed with the multiple electrode pair system. The goal of the experiment was to determine if the system could detect a change in the human target due to the possession of a conducting (metallic) object.

Four different metallic objects were used. They were a large (30 lbs.) automotive alternator, a small (10 lbs.) automotive alternator, a large hollow metal box, and a small hollow metal box. The experiment was conducted as follows. The target walked below the lamp, stopping at one-foot intervals for each polling of the electrode pairs. The relay switching sound was used to step between pollings. Each pass consisted of twelve one-foot steps each step corresponding to a measurement for each electrode pair. Each data set consisted of five complete passes.

The metric for determining if the metallic object was detected was the rms output voltage of the passing sample for each channel. If the mean rms output voltage of a data set consisting of five passes was different from the mean rms output voltage of the control data set with a confidence level of 97% or better, the data was considered a detection. To be sure, a second control data set was taken after each data set and the first and second control data sets were also compared. The measured data set was only considered valid if the two control data sets were the same with a confidence level of at least 30%. This ensures that the difference between the first control data set and the measured data set was not a result of a slow and uncontrolled change in the output sensitivity of the system.

For each metallic object, data was taken while holding the object at waist, chest and then head levels. For each data set, the control set was taken with the human subject mimicking the body position that he would take on while holding the object. For instance, if the human subject would hold a metallic box at chest level, the control set was taken for the human passing under the lamp with arms bent as if holding a box at chest level. Therefore, control data sets were taken for each body position; for each object. The data was analyzed with a Z-test in MATLAB as described in Chapter 5.

The data are presented in Table 6.1. A low p-value means a low probability that the measured data set and the control data set were the same. Therefore, the lowest p-values

represent the most confident detections. Data sets which correspond to detections based on the 97% detection rule are highlighted. In the table, channel 1 is the widest-spaced electrode set corresponding to the longest detection range and channel 4 is the most closely-spaced electrode pair corresponding to the shortest detection range.

Finally, an overall control data set was taken comparing two data sets in which the human was carrying no metallic object. That data is presented in the last column in the table and shows no significant difference between the two data sets.

Table 6.1: Detection Data p – values for vertical scans of a human walking below the lamp holding various metallic objects.

Position	Channel	Small Metal Box	Small Alternator	Large Metal Box	Large Alternator	Control
head	1	3.01×10^{-23}	4.73×10^{-205}	8.60×10^{-22}	0	0.68
	2	1.22×10^{-6}	2.80×10^{-17}	2.64×10^{-12}	2.30×10^{-129}	0.36
	3	9.30×10^{-11}	3.22×10^{-10}	3.59×10^{-28}	5.70×10^{-130}	0.46
	4	3.47×10^{-11}	2.32×10^{-44}	5.47×10^{-35}	0	0.73
chest	1	0.55	1.21×10^{-10}	1.31×10^{-7}	0.15	"
	2	0.84	3.81×10^{-25}	9.78×10^{-5}	0.15	"
	3	0.42	0.0013	0.0087	0.076	"
	4	0.12	0.032	1.86×10^{-4}	0.027	"
waist	1	0.087	0.0010	0.88	4.55×10^{-5}	"
	2	0.48	2.28×10^{-7}	0.35	1.93×10^{-12}	"
	3	0.33	0.0032	0.57	3.41×10^{-10}	"
	4	0.93	0.032	0.51	5.43×10^{-4}	"

The data show clear detections for each of the metallic objects at some heights. Therefore, as a proof of concept, the lamp sensor system was shown to be potentially useful as a metal detector. Consistent with intuition, the larger the object and the closer to the lamp, the more likely it was to be detected on the human subject.

More interestingly, for some objects, only certain electrode configurations showed confident detections. For the small alternator, only the widest channels detected the object at waist and chest level. This follows the intuition that controlling the sensitivity of the lamp sensor can distinguish between different heights below the lamp. With the objects at the further ranges, only the electrode pairs with the highest sensitivities detected the object.

The large alternator data is also interesting. It shows that the vertical scanning may be selectively sensitive to certain objects at detection ranges bounding a range at which it is not detected or a range in which only one electrode pair detects the object. The data for the chest level large alternator was re-taken to be sure. With each iteration, it showed the same result depicted in the table. Therefore, it can be concluded that something particular to the

large solid metallic object makes it less detectable at chest level.

Potential applications of a vertically scanning, low-cost, discrete and widespread threat detector are numerous. Any public space or secure building in which security is a priority could make use of such a metal detector. The vertical scanning capability may also be a forerunner to a more complicated tomographic imaging functionality. Research presented on Electrical Capacitance Tomography was presented in Chapter 1. By taking multiple independent measurements of the electric fields distorted by the presence of a conducting or dielectric object below the lamp, it may be possible to construct a dielectric tomographic surface which could reveal anomalies on the target corresponding to metallic objects or even dangerous substances. Such anomalies would be reported as anomalies in the three-dimensional space below the lamp so that the location of that object could be known with some precision.

6.3 Limitations and Further Work

The lamp sensor demonstrated proof of concept for detection of a human target at practical detection ranges. It also demonstrated proof of concept for detection of the possession of conducting objects at specific heights. However, the lamp sensor is far from a robust and practical system for real-world security detection on account of the limitations presented here. Before the system can be used in real-world situations, these limitations need to be remedied.

The primary limitation of the lamp sensor is the significant noise from the signal source both low-frequency and higher frequency. The bulb voltage magnitude varies in time and along the length of the bulb and this appears at the output of the synchronous detector as a differential output voltage. Low-frequency bulb voltage variations can be mistaken as detections or can overwhelm a real detection. Because these variations are stochastic, they vary in magnitude and can at times be insignificant while at other times they can be very significant. The fact that these variations originate as differential-mode or localized bulb voltage variations was verified by replacing the bulbs with fake bulbs constructed of a distributed resistance mimicking the resistance of the real bulb. The fake bulbs were

constructed to have similar conductive surface area to the real bulbs. With the fake bulbs in place, detection ranges and output behavior were comparable to system with the real bulbs, but the output noise floor of the system was consistently $20\mu V_{rms}$. This is a vast improvement over the real system which exhibited noise floors varying unpredictably between $50\mu V_{rms}$ and $150\mu V_{rms}$. Therefore, a solution which reduces the effect of the bulb voltage variations would greatly improve the robustness and usefulness of the lamp sensor. One suggestion that may achieve this is the use of differential-mode feedforward compensation. Because only differential-mode or localized bulb voltage variations will deviate the output significantly, a differential or localized measurement of the effective source coupling to each individual electrode could be used to compensate the source noise. This measurement would need to be insensitive to targets below the lamp and would have to present an accurate representation of the electric flux coupling to each electrode. The output of that measurement could then be used to normalize the differential output voltage of the differential front-end amplifier.

Further work could also use the lamp sensor system as an Electrical Capacitance Tomography (ECT) system already described. This system would need to take multiple independent measurements and then the data would have to be processed so that a map of the electrical permittivity in the space below the lamp could be constructed. The system might make use of multiple electrodes as well as the degrees of freedom added for measurements taken for multiple target positions below the lamp. This would result in a "scan as you walk" function.

Further work might interface multiple lamp sensors to demonstrate a widespread detection system. This would consist of modifying multiple fluorescent lamps in a space and then interfacing them so that they were controlled and monitored remotely.

In order to make the lamp sensor practical, the electrodes can not be visible on the outside of the lamp like they are in this work. Therefore, further work could be done to inexpensively implant transparent Indium-Tin Oxide electrodes on the inside of the lamp cover[4].

At present, the output voltage of the lamp sensor is nulled or zeroed by hand. A system which auto-nulled the output could be developed perhaps by taking contributions of

measurements from thinner length-wise distributed electrodes in front of the lamp.

6.3.1 Possible Immediate Improvements

Some specific design areas which warrant further investigation have been revealed in writing this work and make possible some immediate improvements.

First, the common-mode output voltage setting of the front-end amplifier is not accurately 2.5V (it is closer to 2.2V) due to the relatively small default setting resistors internal to the amplifier. The V_{OCM} pin on the differential amplifier needs to be driven with a low impedance source such as a precision op-amp voltage buffer or the internal resistors need to be taken into account when choosing the external resistor values.

It has been verified previously that the common-mode input voltage ranges are not exceeded at least for some electrode configurations by taking two simultaneous measurements from ground to the input terminals and averaging the two on the oscilloscope. However, the common-mode input voltage levels should be reexamined to confirm that they are not exceeding the specified limits of the parts in the front-end amplifier for all electrode configurations. If they are in fact exceeding the common-mode input range on occasion or consistently, that would contribute to the noise at the output and it could explain some unpredictability in the noise floor with the lamp turned on. The common-mode input voltage levels will vary with the electrode configuration, so it may be the case that for some electrode configurations, the maximum common-mode input levels are exceeded and for other electrode configurations, they are not.

The differential amplifier part THS4140 is rated for +/-12V supply voltage capability. However, due to the 15mA of quiescent current, this results in 33mW of steady state power dissipation. Because the part is packaged in a small SOIC package with no heat sink, the part routinely overheats. The part could be replaced with a higher performance part that consumes less quiescent current. Also, the +/-12V supply voltages are not necessary for the differential-mode dynamic range of the signal conditioning circuitry. Consequently, the supply voltages could be reduced. The Analog Devices part AD8132 could be used with a +/-5V supply and it could replace the current differential amplifier and is pin compatible.

However, before reducing the supply voltages, it must be verified that +/-12V supplies are not necessary for common-mode input voltage levels in the presence of the lamp[47]. Alternatively, if the +/-12V rails are in fact necessary, the TI part is available in a package that provides an exposed thermal pad on the underside. Contacting the thermal pad to an exposed conducting plane would provide good heat sinking.

The differential low-pass filter was designed to meet the low-input resistance constraint for the ADC. Consequently, the filter presents a low-impedance load to the output of the front-end amplifier and this is not ideal. A better solution would be to design the filter to not load the output of the front-end and then buffer it with a high-performance low offset and low drift fully-differential amplifier, before connecting to the input of the ADC.

A re-examination of the closed-loop frequency responses of the front-end amplifier and of the clock amplifier might reveal that the clock amplifier introduces phase error due to its compensation network. Reducing the phase error to zero could improve the sensitivity of the lamp sensor.

Finally, if further work is done on the multiple electrode pair system, there is no need to use an entire lamp sensor channel for each pair. The electrode pairs could be switched onto the input of a single lamp sensor channel and this would simplify maintenance and debugging of the electronics. If simultaneous measurements of multiple electrode pairs are desired, then multiple channels are necessary. In the case of simultaneous measurements, the effect of the presence each amplifier and electrode pair on the other electrode pair measurements must be understood and quantified.

Appendix A

Lamp Sensor Application Notes

A.1 Nulling the Output

The base-band differential output voltage of the lamp sensor should be relatively near 0 V in the absence of a detection. In practice, nulling the output voltage is achieved by watching the output of the system in the real-time MATLAB demonstration and manually adjusting the relative depths of the two electrodes being nulled.

-First choose a range of voltages in which the output voltage is considered relatively near 0 V. For a maximum deviation of +/-2.5V, a +/-1mV range is acceptable.

-Next, fix one of the two electrodes so that its depth from the lamp is approximately the desired electrode depth. Make sure that the two electrodes are spaced lengthwise symmetrically about the center of the lamp.

-Finally, manually adjust the depth of the unfixed electrode while watching the output voltage approach 0 V. Sufficient control of the output voltage for nulling is usually possible by adjusting the unfixed electrode depth by hand.

A.2 Practical Considerations for a Predictable Output

In order to repeat the results in this work, the output of the lamp sensor must be quiet and stable. That means that it should not be overwhelmed by uncontrolled interference or noise. Some practical considerations are necessary in order to achieve good output performance.

-In Section 3.1.2, it was shown that the common-mode rejection ration of the system degrades as the electrodes are further out of the nulled position. Therefore, good CMRR will be achieved only when the measurement electrodes are nulled. Significant improvement in the predictability of the output can be observed by nulling the electrodes.

-The standard fluorescent lamp cover provides protection from uncontrolled air movement at the surface of the bulbs. By establishing a still-air environment around the bulbs, we can eliminate differential-mode modulations in the flux signal due to ambient air currents and therefore eliminate some uncontrolled output behavior. Significant improvement in the output performance can be observed by placing the standard cover on the lamp especially in the presence of blowing HVAC ventilation or stirred air from movement of a long-past target passing by the lamp sensor.

-The metallic piece which covers the ballast and the ballast wires and which physically contacts the backplane of the lamp provides shielding from electric coupling from the ballast and ballast wires to the electronic circuitry and to the electrodes. Some improvement in the output performance can be obtained by placing the standard ballast cover over the ballast and wires.

-The lamp sensor electronics should be shielded in a grounded metallic box in order to reduce electric coupling from ambient and unwanted signal sources. The grounded coaxial shields on the wires that connect the electrodes to the circuitry provide shielding in the space outside of the box.

-Some drift is observed in the output when initially turning on the lamp sensor. It is hypothesized that localized or differential-mode drift of the ac bulb surface potential magnitudes occurs as the bulbs approach thermal equilibrium with the surrounding air. Therefore, a drifting startup transient in the output voltage can be observed that lasts as long as 10 minutes. The hypothesis that the bulbs exhibit differential-mode surface potential variation as they approach thermal equilibrium with the surrounding air would suggest that placing the lamp cover over the bulbs would also result in a drifting transient and this is in fact the case. A drifting transient is observed when placing or removing the lamp cover and this can also last as long as 10 minutes. The output voltage should be re-nulled after the output voltage stops drifting.

-Poor output noise performance is also observed when the differential amplifier part THS4140 in the front-end amplifier has been damaged either by over-voltage or by static discharge. Typically, the output noise performance will degrade over a period of 10's of minutes to a few hours if the THS4140 has been damaged. The output noise performance will degrade without changing the lamp sensor configuration and the power consumption will slowly increase. Replacing the THS4140 will correct this particular problem. No other part in the lamp sensor has been shown to consistently fail and result in poor output noise performance.

Appendix B

Software

B.1 MATLAB Code

B.1.1 takedata.m

```
1 %Takedata.m is a script which takes a sample from the lamp sensor that is "points" data
  points long.
%This script requires GetSerialData.mex and plotADC.m
%To get the mex file, Compile GetSerialData.c with >>mex GetSerialData.c
%and make sure that StdAfx.h is in the directory.

6 Fig = figure(2);
           %If Roll=1,Do Roll Mode
format short
printbuf = ([]);      %Initialize the prinbuffer to zeros.

11 i=0
while(i<points)
  clear datapoint

  datapoint = ((GetSerialDatasingle('COM5', 115200, 1))*(ref/16777215));
16 printbuf = horzcat(printbuf, datapoint);
  i=i+1
end
printbuf = printbuf(10:length(printbuf));
plot(printbuf)
21 Total_Dev_uV = (max(printbuf)-min(printbuf))/(1e-6)
```

B.1.2 postprocess.m

```
%postprocess.m is a script which analyzes a data sample from takedata.m. This version
plots the data sample and calculates the acrms voltage of the data sample. It
concatenates the acrms value onto a vector named v so that an ensemble of data samples
can be analyzed. Therefore it requires v to be cleared and defined before using the
script. The script clearv.m takes care of initializing the vector v.
format short

4 %Fig = figure(2);
points = length(databuf);
plot(databuf)
%Total_Dev_uV = (max(databuf)-min(databuf))/(1e-6)
AVG = sum(databuf)/(points);
9 Vacrms_uV = (((1/points)*sum((databuf-AVG).* (databuf-AVG)))^0.5)/(1e-6)

v = horzcat(v,Vacrms_uV)
```

B.1.3 clearv.m

```
%clearv.m initializes the vector v for postprocess.m
v = ([]);
```

B.1.4 PlotADCroll.m

```
%PlotADCroll reads serial data from the lamp sensor and plots it in a plot window as shown
in the real-time MATLAB demo section. It is called from the script demo.m.
3 collected = [];
matrix = [];

for i=1:4 %Collect 4 bytes from the ADC
    collected = (fscanf(s,'%x'));
8 matrix = horzcat(matrix, collected);
end

% fprintf(s,'%c',' '); %Tell the Master PIC I got the data

13 %Translate the 4 data bytes into a signed integer
MSB = (2^16)*matrix(1);NSB = (2^8)*matrix(2);LSB = matrix(3);SIGN = matrix(4);

if SIGN==0
```

```

    datapoint = -(16777215-(MSB+NSB+LSB));
18 else
    datapoint = MSB+NSB+LSB;
end
%Output datapoint has units Volts
datapoint = ref*datapoint/16777215;
23 printbuf = horzcat(printbuf(2:points), datapoint);
fixedscale = 2*ref*1e-2;      %Set up the fixed scale window
    subplot(3,1,2)          %for the middle plot

    plot(printbuf, 'Linewidth', 1)
28 axis ([1 points -fixedscale fixedscale ]);
    ylabel('Volts')

    subplot(3,1,1)          %This window will auto scale unless the deviations
33
    %are less than some value "minscale"

    %Decide if there is an event going on or not
format short
38 VRANGE = (max(printbuf)-min(printbuf)), ;
AVG = sum(printbuf)/(points);
Vacrms_uV = (((1/points)*sum((printbuf-AVG).*(printbuf-AVG)))^0.5)/(1e-6)
%Dev_uV = VRANGE*ref/(1e-6) %Print out Absolute Voltage Variation in the Current
    Window
if VRANGE<minscale    %If there is no event, zoom in to the minimum scale
    plot(printbuf, 'Linewidth', 1)
    axis([1 points (min(printbuf) - minscale) (max(printbuf) + minscale)]);
    ylabel('Volts')
    STATUS = 'Quiet...shhhhhh'
    if length(event)<6           %%Event display starts here:
        %If the window is not auto scaled
        event = ([]);            %assume the event is over and print it.
        ;                         %But if it's too short don't actually print it (goto
        end)
48
else
    %If there has been an event thats long enough then
    plot it

    subplot(3,1,3)          %In the bottom plot

    length_event = length(event);      %Get some values to help plot it in a cool
    way.

```

```

58     event_left = event(1:floor(0.5*length_event));      %These 4 values are for
          the direction detection
    avg_event_left = (sum(event_left))/length(event_left);
    event_right = event(ceil(0.5*length_event):length_event);
    avg_event_right = (sum(event_right))/length(event_right);
    bookend_length = floor(0.3*length_event);           %Make a bookend for the
          plot so it looks better
63     avgevent = (sum(event(1:length_event)))/(length_event);
    event = horzcat((ones(1,bookend_length)).*avgevent, event,(ones(1,
          bookend_length)).*avgevent); %Glue the bookends onto the event
    plot(event, 'r', 'linewidth', 1)          %plot the whole event in red in the
          last window
    if avg_event_left < avg_event_right,
        LAST_EVENT = 'Left_to_Right'    %Playing with event detection bells
68    else
        LAST_EVENT = 'Right_to_Left'    %and whistles
    end
    axis auto;                  %Auto scale the event window
    ylabel('Volts')
73    event = ([]);            %reset the event vector
    end                         %%Event display ends here
else
    plot(printbuf, 'linewidth', 1)
    axis auto;
    ylabel('Volts')
78    event = horzcat(event(1:(length(event))), datapoint);    %And collect the event
          data points
    STATUS = 'Event'                                %Also print 'Event'
                                                    %%Event collection:
    end
83 drawnow

```

B.1.5 Demo.m

```

function y = demo(ref, points, channel)
2 clear figure
if (nargin ~=3)
    disp('Usage: demo(reference_voltage,points_per_frame,channel)')
else
7 figure(2);
format long;
printbuf = zeros(1,points);    %Initialize the prinbuffer to zeros.
event = ([]);                %Initialize the event buffer

```

```

1 STATUS = 0;LAST_EVENT = 0;           %Some variables
12 calibrate = ([]);                  %Autocalibrate the output plot scale
 collected = [];
 matrix = [];
 ports=instrfind;
 if size(ports ,1) > 0
    stopasync(instrfind);
    fclose(instrfind);
    delete(instrfind);
end
s=serial('COM5', 'BaudRate', 115200, 'DataBits', 8, 'Parity', 'none', 'StopBits', 1, 'terminator', 'LF'); % create a serial port object
22 fopen(s); %Open serial port defined above
if channel == 1
gomaster = 'A';
elseif channel == 2
    gomaster = 'D';
27 elseif channel ==3
    gomaster = 'E';
elseif channel ==4;
    gomaster = 'F';
end
32 stopmaster = 'B';
event = ([]);                      %Initialize the event buffer
STATUS = 0;LAST_EVENT = 0;           %Some variables
calibrate = ([]);                  %Autocalibrate the output plot scale

37 fprintf(s,'%c',gomaster);        %Tell Master PIC to go
while(length(calibrate))<(ceil(1.1*points))
    collected = [];
    matrix = [];
    for i=1:4                      %Collect 4 bytes from the ADC
42    collected = (fscanf(s,'%x'));
        matrix = horzcat(matrix , collected);
    end
    MSB = (2^16)*matrix(1);NSB = (2^8)*matrix(2);LSB = matrix(3);SIGN = matrix(4);
    if SIGN==0
47    datapoint = -(16777215-(MSB+NSB+LSB));
    else
        datapoint = MSB+NSB+LSB;
    end
    calibrate = horzcat(calibrate , datapoint*(1/16777215));
52    STATUS = 'Calibrating'
end
calibrate = calibrate(2:length(calibrate));

```

```

minscale = 1.8*(max(calibrate)-min(calibrate))*ref;

57 while(1)
    if strcmp(get(2,'currentcharacter'),'q') %Stop the loop if you press q
        close(2)
        fprintf(s,'%c',stopmaster);      %Disable the Slave
        stopasync(s);
    62     fclose(s);
        delete(s);
        clear s;
        break
    end
    plotADCrroll           %This is a big script file PlotADCrroll.m
end
% Close and wrap up the serial port

```

B.1.6 Compensation2.m

```

%Compensation2 produces overlayed bode plots of the closed-loop frequency response of the
%front-end amplifier for various feedback compensation capacitances.
s = tf('s');
A = 2238.7/(1+s/(2*pi*67e3));
Ci = 1e-12;
5 Zi = 1/(s*Ci);
Cg = 31.1e-12;

hold off
Rf = 1e6;
10 Cf = 0;
Zf = Rf/(s*Rf*Cf+1);
H = A*Zf/(Zf+Zi*(1+A));
bode(H)
hold on
15 Cf = 1.1e-12;
Zf = Rf/(s*Rf*Cf+1);
H = A*Zf/(Zf+Zi*(1+A));
bode(H)
Cf = 2.2e-12;
20 Zf = Rf/(s*Rf*Cf+1);
H = A*Zf/(Zf+Zi*(1+A));
bode(H)
Cf = 5e-12;
Zf = Rf/(s*Rf*Cf+1);

```

```

25 H = A*Zf/(Zf+Zi*(1+A));
bode(H)
Cf = 10e-12;
Zf = Rf/(s*Rf*Cf+1);
H = A*Zf/(Zf+Zi*(1+A));
30 bode(H)
Cf = 15e-12;
Zf = Rf/(s*Rf*Cf+1);
H = A*Zf/(Zf+Zi*(1+A));
bode(H)
35 Cf = 20e-12;
Zf = Rf/(s*Rf*Cf+1);
H = A*Zf/(Zf+Zi*(1+A));
bode(H)
Cf = 30e-12;
40 Zf = Rf/(s*Rf*Cf+1);
H = A*Zf/(Zf+Zi*(1+A));
bode(H)
Cf = 62.2e-12;
Zf = Rf/(s*Rf*Cf+1);
45 H = A*Zf/(Zf+Zi*(1+A));
bode(H);

```

B.1.7 Syncdet.m

```

%Syncdet.m plots the output response of a synchronous detection system as the phase error
is varied.
2 phi = [1:1000];
phi = phi./1000;
phi = phi.*0.5*pi;
V = [];
omegact = 0;
7 fontsize1 = 16;
fontsize2 = 14;
fontweight = 'bold';
V = cos(omegact).*cos(omegact+phi);
plot(phi,V,'linewidth',2)
12 set(gca,'XTick',0:pi/8:pi/2)
set(gca,'XTickLabel',{'0','pi/8','pi/4','3pi/8','pi/2'})
set(gca,'fontsize',fontsize2)
title('Normalized_Output_Response_of_a_Synchronous_Detector_vs_Phase_Error','fontsize',
      fontsize1,'fontweight',fontweight)
xlabel('Phase_Error_(radians)','fontsize',fontsize1,'fontweight',fontweight)

```

```

17 ylabel('Normalized_Output_Response_Magnitude','fontsize',fontsize1,'fontweight',fontweight
)

```

B.1.8 anacap5.m

```

%anacap5.m reads a text file that lists capacitance matrices from Fastcap and extracts
vectors of capacitances of interest in the system.
fid = fopen(filename); %open the data file
3 array = []; %init the result array

while ~feof(fid) %Go through the file and get each matrix
str = fgetl(fid);
units = regexp(str,'femto'); %Check to see the units of the matrix femto pico
8 if ~isempty(units)
    units = regexp(str,'pico');
    if ~isempty(units)
        scale = 10^-12;
    end
13 scale = 10^-15;
else
    scale = 10^-18;
end
trash = fgetl(fid); %Get rid of the headers
18 i = 1;
while i < 7 %put each line into a 6x6 matrix
    line = fgetl(fid);
    matrix(i,:) = sscanf(line,'%*s %*d %f %f %f %f %f');
    i = i+1;
end
matrix = matrix*scale; %Scale by the units
array = horzcat(array, matrix); %concatenate onto the result array and go to the next
                                matrix
end
%array = array/(1e-12); %normalize by picofarads
28 array = abs(array);

C11 = [];
C22 = [];
C1T = [];
33 C2T = [];
Cp1 = [];
Cp2 = [];

C1Tp = [];

```

```

38 C2Tp = [];

j = 1;
k = 0;

43 [M,N] = size(array);
while (k+6) <= N

% C11 = horzcat(C11, array(1,3+k));
% C22 = horzcat(C22, array(2,4+k));
48 C11 = horzcat(C11, 2e-12);
C22 = horzcat(C22, 2e-12);
C1T = horzcat(C1T, array(1,5+k));
C2T = horzcat(C2T, array(2,5+k));
Cp1 = horzcat(Cp1, 21e-12);

53 Cp2 = horzcat(Cp2, 21e-12);
% Cp1 = horzcat(Cp1, array(1,6+k));
% Cp2 = horzcat(Cp2, array(2,6+k));

j=j+1;
58 k = 6*(j-1);
end

C1Tp = C1T+Cp1;
C2Tp = C2T+Cp2;

63 % figure(1)
% plot(C11)
% title('Bulb1 to elec1')
% ylabel('farads')

68 % figure(2)
% plot(C22)
% title('Bulb2 to elec2')
% ylabel('farads')

% figure(3)
73 % plot(C1T)
% title('Bulb1 to target')
% ylabel('farads')

% figure(4)
% plot(C2T)
% title('Bulb2 to target')
% ylabel('farads')

78 % figure(5)
% plot(Cp1)
% title('Bulb1 to back')

```

```

83 % ylabel('farads')
% figure(6)
% plot(Cp2)
% title('Bulb2 to back')
% ylabel('farads')
88 fclose(fid);

```

B.1.9 datatest.m

```

%datatest.m was used to test data taken from the multiple electrode pair system with a
% MATLAB Z-test.
2 load control.mat
load data.mat
format short

7 control1 = control(1,:);
control2 = control(2,:);
control3 = control(3,:);
control4 = control(4,:);
data1 = data(1,:);
12 data2 = data(2,:);
data3 = data(3,:);
data4 = data(4,:);

17 i=1;
h=[];

controllength=length(control1);
datalength = length(data1);
controlmean1 = sum(control1)/controllength;
22 while i-l<controllength ,
    h=horzcat(h, control1(i)-controlmean1);
    i=i+1;
end
g=h.*h;
27 controlvar1=sum(g)/length(g);
controlstdev1=sqrt(controlvar1);

[H1,P1]=ztest(data1,controlmean1,controlstdev1);
P1
32 i=1;
h=[];

```

```

controlmean2 = sum(control2)/controllength;
while i-l<controllength ,
37    h=horzcat(h, control2(i)-controlmean2);
    i=i+1;
end
g=h.*h;
controlvar2=sum(g)/length(g);
42 controlstdev2=sqrt(controlvar2);

[H2,P2]=ztest(data2,controlmean2,controlstdev2);
P2

47 i=1;
h=[];
controlmean3 = sum(control3)/controllength;
while i-l<controllength ,
    h=horzcat(h, control3(i)-controlmean3);
52    i=i+1;
end
g=h.*h;
controlvar3=sum(g)/length(g);
controlstdev3=sqrt(controlvar3);

57 [H3,P3]=ztest(data3,controlmean3,controlstdev3);
P3

i=1;
62 h=[];
controlmean4 = sum(control4)/controllength;
while i-l<controllength ,
    h=horzcat(h, control4(i)-controlmean4);
    i=i+1;
67 end
g=h.*h;
controlvar4=sum(g)/length(g);
controlstdev4=sqrt(controlvar4);

72 [H4,P4]=ztest(data4,controlmean4,controlstdev4);
P4

```

B.1.10 openloopcomp.m

```

s = tf('s');
2 A = 2238.7/(1+s/(2*pi*67e3));

```

```

R = 1e6;
Cf = 1e-12;
C1 = 1e-12;
C2 = 31e-12;
7 Cin = C1+C2;
Z1 = 1/(s*Cin);
Zf = R/(1+R*s*Cf);

H = A*(1+R*Cf*s)/(1+R*Cf*s+R*Cin*s);
12 L = A*Z1/(Zf+Z1);
figure(1)
margin(L)
figure(2)
pzmap(L)

```

B.1.11 idiffthesis.m

```

%idiffwork.m calls anacap5.m and uses the extracted capacitances to plot the simulated
    differential output voltage as the target varies its position below the lamp sensor.
clear all
points = 33;
4 filename = 'capdataworkvert1.m';anacap5;points = points+1;
R = 1e6;
w=2*pi*42e3;
eps = 8.85e-12;

9 phi = 1;      %electric flux magnitude matched empirically

%Make a matrix eqn for each time step
Vdiff = [];
i = 1;
14 while(i<points),

i1 = (C11(i))./(C1Tp(i)+C11(i));
i2 = (C22(i))./(C2Tp(i)+C22(i));

19 idiff = eps*w*phi*(i1-i2);
fontsize1 = 20;
fontsize2 = 18;
fontweight1 = 'bold';
24 fontweight2 = 'normal';
linewidth = 2;

```

```

29 Vdiff = horzcat(Vdiff,R*iidiff)
i=i+1;
end
figure(20)
vdiff = Vdiff
n = [0:32];
n=n*.4;
n=n-6;
plot(n,vdiff,'linewidth', linewidth)
title('V_{odiff} normalized by |\Phi_o| vs. Time','fontsize',fontsize1,'fontweight',
      fontweight1)
ylabel('V_{odiff}/|\Phi_o|','fontsize',fontsize1,'fontweight',fontweight1)
xlabel('Distance from Left End of Lamp(m)','fontsize',fontsize1,'fontweight',fontweight1)
set(gca,'fontsize',fontsize2,'fontweight',fontweight2)
39

```

B.1.12 datatest.m

```

1 %Data test compares an ensemble of data samples to an ensemble of control samples and
   produces a confidence level that the data samples are equivalent to the control
   samples.
test
v=control

6 i=1;
h=();
n=length(v);
controlmean = sum(v)/length(v)
while i+1<length(v),
11     h=horzcat(h, v(i)-controlmean);
     i=i+1;
end
g=h.*h;
controlvar=sum(g)/length(g)
controlstdev=sqrt(controlvar)

16 [H,P]=ztest(test ,controlmean ,controlstdev)

```

B.1.13 scandata.m

```

1 %Scandata was used in the multiple electrode pair system experiment to take scanning data
   as the human target walked below the lamp with a metallic object.

```

```

ref = 5;
delay = 3;

repeat = points+delay;
6 scan

printbuf1 = printbuf1(delay+1:length(printbuf1));
printbuf2 = printbuf2(delay+1:length(printbuf2));
printbuf3 = printbuf3(delay+1:length(printbuf3));
11 printbuf4 = printbuf4(delay+1:length(printbuf4));
AVG1 = sum(printbuf1)/(points);
Vacrms_uV1 = (((1/points)*sum((printbuf1-AVG1).*(printbuf1-AVG1)))^0.5)/(1e-6);

AVG2 = sum(printbuf2)/(points);
16 Vacrms_uV2 = (((1/points)*sum((printbuf2-AVG2).*(printbuf2-AVG2)))^0.5)/(1e-6);

AVG3 = sum(printbuf3)/(points);
Vacrms_uV3 = (((1/points)*sum((printbuf3-AVG3).*(printbuf3-AVG3)))^0.5)/(1e-6);

21 AVG4 = sum(printbuf4)/(points);
Vacrms_uV4 = (((1/points)*sum((printbuf4-AVG4).*(printbuf4-AVG4)))^0.5)/(1e-6);

Vacrms_uV1;
26 Vacrms_uV2;
Vacrms_uV3;
Vacrms_uV4;

31 ensemble1 = horzcat(ensemble1,Vacrms_uV1)
ensemble2 = horzcat(ensemble2,Vacrms_uV2)
ensemble3 = horzcat(ensemble3,Vacrms_uV3)
ensemble4 = horzcat(ensemble4,Vacrms_uV4)

```

B.1.14 clearens.m

```

1 ensemble1 = [];
ensemble2 = [];
ensemble3 = [];
ensemble4 = [];

```

B.1.15 storecontrol.m

```

1 control1 = [];
control2 = [];
control3 = [];
control4 = [];
control1 = ensemble1;
6 control2 = ensemble2;
control3 = ensemble3;
control4 = ensemble4;
control = vertcat(control1,control2,control3, control4);

11 clearans;

```

B.1.16 storedata.m

```

data1 = [];
data2 = [];
data3 = [];
4 data4 = [];

data1 = ensemble1;
data2 = ensemble2;
data3 = ensemble3;
9 data4 = ensemble4;
data = vertcat(data1,data2,data3,data4);
clearans;

```

B.2 C Code for the PIC

B.2.1 adc.c

```

//adc.c programs a single PIC16F876 for the single channel lamp sensor so that it //
interfaces with demo.m in MATLAB
#include <pic.h>

4 //Make sure to change pcc.bat to reflect the correct PIC or you will
//have problems up here!

//Program as regular 8 bit hex or Intel

```

```

9  __CONFIG(0x3F72);           //No code prot., no debugger, FLASH prog. memory write
   enabled
   //no LVP, yes Brown Out Reset, no Watchdog, yes Power up
   timer
   //High Speed Oscillator

14  unsigned char MMSB;
  unsigned char NNSB;
  unsigned char LLSB;
  unsigned char JJSB;
  unsigned char MSB;
  unsigned char NSB;
19  unsigned char LSB;
  unsigned char SIGN;
  int newlinecount;

void ReadADC(void);
24 void WriteUART(unsigned char);
void WriteHex(unsigned char);
void getdatabytes(void);
void transmit(void);
void ftransmit(void);

29 void Linit(void) {      //Linit just initializes everything and chooses
   //all of the appropriate options in the mess of
   //Special Registers.

34  TRISB = 0x82;    //Use Port B to control and pole ADC,
   //ADC Busy -> RBI

   //Configure SPI
TRISC = 0xD0;    //Configure port C: Rx and Tx set (UART);
39   //SDO Output; SDI configured by control reg
   //as input;
   //SCK output (Master); RC<2:0> don't care.

SSPCON = 0x20;  //Configure Synchronous Serial Port Control Register:
44   //SSPCON<7:6> don't care;
   //Enable Serial Port mode for SCK, SDO, SDI (and SS);
   //Idle State for clock is Low;
   //SPI Master Mode, clock = Fosc/4.

49  SSPSTAT = 0x40; //Configure Synchronous Serial Port Status Register:
   //SMP Sample at middle of data output time
   //Data transmit on rising edge of SCK.

```

```

//SSPSTAT<5:0> don't care.

54          // Configure UART
RCSTA = 0x80;    // Set bit SPEN to configure RX and TX as UART pins.
                  //RCSTA<6:0> don't care.

TXSTA = 0x24;    // Configure Transmit register:
                  // Bit 7 don't care (Async); 8-bit transmission;
                  // Transmit enabled; Asynchronous Mode; bit 3 unimp.
                  // High Baud Rate; TXSTA<1:0> don't care.

SPBRG = 5;        // Baud Rate Generator Value = 5 for 115.2 kbps
                  // with (11.0592MHz Clock).

64
}

void main(void) {
    Linit();           // Initialize PIC and ADC

    newlinecount = 0;
    while(1){          // Stay in here forever
        while (RBI == 1)      // Wait until ADC is done conversion
            continue;
        ReadADC();           // Get the conversion result
        getdatabytes(); // Isolate 24 data bits out of 32

79        ftransmit();           // Send the result to serial port

    }
}

84 ///////////////////////////////////////////////////////////////////
//subroutines
/////////////////////////////////////////////////////////////////

void transmit(void) {           // Transmit MSB, then NSB, then LSB
    //Play with delimiting characters here
    WriteUART(MSB);
    WriteUART(NSB);
    WriteUART(LSB);
    WriteUART(SIGN);
    WriteUART(0);           // Delimit with a zero.

94    // WriteHex(MSB);
}

```

```

        //WriteHex(NSB);
        //WriteHex(LSB);

99    }

void ftransmit(void) {           //Transmit MSB, then NSB, then LSB
                           //Play with delimiting characters here
    WriteHex(MSB);
104   WriteUART('\n');
    WriteHex(NSB);
    WriteUART('\n');
    WriteHex(LSB);
    WriteUART('\n');
109   WriteHex(SIGN);
    WriteUART('\n');           //Delimit with a zero.

                           //WriteHex(MSB);
                           //WriteHex(NSB);
114   //WriteHex(LSB);
}

///////////

void ReadADC(void) {
119   int SampRateByte = 0x78; //This is the value we will write to SSPBUF to initiate
                           //transmission and also to send to the SDI pin on
                           //the ADC
                           //in order to program the sampling rate as follows
                           :
                           //0x08 = 3.52kHz, 0x10 = 1.76kHz, 0x00 = 880Hz, 0
                           x18 = 880Hz
                           //0x20 = 440Hz, 0x28 = 220Hz, 0x30 = 110Hz, 0x38 =
                           55Hz
                           //0x40 = 27.5Hz, 0x48 = 13.75Hz, 0x78 = 6.875Hz

124   SSPBUF = SampRateByte; //Write to SSPBUF to initiate transmission.
                           //The Value written to SSPBUF outputs to the ADC's
                           SDI pin
                           //and programs the sample rate.
                           //SCK is output to ADC

while (STAT_BF == 0)      //Wait till Buffer is full
    continue;

129   MMSB = SSPBUF;          //8 of 32 in MSB

```

```

    SSPBUF = SampRateByte;           //next byte
    while (STAT_BF == 0)
        continue;
139     NNSB = SSPBUF;           //9-16 in NSB

    SSPBUF = SampRateByte;           //next byte
144     while (STAT_BF == 0)
        continue;
    LLSB = SSPBUF;           //17-24 in LSB

149     SSPBUF = SampRateByte;           //Let the ADC finish so it can
     while (STAT_BF == 0)      //start the next cycle.
        continue;
    JJSB = SSPBUF;

154     //I leave it as an exercise to the reader to
     //figure out why
    SSPBUF = SampRateByte;           //I needed this extra one in order to
    while (STAT_BF == 0)      //get it working.
        continue;
}
159     //back to main with MMSB, NNSB and LLSB

//////////////

const char hexlookup[] = "0123456789ABCDEF";      //Array for bin to hex conversion

164 void WriteHex(unsigned char x)                  //Convert from bin to hex and write
{
    WriteUART(hexlookup[x >> 4]);
    WriteUART(hexlookup[x & 0x0f]);
}
169 //////////////

void WriteUART(unsigned char transmitchar) { //Just write to the UART.
    while (!TXIF)                         //Wait until last transmit is done
        continue;
174     TXREG = transmitchar;             //Write to TXREG which initiates
}
179     //transmission

//////////////

```

```

void getdatabytes(void) { //Get 24 data bits amongst the 32 transmitted bits
    :
    MSB = (((MMSB << 3) & 0b11111000) + ((NNSB >> 5) & 0b00000111));
    NSB = (((NNSB << 3) & 0b11111000) + ((LLSB >> 5) & 0b00000111));
    LSB = (((LLSB << 3) & 0b11111000) + ((JJSB >> 5) & 0b00000111));
184   SIGN = ((MMSB >> 5) & 0b00000001);
}

```

B.2.2 Demomaster.c

```

//Demomaster.c programs the master PIC in the multiple electrode pair system
#include <pic.h>

//Make sure to change pcc.bat to reflect the correct PIC or you will
5 //have problems up here!

//Program as regular 8 bit hex or Intel

__CONFIG(0x3F72); //No code prot., no debugger, FLASH prog. memory write
                  //enabled
10               //no LVP, yes Brown Out Reset, no Watchdog, yes Power up
                  //timer
                  //High Speed Oscillator

unsigned char MMSB;
unsigned char NNSB;
15 unsigned char LLSB;
unsigned char JJSB;
unsigned char MSB;
unsigned char NSB;
unsigned char LSB;
20 unsigned char SIGN;
unsigned char trash;
unsigned char handshake;
int newlinecount;
int i;
25

void ReadADC(void);
void WriteUART(unsigned char);
void WriteHex(unsigned char);
void getdatabytes(void);
30 void transmit(void);
void delay(void);
void temp(void);

```

```

void scan(void);

35 void Linit(void) { //Linit just initializes everything and chooses
                     //all of the appropriate options in the mess of
                     //Special Registers.

    TRISA = 0x00; //Use Port A to control analog MUX.
    //RA4 -> inhibit
    //RA<0:3> -> <A:D>
    //0x01: Channel1, 0x02: Channel2, 0x04: Channel3
    //0x08: Channel4. I want to use a single
    //Port A pin for each Mux switch so I can also
    //use it to control the individual channel relays.
    //So these are MUX switches 1,2,4,8.

    TRISB = 0x00; //Use Port B to control and pole ADC,
                   //Enable Slave PICS
    //RB0: Slave1, RB1: Slave2, RB2: Slave3
    //RB4: Slave4, RB5: Slave5. RB3,6,7 are PGM
    //pins so I don't want to bend them up.

    //Configure SPI
    TRISC = 0xD0; //Configure port C: Rx and Tx set (UART);
                   //SDO Output; SDI configured by control reg
                   //as input;
                   //SCK output (Master); RC<2:0> don't care.

60     SSPCON = 0x20; //Configure Synchronous Serial Port Control Register:
                   //SSPCON<7:6> don't care;
                   //Enable Serial Port mode for SCK, SDO, SDI (and SS);
                   //Idle State for clock is Low;
                   //SPI Master Mode, clock = Fosc/4.

65     SSPSTAT = 0x40; //Configure Synchronous Serial Port Status Register:
                   //SMP Sample at middle of data output time
                   //Data transmit on rising edge of SCK.
                   //SSPSTAT<5:0> don't care.

70     //Configure UART
    RCSTA = 0x90; //Set bit SPEN to configure RX and TX as UART pins.
                   //RCSTA for Async continuous receive enable

75     TXSTA = 0x24; //Configure Transmit register:
                   //Bit 7 don't care (Async); 8-bit transmission;
                   //Transmit enabled; Asynchronous Mode; bit 3 unimp.

```

```

                                //High Baud Rate; TXSTA<1:0> don't care.

80    SPBRG =5;                      //Baud Rate Generator Value = 5 for 115.2 kbps
                                //with (11.0592MHz Clock).

                                trash = RCREG;           //Clear Serial Recv interrupt flag
PORTA = 0x00;
85    PORTB = 0x00;                  //clear slave enable pins
PORTA = 0x0F;                   //Open Relay and MUX for all Channels
}

void main(void) {
90

    Linit();                     //Initialize PIC and ADC

95    while(1){

        while (RCIF == 0)          //Wait for MATLAB to say Go!
            continue;
        handshake = RCREG;         //Clear RCIF
100   if (handshake == 'A') { //Enable Slave1 for demo
            RB0 = 1;
            PORTA = 0x01;
        }
        if (handshake == 'D') { //Enable Slave2 for demo
            RB1 = 1;
            PORTA = 0x02;
        }
        if (handshake == 'E') { //Enable Slave3 for demo
            RB2 = 1;
            PORTA = 0x04;
        }
        if (handshake == 'F') { //Enable Slave4 for demo
            RB4 = 1;
            PORTA = 0x08;
        }
110   if (handshake == 'B')
        PORTB = 0x00; //Stop Slaves
        if (handshake == 'C') { //Scan through channels
            scan();
            Linit();
        }
        else continue;
120
}

```

```

    }

}

125 //////////////////////////////////////////////////////////////////
//subroutines
////////////////////////////////////////////////////////////////

void scan(void) {

130

    while (RCIF == 0)           //Wait for MATLAB to say go
        continue;

    trash = RCREG;
    PORTA = 0x01;              //Open Relay and MUX for Channell
135    RB0 = 1;                  //Enable Slave1
    while (RCIF == 0)           //Wait for MATLAB to say it got the data
        continue;
    trash = RCREG;
    RB0 = 0;                   //Disable Slave1
140    PORTA = 0x10;             //Inhibit MUX and close relay

    while (RCIF == 0)
        continue;
    trash = RCREG;              //Clear RCIF
145    PORTA = 0x02;             //Open Relay and MUX for Channell
    RB1 = 1;                  //Enable Slave1
    while (RCIF == 0)           //Wait for MATLAB to say it got the data
        continue;
    trash = RCREG;
    RB1 = 0;                   //Disable Slave1
150    PORTA = 0x10;             //Inhibit MUX and close relay

    while (RCIF == 0)
        continue;
    trash = RCREG;              //Clear RCIF
155    PORTA = 0x04;             //Open Relay and MUX for Channell
    RB2 = 1;                  //Enable Slave1
    while (RCIF == 0)           //Wait for MATLAB to say it got the data
        continue;
    trash = RCREG;
    RB2 = 0;                   //Disable Slave1
160    PORTA = 0x10;             //Inhibit MUX and close relay

165    while (RCIF == 0)
        continue;
    trash = RCREG;              //Clear RCIF
}

```

```

    PORTA = 0x08;           //Open Relay and MUX for Channel1
    RB4 = 1;                //Enable Slave1
170   while (RCIF == 0)      //Wait for MATLAB to say it got the data
        continue;
        trash = RCREG;
        RB4 = 0;              //Disable Slave1
        PORTA = 0x10;          //Inhibit MUX and close relay
175 }

//////////////

180 void transmit(void) {           //Transmit MSB, then NSB, then LSB
                                    //Play with delimiting characters here

    MSB = 0x08;
    WriteHex(MSB);
185   WriteUART('\n');

}

//////////////

190 void ReadADC(void) {
    int SampRateByte = 0x78; //This is the value we will write to SSPBUF to initiate
                            //transmission and also to send to the SDI pin on
                            //the ADC
                            //in order to program the sampling rate as follows
                            :
195   //0x08 = 3.52kHz, 0x10 = 1.76kHz, 0x00 = 880Hz, 0
      x18 = 880Hz
      //0x20 = 440Hz, 0x28 = 220Hz, 0x30 = 110Hz, 0x38 =
      55Hz
      //0x40 = 27.5Hz, 0x48 = 13.75Hz, 0x78 = 6.875Hz

    SSPBUF = SampRateByte; //Write to SSPBUF to initiate transmission.
200   //The Value written to SSPBUF outputs to the ADC's
       SDI pin
       //and programs the sample rate.
       //SCK is output to ADC

    while (STAT_BF == 0)      //Wait till Buffer is full
        continue;
    MMSB = SSPBUF;            //8 of 32 in MSB
    SSPBUF = SampRateByte;    //next byte

```

```

    while (STAT.BF == 0)
        continue;
210   NNSB = SSPBUF;           //9-16 in NSB
    SSPBUF = SampRateByte;     //next byte
    while (STAT.BF == 0)
        continue;
    LLSB = SSPBUF;           //17-24 in LSB
215   SSPBUF = SampRateByte;   //Let the ADC finish so it can
    while (STAT.BF == 0)      //start the next cycle.
        continue;
    JJSB = SSPBUF;
                                //I leave it as an exercise to the reader to
                                //figure out why
220   SSPBUF = SampRateByte;   //I needed this extra one in order to
    while (STAT.BF == 0)      //get it working.
        continue;
}
                                //back to main with MMSB, NNSB and LLSB

225 /////////////////
const char hexlookup[] = "0123456789ABCDEF"; //Array for bin to hex conversion

void WriteHex(unsigned char x)           //Convert from bin to hex and write
230 {                                     //to the UART
    WriteUART(hexlookup[x >> 4]);
    WriteUART(hexlookup[x & 0x0f]);
}

235 ///////////////
void WriteUART(unsigned char transmitchar) { //Just write to the UART.
    while (!TXIF)                         //Wait until last transmit is done
        continue;
240   TXREG = transmitchar;                //Write to TXREG which initiates
}                                         //transmission

245 void getdatabytes(void) {             //Get 24 data bits amongst the 32 transmitted bits
:
    MSB = (((MMSB << 3) & 0b1111000) + ((NNSB >> 5) & 0b00000111));
    NSB = (((NNSB << 3) & 0b1111000) + ((LLSB >> 5) & 0b00000111));
    LSB = (((LLSB << 3) & 0b1111000) + ((JJSB >> 5) & 0b00000111));
    SIGN = ((MMSB >> 5) & 0b00000001);
}

```

```
//////////
```

B.2.3 Demoslave.c

```
//Demoslave.c programs each of the slave PICS in the multiple electrode pair system.  
#include <pic.h>  
  
4 //Make sure to change pcc.bat to reflect the correct PIC or you will  
//have problems up here!  
  
//Program as regular 8 bit hex or Intel  
  
9 __CONFIG(0x3F72); //No code prot., no debugger, FLASH prog. memory write  
enabled  
//no LVP, yes Brown Out Reset, no Watchdog, yes Power up  
timer  
//High Speed Oscillator  
  
14 unsigned char MMSB;  
unsigned char NNSB;  
unsigned char LLSB;  
unsigned char JJSB;  
unsigned char MSB;  
unsigned char NSB;  
19 unsigned char LSB;  
unsigned char SIGN;  
int newlinecount;  
  
void ReadADC(void);  
24 void WriteUART(unsigned char);  
void WriteHex(unsigned char);  
void getdatabytes(void);  
void transmit(void);  
void ftransmit(void);  
  
29 void Linit(void) { //Linit just initializes everything and chooses  
//all of the appropriate options in the mess of  
//Special Registers.  
  
34 TRISB = 0x8F; //Use Port B to control and pole ADC,  
//ADC Busy -> RBI  
//Slave Enable -> RB0  
  
//Configure SPI
```

```

39    TRISC = 0xD0; //Configure port C: Rx and Tx set (UART);
        //SDO Output; SDI configured by control reg
        //as input;
        //SCK output (Master); RC<2:0> don't care.

44    SSPCON = 0x20; //Configure Synchronous Serial Port Control Register:
        //SSPCON<7:6> don't care;
        //Enable Serial Port mode for SCK, SDO, SDI (and SS);
        //Idle State for clock is Low;
        //SPI Master Mode, clock = Fosc/4.

49    SSPSTAT = 0x40; //Configure Synchronous Serial Port Status Register:
        //SMP Sample at middle of data output time
        //Data transmit on rising edge of SCK.
        //SSPSTAT<5:0> don't care.

54
        //Configure UART
RCSTA = 0x80; //Set bit SPEN to configure RX and TX as UART pins.
        //RCSTA<6:0> don't care.

59    TXSTA = 0x24; //Configure Transmit register:
        //Bit 7 don't care (Async); 8-bit transmission;
        //Transmit enabled; Asynchronous Mode; bit 3 unimp.
        //High Baud Rate; TXSTA<1:0> don't care.

64    SPBRG =5;           //Baud Rate Generator Value = 5 for 115.2kbps
        //with (11.0592MHz Clock).

}

69 void main(void) {
    Linit();           //Initialize PIC and ADC
    while(RB0 == 1){

74        while (RB1 == 1)      //Wait for ADC to finish converting
        continue;

        ReadADC();           //Get the conversion result
        getdatabytes();      //Isolate 24 data bits out of 32
        ftransmit();          //Send the result to serial port

79    }
}

```

```

84 /////////////////
//subroutines
///////////////

89

void transmit(void) { //Transmit MSB, then NSB, then LSB

94 //Play with delimiting characters here
    WriteUART(MSB);
    WriteUART(NSB);
    WriteUART(LSB);
    WriteUART(SIGN);
99    WriteUART(0); //Delimit with a zero.

        //WriteHex(MSB);
        //WriteHex(NSB);
        //WriteHex(LSB); //Delimit with a zero.

104 //WriteHex(MSB);
    //WriteHex(NSB);
    //WriteHex(LSB);
}
109

void ftransmit(void) { //Transmit MSB, then NSB, then LSB
    //Play with delimiting characters here
    WriteHex(MSB);
    WriteUART('\n');
    WriteHex(NSB);
    WriteUART('\n');
    WriteHex(LSB);
    WriteUART('\n');
    WriteHex(SIGN);
114    WriteUART('\n'); //Delimit with a zero.

        //WriteHex(MSB);
        //WriteHex(NSB);
        //WriteHex(LSB);

119 }

124 }

/////////////

void ReadADC(void) {

```

```

129     int SampRateByte = 0x78; //This is the value we will write to SSPBUF to initiate
                                //transmission and also to send to the SDI pin on
                                //the ADC
                                //in order to program the sampling rate as follows
                                :
                                //0x08 = 3.52kHz, 0x10 = 1.76kHz, 0x00 = 880Hz, 0
                                x18 = 880Hz
                                //0x20 = 440Hz, 0x28 = 220Hz, 0x30 = 110Hz, 0x38 =
                                55Hz
                                //0x40 = 27.5Hz, 0x48 = 13.75Hz, 0x78 = 6.875Hz

134
SSPBUF = SampRateByte; //Write to SSPBUF to initiate transmission.
                        //The Value written to SSPBUF outputs to the ADC's
                        //SDI pin
                        //and programs the sample rate.
                        //SCK is output to ADC

139
while (STAT_BF == 0) //Wait till Buffer is full
    continue;

144 MMSB = SSPBUF; //8 of 32 in MSB

SSPBUF = SampRateByte; //next byte
while (STAT_BF == 0)
    continue;
NNSB = SSPBUF; //9-16 in NSB

SSPBUF = SampRateByte; //next byte
while (STAT_BF == 0)
    continue;
LLSB = SSPBUF; //17-24 in LSB

SSPBUF = SampRateByte; //Let the ADC finish so it can
while (STAT_BF == 0) //start the next cycle.
    continue;
JJSB = SSPBUF;

154
                                //I leave it as an exercise to the reader to
                                //figure out why
SSPBUF = SampRateByte; //I needed this extra one in order to
while (STAT_BF == 0) //get it working.
    continue;

```

```

169      }
170      //////////////////////////////////////////////////////////////////
171
172      const char hexlookup[] = "0123456789ABCDEF"; //Array for bin to hex conversion
173
174      void WriteHex(unsigned char x) //Convert from bin to hex and write
175      {
176          WriteUART(hexlookup[x >> 4]);
177          WriteUART(hexlookup[x & 0x0f]);
178      }
179      //////////////////////////////////////////////////////////////////
180
181      void WriteUART(unsigned char transmitchar) { //Just write to the UART.
182          while (!TXIF) //Wait until last transmit is done
183          {
184              continue;
185              TXREG = transmitchar; //Write to TXREG which initiates
186          } //transmission
187          //////////////////////////////////////////////////////////////////
188
189      void getdatabytes(void) { //Get 24 data bits amongst the 32 transmitted bits
190          :
191
192          MSB = (((MMSB << 3) & 0b1111000) + ((NNSB >> 5) & 0b00000111));
193          NSB = (((NNSB << 3) & 0b1111000) + ((LLSB >> 5) & 0b00000111));
194          LSB = (((LLSB << 3) & 0b1111000) + ((JJSB >> 5) & 0b00000111));
195          SIGN = ((MMSB >> 5) & 0b00000001);
196      }

```

Appendix C

Schematics and PCBs

C.1 PCB: Front-End Only

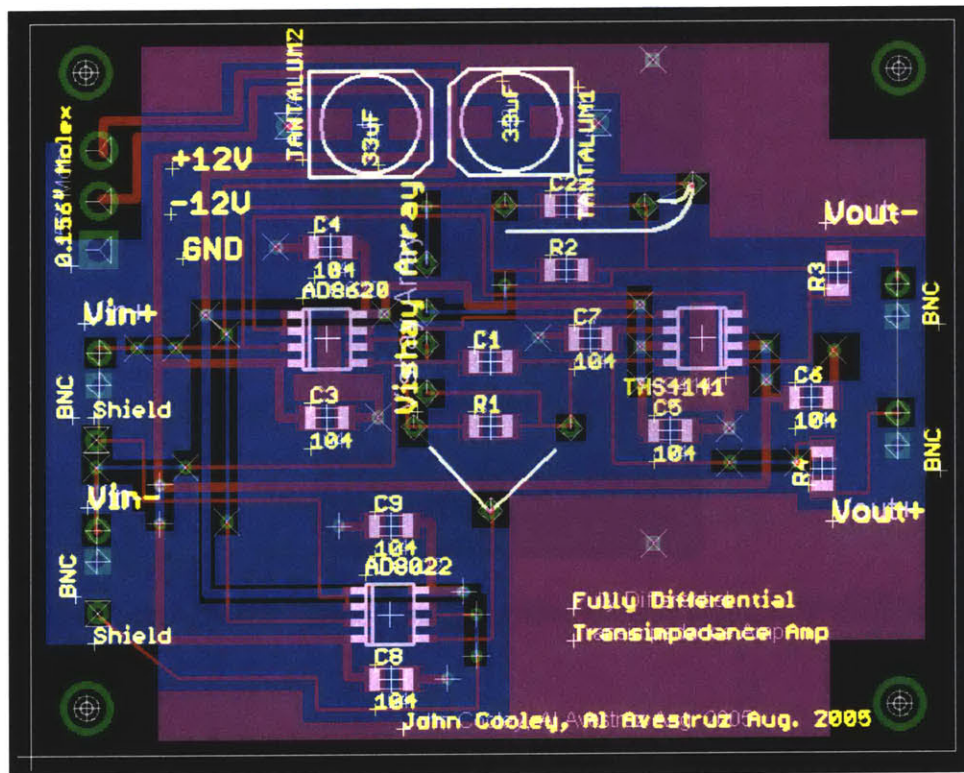


Figure C-1: A PCB for the front-end amplifier

C.2 PCB: Full Channel

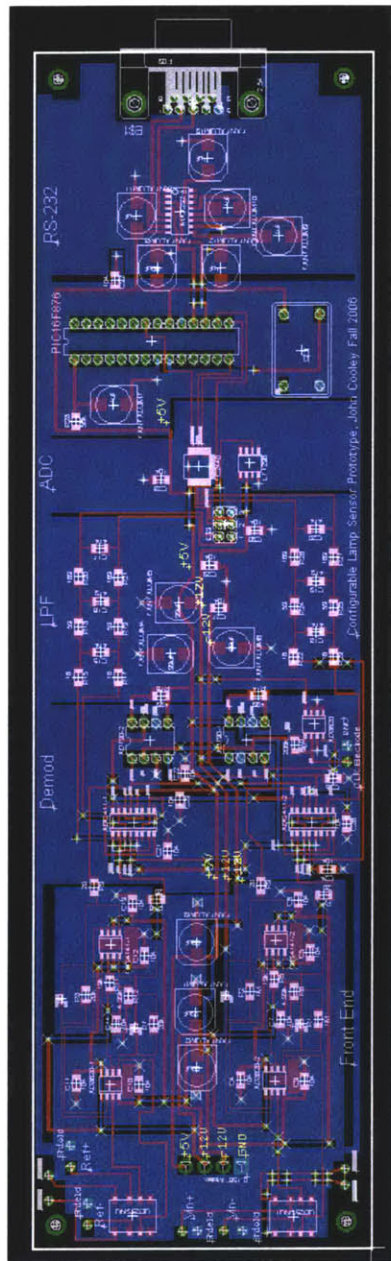


Figure C-2: The single channel prototype lamp sensor mixed-signal PCB.

Bibliography

- [1] Al-Thaddeus Avestruz, John I. Rodriguez, Roderick Hinman, Gary Livshin, Elmer C. Lupton. “Stability Considerations and Performance of Wide Dynamic Range, Ambient Light Active Rejection Circuits in Photodiode Receivers”. *Proceedings of the 2004 American Control Conference*
- [2] Kara E. Bliley, David R. Holmes III; paul H. Kane, Randal C. Foster, James A. Levine, Erik S. Daniel, Barry K. Gilbert “A Miniaturized Low Power Personal Motion Analysis Logger Utilizing MEMS Accelerometers and Low Power Microcontroller”. *Microtechnology in Medicine and Biology, 2005. 3rd IEEE/EMBS Special Topic Conference on*
- [3] Yi-Tsung Chien, Yea-Shuan Huang, Sheng-Wen Jeng, Yao-Hong Tasi, Hung-Xin Zhao “A Real-time Security Surveillance System for Personal Authentication”. *Security Technology, 2003. Proceedings. IEEE 37th Annual 2003 International Carnahan Conference on.*
- [4] C. L. Chua, R.L. Thornton, D.W. Treat, V.K. Yang, and C. C. Dunnrowicz. “Indium Tin Oxide Transparent Electrodes for Broad-Area Top-Emitting Vertical-Cavity Lasers”. *IEEE Photonics Technology Letters, Vol. 9, No. 5, 1997.*
- [5] John Cooley, Al-Thaddeus Avestruz, Steven Leeb. “Proximity Detection and Ranging Using a Modified Fluorescent Lamp for Security Applications”. *Proceedings of the 2006 International Carnahan Conference on Security Technology*
- [6] John Cooley, Al-Thaddeus Avestruz, Stven Leeb. “Digest: A Fluorescent Lamp and Ballast Modification to Sense Personnel Activity Levels for Building Energy and Power Management”. *PESC 2007 digest submissions December, 2006.*

- [7] Chong-Gun Yu, Randall L. Geiger. "Analysis of Random Common-Mode Rejection Ratio in Op-Amps" *Circuits and Systems, 1992., Proceedings of the 35th Midwest Symposium on 9-12 Aug. 1992* Page(s):949 - 952 vol.2
- [8] Christian C. Enz, Gabor C. Temes. "Circuit Techniques for Reducing the Effects of Op-Amp Imperfections: Autozeroing, Correlated Double Sampling, and Chopper Stabilization." *Proceedings of the IEEE, Vol. 84, No. 11, November 1996.*
- [9] Robert Cox, Steven Leeb, Steven R. Shaw, Leslie K. Norford "Transient Event Detection for Nonintrusive Load Monitoring and Demand Side Management Using Voltage Distortion". *Applied Power Electronics Conference and Exposition, 2006. APEC '06. Twenty-First Annual IEEE*
- [10] James T. Dakin. "Nonequilibrium Lighting Plasmas". *IEEE Transactions on Plasma Science, Vol. 19, No. 6, 1999.*
- [11] A.C.M Fong, S.C. Hui "Web-based intelligent surveillance system for detection of criminal activities". *Computing and Control Engineering Journal December 2001*
- [12] Susan B. Garavaglia. "Statistical Analysis of the Tanimoto Coefficient Self-Organizing Map (TCSOM) applied to health behavioral survey data" *Neural Networks, 2001. Proceedings. IJCNN '01. International Joint Conference on Volume 4, 15-19 July 2001* Page(s):2483 - 2488 vol.4
- [13] Steven L. Garverick, Michael L. Nagy, Naresh K. Rao, David K. Hartsfield, Arvind Purushotham "A Capacitive Sensing Integrated Circuit for Detection of Micromotor Critical Angles". *IEEE Journal of Solid-State Circuits, Vol. 32, No. 1, January 1997.*
- [14] Thomas Heseltine, Nick Pears, Jim Austin "Three-Dimensional Face Recognition: An Eigensurface Approach". *2004 International Conference on image Processing (ICIP)*
- [15] Tiffany k. Buffaloe, Deron J. Jackson, Steven B. Leeb, Martin F. Schlect, Rebecca A. Leeb. "Fiat Lux: A Fluorescent Lamp Transceiver". *Proceedings of the Applied Power Electronics Conference and Exposition, 1997 (APEC)*

- [16] Seven B. Leeb, Steven R. Shaw, James L. Kirtley Jr. “Transient Event Detection in Spectral Envelope Estimates for Nonintrusive Load Monitoring”. *IEEE Transactions on Power Delivery*, Vol. 10, No. 3, July 1995
- [17] Steven B. Leeb, James L. Kirtley Jr., David S. Woodruff, Michael S. LeVan. “Building-Level Power Network Analysis”. *Computer Applications in Power, IEEE Vol. 5, Issue 1, Jan. 1992 Pages:30-34*
- [18] Umair A. Khan, Seven B. Leeb, Mark C. Lee. “A Multiprocessor for Transient Event Detection”. *IEEE Transactions on Power Delivery, Col. 12, No. 1 January 1997*
- [19] Hao Luo, Gang Zhang, L. Richard Carley, Gary K. Fedder “A Post-CMOS Micromachined Lateral Accelerometer”. *Journal of Microelectromechanical Systems, Vol. 11, No. 3, June 2002.*
- [20] D. Marioli, E. Sardini, A. Taroni. “High Accuracy Measurement Techniques for Capacitance Transducers”. *Measurement Science and Technology, No. 4, 1993, U.K.*
- [21] K. Nabors, et al. “Multipole-accelerated capacitance extraction algorithms for 3-D structures with multiple dielectrics”. *IEEE Transactions Circuits and Systems-I: Fundamental Theory and Applications, vol. 39, pp. 946-954, Nov. 1992.*
- [22] Alan V. Oppenheim, Alan S. Willsky. *Signals and Systems Second Edition Prentice Hall, New Jersey 07458, 1997.*
- [23] James K. Roberge. *Operational Amplifiers: Theory and Practice John Wiley and Sons, Inc., New York, London, Sydney, Toronto, 1975.*
- [24] Anwar Sadat, Hongwei Qu, Chuanzhao Yu, Jiann SS. Yuan, Huikai Xie “Low-Power CMOS Wireless MEMS Motion Sensor for Physiological Activity Monitoring”. *IEEE Transactions on Circuits and Systems-I: Regular Papers, Vol. 52, No. 12, December 2005.*
- [25] J.R. Smith. “Field mice: Extracting hand geometry from electric field measurements”. *IBM Systems Journal, Vol. 35, Nos. 3 and 4, 1996*

- [26] Lewis Smith and D.H. Sheingold. “AN-358 Application Note: Noise and Operational Amplifier Circuits”. *Reprinted from Analog Dialogue 3-1, 1969, Analog Devices. Norwood, MA, USA.*
- [27] Meng-Lieh Sheu, Chih-Kuan Lai, Wei-Hung Hsu, Hong-Ming Yang “A Novel Capacitive Sensing Scheme for Fingerprint Acquisition”. *Electron Devices and Solid-State Circuits, 2005 IEEE Conference on*
- [28] David Stoppa, Lorenzo Gonzo, Andrea Simoni “Scannerless 3D Imaging Sensors”. *IEEE IST 2005*
- [29] Marco Tartagni and Roberto Guerrieri “A Fingerprint Sensor Based on the Feedback Capacitive Sensing Scheme”. *IEEE Journal of Solid-State Circuits, Vol. 33, No. 1, January 1998*
- [30] R.C. Tozer, J.C. Simpson, I.L. Freeston, J.M. Mathias “Noncontact Induced Current Impedance Imaging”. *Electronics Letters 9th April 1992 Vol. 28 No. 8.*
- [31] C.-C. Wang and R.J.-W. Chen. “Three Modified Dependency-tests for Software Failures”. *IEEE Proceedings on Reliability and Maintainability, 2002.*
- [32] J. Waymouth “Electrical Discharge Lamps” *MIT Press, Cambridge, MA, 1971.*
- [33] Raphael Wimmer, Paul Holleis, Matthias Kranz, Albrecht Schmidt “Thracker - Using Capacitive Sensing for Gesture Recognition”. *Proceedings of the 26th IEEE International Conference on Distributed Computing Systems Workshops*
- [34] Alejandro Gonzalez-Nakazawa, Jose Carlos Gamio, Wuqiang Yang. “Transient Processes and noise in a Tomography System: An Analytical Case Study”. *IEEE Sensors Journal, Vol. 5, No. 2, April 2005*
- [35] “LT1236 data sheet”. Linear Technology. Milpitas, CA, USA.
- [36] “AD8610 data sheet”. Analog Devices. Norwood, MA, USA.
- [37] “THS4140 data sheet.” Texas Instruments. Dallas, TX, USA.

- [38] “CD4067b data sheet.” Texas Instruments. Dallas, TX, USA.
- [39] “AD790 data sheet.” Analog Devices. Norwood, MA, USA.
- [40] “LT1236 data sheet.” Linear Technology. Milipitas, CA, USA.
- [41] “ADG411 data sheet.” Analog Devices. Norwood, MA, USA.
- [42] “LT2440 data sheet.” Linear Technology. Milipitas, CA, USA.
- [43] “PIC16F876 data sheet.” Microchip Technology Corp. USA
- [44] “MAX232 data sheet.” Maxim Integrated Products. Sunnyvale, CA, USA.
- [45] “CD4067b data sheet.” Texas Instruments. Dallas, TX, USA.
- [46] “ECS-100 Oscillator data sheet.” ECS Inc. Olathe, KS, USA.
- [47] “AD8132 data sheet.” Analog Devices. Norwood, MA, USA.